



Dynamic Modeling, Control and Stability Analysis of VSC-based Energy Storage Systems

Álvaro Ortega Manjavacas, B.E.

13203985

A thesis submitted to University College Dublin
in fulfillment of the requirements for the degree of

Philosophiæ Doctor

College of Engineering and Architecture
School of Electrical and Electronic Engineering

Head of School: Dr. Andrew Keane

Supervisor: Prof. Federico Milano

April 2017

I hereby certify that the submitted work is my own work, was completed while registered as a candidate for the degree stated on the Title Page, and I have not obtained a degree elsewhere on the basis of the research presented in this submitted work.

© by Álvaro Ortega Manjavacas, 2017
All Rights Reserved.

A mis amados padres y hermano. Sin vosotros no hubiese sido posible.

Acknowledgements

Over the course of the past three years of my Ph.D., I have realized two things: first, no thesis is ever really finished, and second, thanking every person who has helped me to accomplish this work in any of the ways is truly an unapproachable issue.

I should first thank my supervisor and mentor Prof. Federico Milano for the trust he put in me since our first encounter, for his invaluable advices, and his endless motivation to constantly improve as a researcher, as well as a person.

I thank my colleagues with whom I have had the opportunity to work, for the stimulating discussions, and for all the fun we have had in the last years. They provided a friendly and cooperative atmosphere at work and also useful feedback and insightful comments on my work.

Finally, with all my love, I would like to thank my beloved parents and brother for their encouragement and support throughout my entire life, without which this thesis would not have been possible. I am also grateful to my beloved Alicia for her appearance in the most difficult moment of my life, and her support, energy and motivation until the end of this thesis.

“We need books that affect us like a disaster, that grieve us deeply, like the death of someone we loved more than ourselves, like being banished into forests far from everyone, like a suicide. A book must be the axe for the frozen sea within us.”

Franz Kafka

“Being myself includes taking risks with myself, taking risks on new behavior, trying new ways of 'being myself', so that I can see who it is I want to be.”

Hugh Prather, *Notes to Myself*

Contents

List of Figures	x
List of Tables	xiv
List of Abbreviations and Acronyms	xv
Abstract	xvii
1 Introduction	1
1.1 Motivation	1
1.2 Thesis Overview and Contributions	6
1.3 Publications	9
1.3.1 Journal Papers	9
1.3.2 Conference Papers	9
1.3.3 Publications Arising	10
2 VSC-Based Energy Storage Systems: Overview and Technologies	11
2.1 Common Elements of VSC-Based ESSs	12
2.1.1 Storage Control	12
2.1.2 Voltage Sourced Converter	14
2.2 Features and Modeling of Different ESS Technologies	17
2.2.1 Battery Energy Storage	17
2.2.2 Above Ground Compressed Air Energy Storage	19
2.2.3 Flywheel Energy Storage	22
2.2.4 Super Capacitor Energy Storage	23
2.2.5 Superconducting Magnetic Energy Storage	24

3	Frequency Estimator Modeling: Introducing the Frequency Divider	26
3.1	Motivation	26
3.2	Modeling of Different Frequency Estimators	28
3.2.1	Center of Inertia	28
3.2.2	Washout Filter	28
3.2.3	Frequency Divider	30
3.3	Example: 3-Bus System	33
3.4	Comparison of Different Frequency Estimators: Frequency Controlled Loads	39
3.4.1	IEEE 14-Bus Test System	40
3.4.2	New England 39-Bus, 10-Machine Test System	44
3.4.3	Remarks	46
3.5	Case Study: Frequency Estimators in Real Systems	47
3.5.1	Irish Transmission System	47
3.5.2	ENTSO-E Transmission System	51
3.6	Concluding Remarks	53
4	Generalized Model of Energy Storage Systems	54
4.1	Motivation	54
4.2	Proposed Generalized Model of Energy Storage Devices	56
4.2.1	Generalized model of different storage technologies	59
4.3	Case Study	61
4.3.1	SMES	62
4.3.2	CAES	68
4.3.3	BES	70
4.4	Concluding Remarks	71
5	Formulation, Design and Comparison of Control Strategies for Energy Storage Systems	73
5.1	Motivation	73

5.2	Control Strategies for ESSs	74
5.2.1	PI Control	75
5.2.2	H_∞ Control	75
5.2.3	Sliding Mode Control	78
5.3	Case Study: IEEE 14-Bus Test System	80
5.3.1	Line Outage	81
5.3.2	Loss of Load	84
5.4	Case Study: Irish Transmission System	87
5.4.1	Line Active Power Flow Regulation	88
5.4.2	Primary Frequency Regulation	93
5.5	Concluding Remarks	95
6	Stochastic Transient Stability Analysis of Transmission Systems with Inclusion of Energy Storage Devices	96
6.1	Motivation	96
6.2	Effect of ESSs on the Transient Stability of Power Systems	98
6.2.1	One-Machine Infinite-Bus	98
6.2.2	One-Machine Infinite-Bus with a STATCOM device	99
6.2.3	One-Machine Infinite-Bus with an ESS	101
6.3	Probabilistic Stochastic Transient Stability Analysis	102
6.4	Case Study: Irish Transmission System	104
6.5	Concluding Remarks	106
7	Conclusion and Scope for Future Work	109
A	Storage Input Limiter	114
A.1	Deterministic Variation of Load	114
A.2	Stochastic Variation of Load	116
A.3	Concluding Remarks	118

B Stochastic Models of Wind and Loads	119
B.1 Load Stochastic Processes	119
B.2 Wind Stochastic Processes	120
C Map of the All-Island Irish Transmission System	121
Bibliography	122
Index Terms	132

List of Figures

1.1	Comparison of power rates and discharge times of different ESS technologies.	3
2.1	Scheme of the ESS connected to a grid.	11
2.2	Storage control scheme.	12
2.3	VSC scheme.	14
2.4	Block diagram of the VSC inner current control and converter.	15
2.5	PLL scheme.	15
2.6	Outer dc and ac voltage controllers of the VSC.	16
2.7	Scheme of a μ CAES.	19
2.8	Scheme of a FES.	22
2.9	Scheme of a SCES.	24
2.10	Scheme of the SMES and the boost converter.	25
3.1	Numerical derivative of the bus voltage phase angle composed of a washout and a low pass filters.	29
3.2	Two-machine radial system.	34
3.3	3-bus system.	35
3.4	3-bus system – Synchronous machine rotor speeds, COI frequency, and frequency at bus 3 estimated based on the proposed FD approach.	35
3.5	3-bus system – Frequency at bus 3 estimated with FD and the conventional WF. The system is simulated using the fully-fledged dq -axis model.	36

3.6	3-bus system – Frequency at bus 3 estimated with the FD and the conventional WF. The load is modeled as a frequency-dependent load representing an aluminum plant.	38
3.7	3-bus system – Frequency at bus 3 estimated with the FD and the conventional WF. The load is a squirrel cage induction motor with a 5 th -order <i>dq</i> -axis model.	38
3.8	Thermostatically controlled load with frequency control.	39
3.9	IEEE 14-bus test system.	40
3.10	Frequency of bus 2 when TCLs are not included.	41
3.11	Rotor speed of the synchronous generator in bus 2 when TCLs are included.	42
3.12	Frequency of bus 2 with 20% of system overload without TCLs.	42
3.13	Estimated frequency at bus 14 using WF, FD and the COI.	43
3.14	Rotor speed of the synchronous generator in bus 2 with 20% of system overload and TCLs.	43
3.15	New England 39-bus, 10-machine system.	44
3.16	Rotor speed of the synchronous generator in bus 31 (Gen 2).	45
3.17	Frequency response of the Irish transmission system facing a three-phase fault close to a synchronous machine.	49
3.18	Scheme of a section of the Irish transmission system that includes a wind power plant.	50
3.19	Frequency response of the Irish transmission system facing a three-phase fault close to a wind power plant.	51
4.1	Scheme of a simplified ESS model.	54
4.2	WSCC 9-bus test system with an ESS device connected to bus 8.	61
4.3	Response of the WSCC system with a SMES following a three-phase fault at bus 7.	63

4.4	Response of the WSCC system following a three-phase fault at bus 7 when the SMES reaches its maximum storable energy.	64
4.5	Response of the WSCC system with a SMES considering stochastic variations of the loads.	67
4.6	Response of the WSCC system with a CAES following a loss of load. . . .	68
4.7	Response of the WSCC system with a CAES considering stochastic perturbations in the loads.	69
4.8	Response of the WSCC system with a BES following a loss of load.	71
5.1	PI-based control for ESSs.	75
5.2	H_{∞} controller.	76
5.3	Graphical representation of the dynamic behavior of a sliding control. . .	78
5.4	Response of the 14-bus system with an ESS following the opening of line 2-4 for a low wind profile.	82
5.5	Response of the 14-bus system with an ESS following the opening of line 2-4 for a high wind profile.	83
5.6	Response of the 14-bus system with an ESS following the loss of the load at bus 9 for a high wind profile.	85
5.7	Response of the 14-bus system with an ESS following the loss of the load at bus 9 for a high wind profile and considering energy limits of the storage device.	86
5.8	Irish system with HESS and a three-phase fault followed by a line trip. . .	89
5.9	Irish system without HESS and a three-phase fault followed by a line trip: Active power flowing through the regulated line.	90
5.10	Irish system with HESS and a three-phase fault followed by a line disconnection: Active power flowing through regulated line.	91
6.1	Classification of the categories of power system stability.	96

6.2	Scheme of a generator connected to an infinite bus through a transformer and a transmission line.	98
6.3	EAC of an OMIB system.	99
6.4	Scheme of a generator connected to an infinite bus with the inclusion of a STATCOM device.	100
6.5	EAC of an OMIB system with a STATCOM.	100
6.6	Scheme of a generator connected to an infinite bus with the inclusion of an ESS.	101
6.7	EAC of an OMIB system with an ESS.	101
6.8	Topologies of a power system facing a fault.	105
6.9	Response of the Irish transmission system during a three-phase fault (Topology 1).	107
6.10	Rotor angle of the synchronous machine during a three-phase fault (Topology 2) with a FES regulating ω_{bus} and ω_{COI}	107
6.11	Rotor angle of the synchronous machine during a three-phase fault for the two topologies with a BES regulating ω_{bus}	108
A.1	Storage control scheme.	114
A.2	Response of the WSCC system with a BES to deterministic variations of the load.	115
A.3	Response of the WSCC system with a BES when stochastic perturbations are considered for the loads.	117
C.1	Schematic map of the all-island Irish transmission system	121

List of Tables

1.1	Technical Features of ESS Technologies.	3
1.2	Typical Costs of ESS Technologies.	4
3.1	Computational burden of different bus frequency estimators.	51
3.2	Size and number of non-zeros (NNZ) elements of matrices \mathbf{B}_{BB} , \mathbf{B}_{G0} , \mathbf{B}_{BG} and \mathbf{D} for the ENTSO-E system.	52
4.1	Examples of energy storage technologies.	55
4.2	GEM variables and parameters of BES technology.	59
4.3	GEM variables and parameters of CAES technology.	60
4.4	GEM variables and parameters of FES technology.	60
4.5	GEM variables and parameters of SMES technology.	60
5.1	Comparison of σ_P for different loading levels during a fault in the Irish system.	92
5.2	Comparison of n_{sat} of the HESS for different loading levels during a fault in the Irish system.	92
5.3	Comparison of σ_ω and $\Delta\mu_\omega$ for different HESS controllers during a synchronous machine outage in the Irish system.	94
6.1	Percentage of unstable simulations after a three-phase fault for Topology 1 in the Irish system for different CTs.	105
6.2	Percentage of unstable simulations after a three-phase fault for Topology 2 in the Irish system for different CTs.	106

List of Abbreviations and Acronyms

AGC	Automatic Generation Control
AVR	Automatic Voltage Regulator
BES	Battery Energy Storage
CAES	Compressed Air Energy Storage
CCT	Critical Clearing Time
COI	Center of Inertia
DAE	Differential Algebraic Equation
EAC	Equal Area Criterion
EMF	Electromotive Force
ESS	Energy Storage System
FACTS	Flexible AC Transmission Systems
FCES	Fuel Cell Energy Storage
FD	Frequency Divider
FES	Flywheel Energy Storage
FLC	Fuzzy Logic Control
GEM	Generalized Energy Storage System Model
HESS	Hybrid Energy Storage System
IGBT	Integrated Gate Bipolar Transistor
MPC	Model Predictive Control
OMIB	One-Machine Infinite-Bus

PDF	Probability Density Function
PHES	Pumped Hydro Energy Storage
PLL	Phase-Locked Loop
PSS	Power System Stabilizer
RES	Renewable Energy Source
RoCoF	Rate of Change of Frequency
SCES	Super Capacitor Energy Storage
SDAE	Stochastic Differential Algebraic Equation
SIL	Storage Input Limiter
SM	Sliding Mode
SMES	Superconducting Magnetic Energy Storage
SOC	State of Charge
STATCOM	Static Synchronous Compensator
STSA	Stochastic Transient Stability Analysis
TCL	Thermostatically Controlled Load
TG	Turbine Governor
TSA	Transient Stability Analysis
VSC	Voltage Sourced Converter
WF	Washout Filter

Abstract

The capability of power converter-based Energy Storage Systems (ESSs) to improve the transient behavior of power systems and to increase the competitiveness of non-dispatchable power production technologies such as renewable energies, has led, in recent years, to a huge investment in research, prototyping and installation of storage devices. Among the technologies that currently appear most promising, there are battery energy storage, compressed air energy storage, flywheel energy storage, super capacitor energy storage and superconducting magnetic energy storage.

One of the main purposes of ESSs is the regulation of a given system frequency. Therefore, a reliable technique to estimate that frequency is needed in power system simulators. With this aim, three approaches to estimate the frequency at different points of the network are defined and compared, namely the well-known center of inertia, the commonly used washout filter, and a new frequency estimation approach proposed in this thesis. The latter is based on the voltage-divider formula, and computes the frequencies at every bus of the network. The performance, accuracy and computational efficiency of the three estimation techniques are duly studied and compared based on comprehensive case studies using two real-world systems.

Modeling ESSs is a complex and time-consuming task due to the several different technologies that are currently available and that are expected to be developed in the future. While there are comprehensive studies aimed at defining the economic viability and the effect on electricity markets of ESSs, there is still no commonly-accepted simple yet detailed general model of ESSs for voltage and angle stability studies. The aim of this thesis is to develop a generalized model of ESSs to simplify, without giving up accuracy, the simulation of different storage technologies. The objective is to provide a balanced, fundamental frequency model that can be defined through a reduced and fixed set of parameters and equations, and that can be readily implemented in power system simulators for voltage and angle stability analysis.

The proposed model is based on the observation that most ESSs connected to transmission and distribution grids share a common structure, i.e., are coupled to the ac network through a voltage sourced converter, present a dc-link and then include another converter (either a dc/dc or an ac/dc device) to connect the main energy storage device to the dc link. Moreover, all storage systems necessarily imply potential and flow quantities, whose dynamics characterize the transient response of the ESS. To properly capture the dynamic response of the ESS, it is important to preserve such dynamics along with those of the ESS regulators. Controller hard limits are also relevant.

Following the definition of a generalized model, the next objective is to design and compare different control strategies of ESS devices. The control scheme that has been most widely installed in ESSs is the PI, due mainly to its easy implementation for both linear and nonlinear systems. However, the performance of PI controllers can be affected by changes in system topology. The linear structure of the equations of the generalized ESS model proposed in this thesis facilitates the design and implementation of potentially more robust control strategies that are being studied and developed in the literature, such as Sliding Mode and H-infinity controllers. With this aim, different control strategies for ESSs are compared in terms of robustness, design and practical implementation.

Finally, this thesis focuses on transient stability analysis of power systems with the inclusion of ESSs. Fast response of ESSs, and their capability to provide both active and reactive power supports are expected, as byproduct, to improve the transient stability of the grid. With that aim, the thesis presents a detailed stochastic and statistical analysis of the impact of ESSs on the transient stability of transmission grids. The study compares the critical clearing times of a power system with a variety of ESS technologies and network topologies. The latter concerns the relative positions of faults, storage devices and synchronous machines. The case study provided in the thesis consists of stochastic time-domain simulations carried out for a real-world system model. Simulations also include FACTS devices, and results are compared with those of ESSs.

1 | Introduction

1.1 Motivation

In recent years, development and installation of Renewable Energy Sources (RESs) (e.g. wind turbines, solar power plants, etc.) have undergone a steady growth in their path to gradually substitute conventional power plants in the production of electricity [33, 116, 117]. This replacement is leading to a transition from a highly centralized electricity production to a decentralized one that is based on variable sources of stochastic nature. Given the fact that electricity must be produced and consumed at the same instant, most renewable energies are characterized by a limited reliability, as they do not guarantee the supply-demand balance. Moreover, the increase of the penetration of RESs leads to a reduction of the total inertia of the system. Therefore, novel schemes to regulate both the system frequency and the rate of change of frequency (RoCoF) become essential.

Among all currently existing alternatives to improve the performance, reliability and resiliency of power systems with high RESs penetration, Energy Storage Systems (ESSs) appear to be one of the most promising [55, 15, 100]. ESSs have the potential to provide a large variety of ancillary services to the system thanks to their capability to supply/absorb active and reactive powers. These services include flattening of the power provided by RESs, active power regulation in transmission lines, local and/or global frequency regulation, RoCoF mitigation, and local voltage regulation. These features of ESSs have led, in recent years, to a huge investment in the research, development, prototyping and installation of a large variety of technologies. Among all ESS technologies that currently appear most promising there are Battery Energy Storage (BES), Compressed Air Energy Storage (CAES), Fuel Cell Energy Storage (FCES), Flywheel Energy Storage (FES), Pumped Hydro Energy Storage (PHES), Super Capacitor Energy Storage (SCES) and Superconducting Magnetic Energy Storage (SMES).

According to the features, sizes and time-scales of each of these technologies, two main groups can be defined: *seasonal energy storage* (PHES, large-scale CAES) and “*transient*”, *power converter-based energy storage* (e.g., BES, FES).

Seasonal storage has been used for decades for both technical and economical purposes [43, 39, 24, 98]. These systems are usually designed with the aim of storing energy during the power demand valleys, when the electricity cost is lower (night time), and to release it to the grid during the demand peaks when the electricity is more expensive. Seasonal storage is characterized by a relatively large energy capacity, and a relatively low cost per MWh. However, the installation of PHESs and large-scale CAESs is geographically limited to the existence of water reservoirs and underground caves, respectively. Moreover, the time response of these systems, despite being usually faster than conventional synchronous power plants, is slow when compared with other power system dynamics.

On the other hand, time responses of transient ESSs, which usually are in the range of tens of milliseconds to few seconds, are much faster when compared with seasonal ones, which usually span few minutes. These systems are generally connected to the grid through a Voltage Sourced Converter (VSC), and therefore are decoupled from the grid frequency [100, 5, 69, 45]. The high speed of response to produce/absorb both active and reactive power makes VSC-based ESSs suitable for maintaining and improving the reliability and power quality of the system. VSC-based ESSs are able to rapidly regulate the voltage at the bus of connection with the grid, damp system oscillations due to contingencies, etc. The main issue with current transient VSC-based ESSs which greatly limits their installation is their high ratio cost vs. capacity. However, this ratio has improved greatly in recent years, increasing the economical viability of these devices. Moreover, the trend of increasing the size while reducing the cost of ESSs is expected to continue progressively in the following years.

Figure 1.1 presents a general comparison of the power ratings and the discharge time at rated power of a variety of ESS technologies, while relevant information and characteristics of different ESSs are provided in Table 1.1 [2, 94]. In Fig. 1.1, the region of interest of the studies provided in the thesis corresponds to the Transmission and Distribution (T&D) Grid Support.

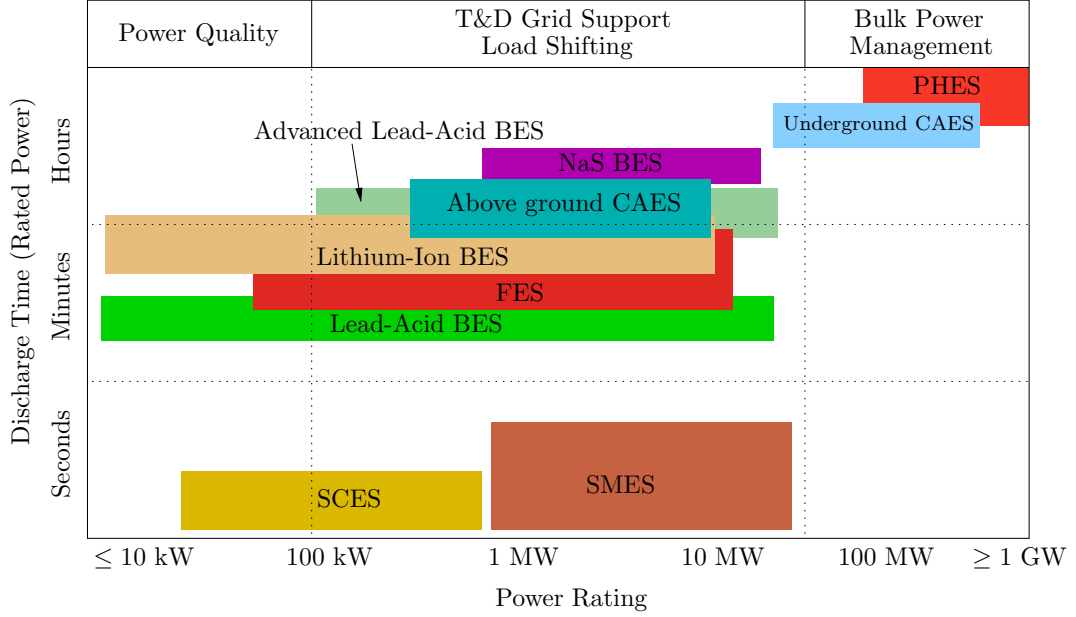


Figure 1.1: Comparison of power rates and discharge times of different ESS technologies [2, 94].

Table 1.1: Technical Features of ESS Technologies [2, 94].

Technology	Capacity (MWh)	Response Time	Maturity	Life Time (years)	Efficiency (%)
Electrochemical					
Lead-acid BES	0.25~50	≤1 sec	Demo~Commercial	≤20	≤85
Lithium-ion BES	0.25~25	≤1 sec	Demo	≤15	≤90
NaS BES	≤300	≤1 sec	Commercial	≤15	≤80
Mechanical					
CAES (underground)	≤2,700	≤15 min	Mature	≤40	≤60
CAES (above ground)	≤20	sec~min	Demo	≤40	≤85
FES	≤10	≤10 ms	Demo~Mature	≤20	≤85
PHES	≤14,000	≤10 min	Mature	≤70	≤85
Electrical					
SCES	0.1~0.5	≤10 ms	Commercial	≤40	≤95
SMES	1~3	≤10 ms	Demo~Mature	≤40	≤95

Design, installation and operation of ESSs must be carefully studied considering several aspects:

- *Cost:* A very important factor in the installation of ESSs in power systems is the total cost of the unit. This should include the capital cost of installation, and the operating cost which covers the operation, maintenance, disposal and replacement costs [9]. In the literature, ESSs costs are usually expressed in terms of power (\$ per kW) and energy (\$ per kWh) capacities, while for ESSs technologies characterized by a large number of charge/discharge processes, the unit is \$ per kWh-per cycle. Table 1.2 provides typical costs for some of the most common ESS technologies.

Table 1.2: Typical Costs of ESS Technologies [9].

Technology	\$/kW	\$/kWh	\$/kWh-per cycle
Electrochemical			
Lithium-ion BES	1,200-4,000	600-2,500	15-100
NaS BES	1,000-3,000	300-500	8-20
Mechanical			
CAES (underground)	400-800	2-50	2-4
FES	250-350	1,000-5,000	3-25
PHES	600-2,000	5-100	0.1-1.4
Electrical			
SCES	100-300	300-2,000	2-20
SMES	200-300	1,000-10,000	

- *Dynamic behavior:* The study of the interaction of ESSs with the transmission/distribution grid is imperative in order to obtain the optimal performance of these devices. With this aim, the behavior of ESSs must be studied for a large variety of scenarios prior to their actual installation, in order to prevent any undesirable and unexpected response caused by the nonlinearities and couplings of the devices and controllers that compose the ESS.

- *Efficiency*: ESSs, as any other kind of energy system, are non ideal and thus, losses are always present in the operation of these devices [95]. Energy conversions, power converter switches, internal resistances and mechanical frictions are examples of stages where power and energy losses exist in ESS. Moreover, the number of operations of ESSs is expected to be high during their working life. Therefore, the minimization of the losses, and thus the enhancement of the efficiency of ESSs, are critical steps in the study of these systems.
- *Flexibility of design and applications*: The flexibility that characterizes ESSs can be studied in different stages. On one hand, the modular design of most VSC-based ESSs offers the possibility to increase/decrease the power and/or energy capacities of the storage device that was initially design and installed, according to changes in the system and regulation requirements. Secondly, the location of VSC-based ESSs is not limited by geographical features, and thus, they can be optimally placed and installed in the system. Moreover, once installed, these devices can be moved and relocated if required. Finally, ESSs give the possibility to alternate their applications, according to their initial installation purpose. These include *bulk energy applications* (e.g., energy arbitrage and peak shaving), *ancillary services* (e.g., load following, frequency and voltage regulation), *customer energy management* (e.g., power quality and reliability), and *renewable energy integration* [2, 94, 47].

The handicap of the current high costs of ESSs has inspired a large number of works that try to optimize every economical aspect of these devices, such as sizing [75, 23], location [10, 29], and degradation [111]. These studies, which usually consider time scales that span from several hours to months, generally do not take into account the physical, dynamic interactions of all the elements that compose the ESS, i.e., the storage and VSC devices, and their controllers. This simplification, which neglects the nonlinear nature of the ESS components, can lead to unexpected responses of the real ESS. This study aims to fill this gap, and focuses on the dynamic performance of VSC-based ESSs for transient stability time frames (seconds-minutes), showing the importance of taking into account their intrinsic nonlinearities.

1.2 Thesis Overview and Contributions

This thesis presents a comprehensive study of the dynamic interaction of VSC-based ESSs with transmission grids. To this aim, the following tasks are addressed:

- i. *Frequency estimation:* Firstly, different approaches to estimate the frequency to be regulated by the ESS are described and compared, including a new estimation technique proposed in this thesis. The comparison is based on the results of dynamic simulations of the Irish and the ENTSO-E transmission systems.
- ii. *ESS modeling:* Transient stability models of different ESS technologies are presented. The thesis proposes a generalized ESS model, composed of a reduced and fixed set of linear equations, and able to accurately reproduce the behavior of all transient stability ESS models that are studied.
- iii. *ESS control:* The generalized ESS model is then used to design and implement different control strategies for the storage device. The thesis provides an exhaustive study that includes and combines different storage technologies (e.g., BES, FES) with a variety of control techniques (e.g., PI, H-infinity) and regulation strategies (e.g., frequency, voltage, active power flow) in large, real-world networks such as the Irish transmission grid.
- iv. *ESS transient stability analysis:* Finally, a comprehensive, stochastic transient stability analysis of ESSs coupled with a real-world transmission grid is presented. The analysis studies the effect of the inclusion of ESSs on the fault critical clearing times, and is based on the probabilistic results of thousands of time-domain simulations of the Irish transmission system with ESSs.

The remainder of the thesis is organized as follows.

Chapter 2 presents the general configuration of a VSC-based ESS. The different devices and controllers that compose the ESS and that are common to all storage technologies, i.e., with the exception of the storage device itself, are described in Section 2.1, namely the Storage Control (Subsection 2.1.1), and the VSC device (Subsection 2.1.2). The Storage Control is responsible of regulating the behavior of the

storage device, varying the active power that it absorbs or provides from/to the network, according to the variations of a regulated variable of the network with respect to a given reference. On the other hand, the VSC connects the storage device (in dc) with a certain bus of the grid (in ac). The dc voltage is converted to ac voltage waveform via the use of power electronic converters that are regulated by the VSC control. Chapter 2 also describes some of the most relevant VSC-based ESSs in Section 2.2. The technologies considered in the thesis are: BES, CAES, FES, SCES and SMES in Subsections 2.2.1-2.2.5. The chapter provides the main features of each storage technology, and presents the largest projects that have been or are being developed for real-world applications. Detailed fundamental-frequency, transient stability models of each technology are also provided.

Chapter 2 highlights the fact that one of the main purposes of the ESSs studied in this thesis is the regulation of a given system frequency. Therefore, a reliable technique to estimate that frequency is needed in power system simulators. With this aim, Chapter 3 defines three approaches to estimate the frequency at different points of the network. These are: the well-known center of inertia in Subsection 3.2.1, which provides information of the global system frequency based on the rotor speeds and inertias of the synchronous machines of the system; the commonly used washout filter in Subsection 3.2.2, which estimates the frequency of a given bus of the system based on the numerical derivative of the bus voltage angle; and a new frequency estimation approach proposed in this thesis in Subsection 3.2.3. The proposed approach is based on the *voltage-divider* formula, and computes the frequencies at every bus of the network. The features of each frequency estimator are listed and illustrated by means of a simple 3-bus test system in Section 3.3. The performance, accuracy and computational efficiency of the three estimation techniques are duly studied and compared in Sections 3.4 and 3.5, based on comprehensive case studies using both benchmark and real-world systems, respectively.

In order to simplify the implementation in power system simulators of all existing technologies of VSC-based ESSs, a generalized model of these devices is proposed in Chapter 4. This model consists of a fixed and reduced set of linear differential algebraic equations and parameters, and is able to reproduce the behavior of all ESS technologies studied in this work with a high level of accuracy. The linearization is carried out only

on the equations that depend on the technology, i.e., the equations that represent the storage device. Therefore, nonlinearities of the common components of the ESS, namely VSC device and controllers are properly taken into account by the proposed generalized model. The validity of this model is duly proven in the case study provided in the chapter, which is based on the WSCC 9-bus system and compares the detailed, the generalized and other commonly used simplified ESS models for a variety of scenarios and technologies.

While the main purpose of the installation of ESSs in power systems is the provision of a variety of ancillary services, ESSs are also expected to be flexible yet reliable against any kind of contingencies and disturbances that may occur in the system, topology and/or regulation goal changes, etc. With this regard, alternatives to the commonly-used PI control for ESSs are being proposed in the literature in recent years. These new and advanced control strategies are aimed at improving the robustness of the PI regulator, and can be based on deterministic techniques, e.g., H-infinity, sliding mode or model predictive controllers, or based on heuristics such as the fuzzy logic control. However, the design of these advanced ESS control strategies is generally highly involved, specially considering the large variety of storage technologies available. With this aim, in Chapter 5 the generalized ESS model proposed in Chapter 4 is used to formulate the PI, H-infinity and sliding mode controllers in Section 5.2. The fixed and reduced set of equations of the generalized ESS model highly simplifies the design of these controllers, and allows their subsequent implementation for the detailed ESS models in a straightforward manner. The performance of the controllers is illustrated and compared in Section 5.3 based on the IEEE 14-bus test system, while Section 5.4 provides a comprehensive comparison of the three controllers based on a stochastic model of the all-island Irish transmission system.

The ancillary services provided by VSC-based ESSs are the main reasons that justify their economical viability. However, their fast response and their capability to provide simultaneously both active and reactive support are expected, as byproduct, to improve the transient stability of the grid. With this aim, Chapter 6 presents a detailed stochastic and statistical analysis of the impact of ESSs on the transient stability of transmission grids. The chapter studies and compares the critical clearing times of a power system with a variety of ESS technologies and network topologies. The latter concerns the

relative positions of faults, storage devices and synchronous machines. The case study provided in Chapter 6 consists of stochastic time-domain simulations carried out for the all-island Irish transmission system that includes a real-world storage device. Simulation are also carried out including Flexible AC Transmission Systems (FACTS) devices, and results are compared with those of ESSs.

Finally, Chapter 7 draws general conclusions and remarks of the overall thesis. Future work directions derived from this thesis are also presented and discussed.

1.3 Publications

1.3.1 Journal Papers

1. F. Milano and Á. Ortega, “Frequency Divider,” *IEEE Transactions on Power Systems*, 2016, (in press, accepted for publication on July 2016).
2. Á. Ortega and F. Milano, “Generalized Model of VSC-based Energy Storage Systems for Transient Stability Analysis,” *IEEE Transactions on Power Systems*, vol. 31, no. 5, pp. 3369-3380, Sept. 2016.
3. Á. Ortega and F. Milano, “Modeling, Simulation and Comparison of Control Techniques for Energy Storage Systems,” *IEEE Transactions on Power Systems*, 2016, (in press, accepted for publication on April 2016).

1.3.2 Conference Papers

Papers closely related to the thesis

1. Á. Ortega and F. Milano, “Design of a Control Limiter to Improve the Dynamic Response of Energy Storage Systems,” in *Proceedings of the Power Engineering Society General Meeting, IEEE*, Denver, CO, USA, July 2015.
2. Á. Ortega and F. Milano, “Comparison of Different Control Strategies for Energy Storage Devices,” in *Proceedings of the Power System Computation Conference (PSCC)*, Genoa, Italy, June 2016.

3. Á. Ortega, P. Mc Namara and F. Milano, “Design of MPC-based Controller for a Generalized Energy Storage System Model,” in *Proceedings of the Power Engineering Society General Meeting, IEEE*, Boston, MA, USA, July 2016.
4. Á. Ortega and F. Milano, “Comparison of Bus Frequency Estimators for Power System Transient Stability Analysis,” in *Proceedings of the International Conference on Power System Technology (POWERCON)*, Wollongong, Australia, Sept. 2016.

Other papers

5. F. Madia Mele, Á. Ortega, R. Zárate-Miñano and F. Milano, “Impact of Variability, Uncertainty and Frequency Regulation on Power System Frequency Distribution,” in *Proceedings of the Power System Computation Conference (PSCC)*, Genoa, Italy, June 2016.
6. P. Mc Namara, Á. Ortega and F. Milano, “Model Predictive Control based AGC for Multi-Terminal DC grids,” in *Proceedings of the Power Engineering Society General Meeting, IEEE*, Boston, MA, USA, July 2016.
7. M. Liu, Á. Ortega, A. C. Melhorn, D. Flynn and F. Milano, “Stability-constrained Unit Commitment with Water Network Loads,” in *Proceedings of the International Conference on Power System Technology (POWERCON)*, Wollongong, Australia, Sept. 2016.

1.3.3 Publications Arising

1. Á. Ortega and F. Milano, “Stochastic Transient Stability Analysis of Transmission Systems with Inclusion of Energy Storage Devices,” *IEEE Power Engineering Society Letters*, submitted in Sept. 2016 and currently under review.

2 | VSC-Based Energy Storage Systems: Overview and Technologies

A general scheme of a VSC-based ESS connected to a power system is depicted in Fig. 2.1. The main objective of ESS is to regulate a measured quantity of the system w , e.g., power flowing through a transmission line, or the frequency of the bus of connection of the ESS. While the storage device is responsible of the active power support, the VSC provides reactive power support by regulating the ac voltage at the bus of connection, and it links the storage device with the grid.

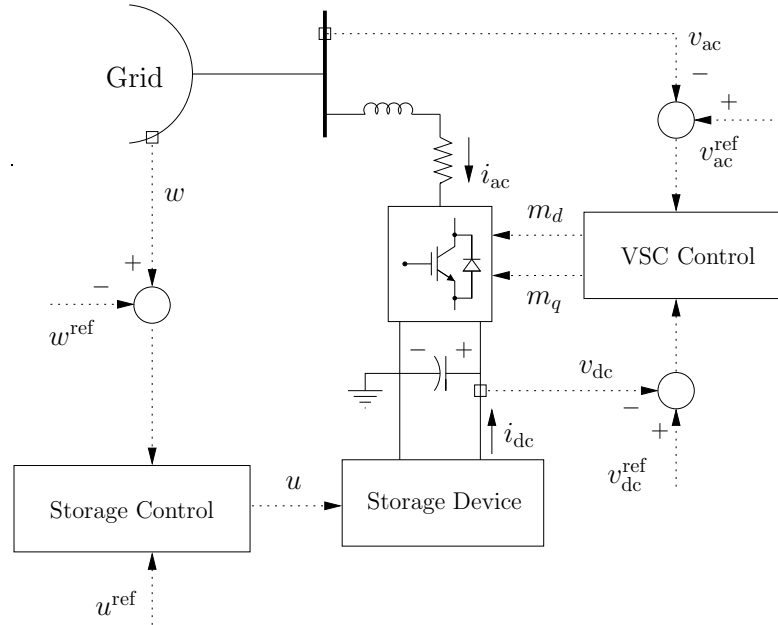


Figure 2.1: Scheme of the ESS connected to a grid.

This chapter presents an overview of the elements that compose the ESS. The schemes, models and assumptions described in this chapter are the base of the work that has been carried out in the remainder of the document. The chapter is organized as follows. Section 2.1 describes the elements that are common to all VSC-based ESSs and do not depend on the technology, namely the VSC device and the controllers. A detailed description of the main features and the averaged models of the different ESS technologies studied is presented in Section 2.2.

2.1 Common Elements of VSC-Based ESSs

This section describes the devices and controllers that are common to all VSC-based ESSs connected to a grid (see Fig. 2.1). The general scheme of the Storage Control, as well as the detailed models of the VSC device and its controllers are presented in Sections 2.1.1 and 2.1.2, respectively. These models are obtained based on a careful selection of well-assessed models for transient stability analysis.

2.1.1 Storage Control

The charge/discharge process of the storage device is regulated by the Storage Control (see Fig. 2.2). The input signal of the control is the error between the actual value of w , and a reference value (w^{ref}). If $w = w^{\text{ref}}$, the storage device is inactive and its stored energy is thus kept constant. For $w \neq w^{\text{ref}}$, the storage device injects active power into the ac bus through the VSC (discharge process) or absorbs power from the ac bus (charge process). The typical configuration of this controller includes a dead-band and low-pass filter blocks that are responsible of reducing the sensitivity of the storage control to small, high-frequency perturbations such as noises. The aim of these blocks is to reduce the number of charge/discharge operations, thus increasing the life of the ESS [81]. Note that, for illustration, the control scheme shown in Fig. 2.2 is based on a PI regulator. Other alternatives to this controller are presented in Chapter 5.

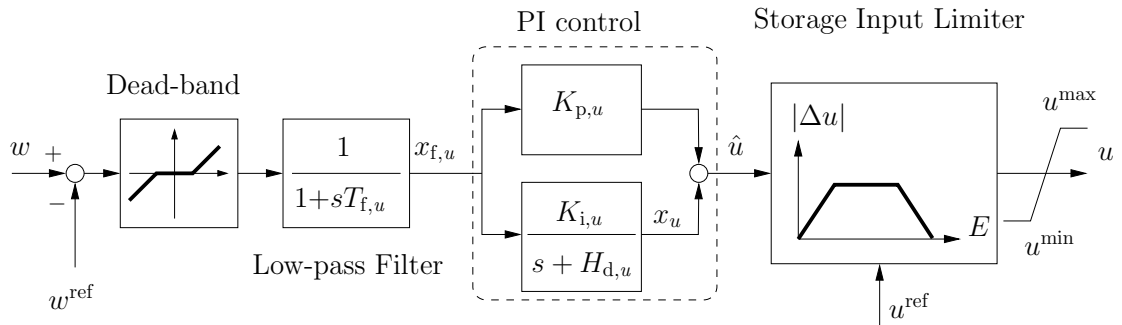


Figure 2.2: Storage control scheme.

The scheme shown in Fig. 2.2 includes also a block referred to as Storage Input Limiter (SIL) [91]. The purpose of the SIL is to reduce the impact of energy saturations of the storage device on system transients. This block takes the actual value of the energy stored in the device, E , and regulates accordingly the input controlled variable of the storage device, u , as follows:

$$u = \begin{cases} \frac{E - E^{\min}}{E_{\text{thr}}^{\min} - E^{\min}} \Delta u + u^{\text{ref}} & \text{if } E^{\min} \leq E \leq E_{\text{thr}}^{\min} \quad \text{and} \quad \Delta u > 0 \\ \frac{E^{\max} - E}{E^{\max} - E_{\text{thr}}^{\max}} \Delta u + u^{\text{ref}} & \text{if } E_{\text{thr}}^{\max} \leq E \leq E^{\max} \quad \text{and} \quad \Delta u < 0 \\ \hat{u} & \text{otherwise} \end{cases} \quad (2.1)$$

where u^{ref} is the value of u such that the storage device is disabled; $\Delta u = \hat{u} - u^{\text{ref}}$; E^{\min} and E^{\max} are the minimum and maximum storable energy in the ESS, respectively; and E_{thr}^{\min} and E_{thr}^{\max} define the minimum and maximum energy thresholds, respectively, that are computed as follows:

$$\begin{aligned} E_{\text{thr}}^{\min} &= E^{\min} + \mu^{\min} (E^{\max} - E^{\min}) \\ E_{\text{thr}}^{\max} &= E^{\max} - \mu^{\max} (E^{\max} - E^{\min}) \end{aligned} \quad (2.2)$$

where μ^{\min} and μ^{\max} are the coefficients that define the regions in which the SIL is operational. In this work, a symmetrical limiter is assumed, hence $\mu^{\min} = \mu^{\max} = \mu$; where $\mu \in (0, 0.5]$.

The sign of Δu is taken into account in (2.1) with the aim of reducing its value, and hence altering the regulation capability of the storage control, only if the ESS is close to its maximum storable energy and the storage device is charging, or if the energy is close to the minimum value and the ESS is discharging. If any other condition is satisfied, the storage control can regulate the input quantity w as expected. The robustness and effectiveness of the SIL are verified through time domain simulations in Appendix A.

2.1.2 Voltage Sourced Converter

The connection of the ac side of the grid with the dc side of the storage device is achieved through a VSC device [27, 125, 16, 26]. The VSC decouples the storage device from the grid frequency, and allows the installation of any kind of ESS technology. In this way, a SMES (which essentially is a dc RL circuit), and a FES (in which the main component is an asynchronous motor) can be connected in the same way to the grid. Moreover, similar control techniques can be applied regardless the technology used. Figure 2.3 illustrates the usual configuration of the VSC device. VSCs include a bidirectional converter (e.g., based on Integrated Gate Bipolar Transistors (IGBTs)) which offers both *turn-on* and *turn-off* control capability, a transformer, and a condenser. The transformer provides galvanic insulation, whereas the condenser maintains the voltage level at the dc side of the converter.

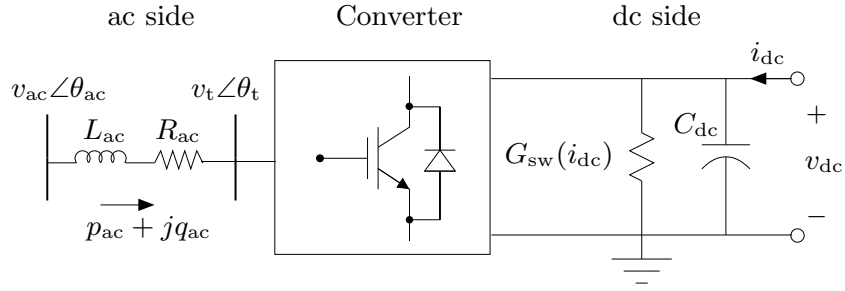


Figure 2.3: VSC scheme.

Figure 2.4 shows the block diagram representation of both the converter and the inner current control loop of the VSC. After transforming the three-phase equations to a rotating dq -frame¹, the dynamics of the ac side of the VSC depicted in Fig. 2.3 become:

$$\begin{aligned} R_{ac}i_{ac,d} + L_{ac}\frac{di_{ac,d}}{dt} &= \omega_{ac}L_{ac}i_{ac,q} + v_{ac,d} - v_{t,d} \\ R_{ac}i_{ac,q} + L_{ac}\frac{di_{ac,q}}{dt} &= -\omega_{ac}L_{ac}i_{ac,d} + v_{ac,q} - v_{t,q} \end{aligned} \quad (2.3)$$

where $R_{ac} + jL_{ac}$ is the aggregated impedance of the converter reactance and transformer; $v_{t,d} = m_d v_{dc}/2$; $v_{t,q} = m_q v_{dc}/2$; and ω_{ac} is the frequency of the grid voltage, \bar{v}_{ac} . Note that, using the rotating frame, (2.3) represents a two-input/two-output system where $v_{ac,d/q}$ and $v_{t,d/q}$ are the external and control inputs, respectively, and $i_{ac,d/q}$ are the

¹A detailed description of the conversion of the three-phase notation to the dq -frame representation is provided in [27].

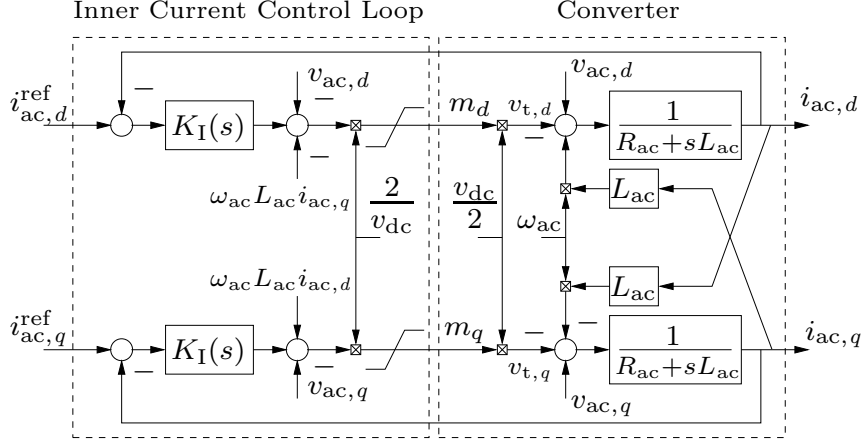


Figure 2.4: Block diagram of the VSC inner current control and converter in the dq -frame.

outputs. The average model of the converter used in this thesis has been duly justified and accepted in the literature, e.g., [76, 108]. Its theoretical foundation and formulation are beyond the scope of this thesis.

The dq -reference frame rotates with the same speed as the grid voltage phasor \bar{v}_{ac} . In practice, this can be achieved through a phase-locked loop (PLL) [32], which is a control system that forces the angle of the dq -frame, θ_{dq} , to track the angle θ_{ac} . The PLL is typically composed of a phase detector (PD), a loop filter (LF), and a voltage controlled oscillator (VCO). The PLL scheme used in this work is depicted in Fig. 2.5.

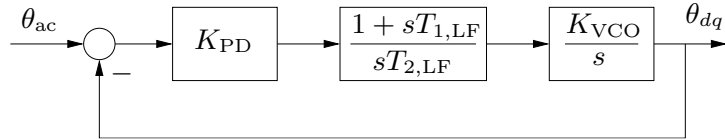


Figure 2.5: PLL scheme.

The grid voltage \bar{v}_{ac} can, thus, be expressed in the dq -frame as follows:

$$v_{ac,d} + jv_{ac,q} = v_{ac}(\cos(\theta_{ac} - \theta_{dq}) + j \sin(\theta_{ac} - \theta_{dq})) \quad (2.4)$$

To ensure zero steady-state error in the regulation, the controller $K_I(s)$ of Fig. 2.4 is designed as a PI control, as follows [27]:

$$K_I(s) = \frac{R_{ac} + sL_{ac}}{sT_I} \quad (2.5)$$

where T_I is the time-constant of the closed-loop step response.

The power balance between the dc and the ac sides of the converter is imposed by:

$$p_{ac} + v_{dc}i_{dc} - p_{loss} - \frac{1}{2}C_{dc}\frac{d(v_{dc}^2)}{dt} = 0 \quad (2.6)$$

where $p_{ac} = \frac{3}{2}(v_{ac,d}i_{ac,d} + v_{ac,q}i_{ac,q})$; $\frac{1}{2}C_{dc}\frac{d(v_{dc}^2)}{dt}$ is the energy variation in the capacitor; and $p_{loss} = \frac{3}{2}R_{ac}i_{ac}^2 + G_{sw}(i_{dc})v_{dc}^2$ are the losses of the converter, where the first term accounts for the ac circuit losses with $i_{ac}^2 = i_{ac,d}^2 + i_{ac,q}^2$; and $G_{sw}(i_{dc})$ represents the dc circuit and switching losses of the converter, and is obtained from a given constant conductance, G_0 , and the quadratic ratio of the actual current to the nominal one, as follows [1]:

$$G_{sw}(i_{dc}) = G_0 \left(\frac{i_{dc}}{i_{dc}^{nom}} \right)^2 \quad (2.7)$$

Finally, the outer controllers used to regulate the dc and ac voltages of the VSC are depicted in Fig. 2.6. The purpose of the PI regulator in the dc loop is to maintain the dc voltage constant, while the compensator of the ac loop will filter the lowest and highest frequencies of the grid ac voltage disturbances. Note that, by using the dq -frame representation, the controllers of the two voltages are decoupled. In [27], an alternative to the dc loop in Fig. 2.6 is proposed, where the regulated signal is the error between the square of the dc voltage, v_{dc}^2 , and its corresponding reference, $(v_{dc}^{ref})^2$.

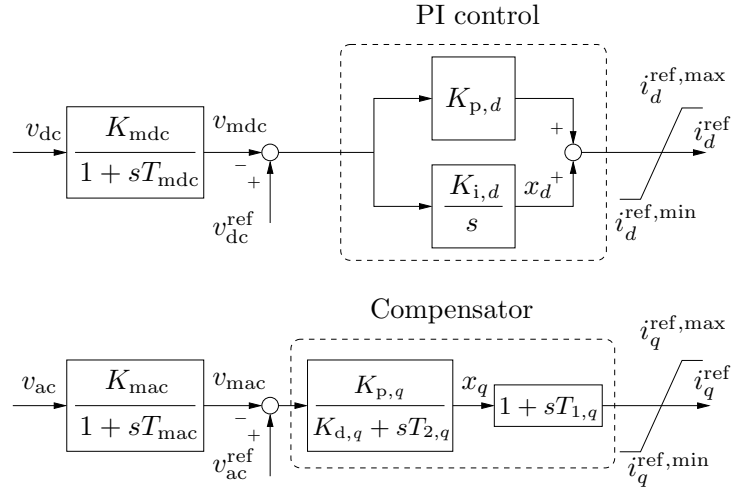


Figure 2.6: Outer dc and ac voltage controllers of the VSC.

2.2 Features and Modeling of Different ESS Technologies

This section describes the most common VSC-based ESS technologies and that are studied in this work, namely BES (Section 2.2.1), CAES (Section 2.2.2), FES (Section 2.2.3), SCES (Section 2.2.4), and SMES (Section 2.2.5) [15, 100, 94, 9, 54]. Detailed fundamental-frequency, transient stability models of these storage technologies are also provided.

2.2.1 Battery Energy Storage

In the battery cells that compose a BES system, a reversible chemical reaction is used to convert directly chemical energy into electrical energy. The main advantage of BESs is their versatility, since they can be installed in a wide range of sizes by connecting cells in series (increasing the operational voltage of the battery) and/or in parallel (for higher current operations). There also exists a large variety of battery technologies to be chosen, depending on the requirements and specifications of the system. Among these, there are lead-acid batteries, nickel-cadmium, lithium-ion, etc. The main drawbacks of BESs are their limited number of charge/discharge cycles ($\leq 5,000$), a relatively high degradation during their life time, and their intrinsic self-discharge rates. The largest BES system installed in Europe is located in Feldheim (northeastern Germany): a lithium-ion based battery storage plant with 10 MW of peak power and 10 MWh of capacity [31, 44]. In Texas (USA), Duke Energy is developing an advanced lead-acid BES project of 36 MW/14.4 MWh [36, 41].

Model of the BES

A commonly-used model to represent the dynamics of a rechargeable battery cell is the Shepherd model [105, 115]:

$$\begin{aligned}
 \dot{Q}_{e,B} &= i_B/3600 \\
 \dot{i}_{m,B} &= \frac{i_B - i_{m,B}}{T_{m,B}} \\
 0 &= v_{oc,B} - v_{p,B}(Q_{e,B}, i_{m,B}) + v_{e,B}e^{-\beta_{e,B}Q_{e,B}} - R_{i,B}i_B - v_B
 \end{aligned} \tag{2.8}$$

where $Q_{e,B}$ is the extracted capacity in Ah; $i_{m,B}$ is the battery current i_B passed through a low-pass filter with time constant $T_{m,B}$; $v_{oc,B}$, $v_{p,B}$ and $v_{e,B}$ are the open-circuit, polarization and exponential voltages, respectively; $\beta_{e,B}$ is the exponential zone time constant inverse; $R_{i,B}$ is the internal battery resistance; and v_B is the battery voltage.

The variation of the polarization voltage $v_{p,B}$ with respect to $i_{m,B}$ and $Q_{e,B}$ is given by:

$$v_{p,B}(Q_{e,B}, i_{m,B}) = \begin{cases} \frac{R_{p,B}i_{m,B} + K_{p,B}Q_{e,B}}{\text{SOC}_B} & \text{if } i_{m,B} > 0 \text{ (discharge)} \\ \frac{R_{p,B}i_{m,B}}{q_{e,B} + 0.1} + \frac{K_{p,B}Q_{e,B}}{\text{SOC}_B} & \text{if } i_{m,B} \leq 0 \text{ (charge)} \end{cases} \tag{2.9}$$

where $R_{p,B}$ and $K_{p,B}$ are the polarization resistance and polarization constant, respectively; and SOC_B is the state of charge of the battery which is defined as:

$$\text{SOC}_B = \frac{Q_{n,B} - Q_{e,B}}{Q_{n,B}} = 1 - q_{e,B} \tag{2.10}$$

with $Q_{n,B}$ the maximum battery capacity.

The connection of the BES to the VSC is achieved by means of a dc/dc converter, represented by the following average model [45]:

$$\begin{aligned}
 0 &= (1 - 2S_B)v_{dc} - n_{s,B}v_B \\
 i_{dc} &= -(1 - 2S_B)n_{p,B}i_B
 \end{aligned} \tag{2.11}$$

where S_B is the duty cycle of the converter; and $n_{p,B}$ and $n_{s,B}$ are the number of parallel and series connected battery cells, respectively.

2.2.2 Above Ground Compressed Air Energy Storage

Small-scale CAES (μ CAES) systems compress and store air in an above ground vessel or tank, consuming electricity from the grid. This air is later expanded in a turbine to produce electricity. This technology is characterized by a long life time (30-40 years), high energy density and power rate (up to 10 MW), and faster response times with respect to large, underground CAESs [2]. Moreover, the location of μ CAESs is not restricted by orographic constraints, as opposed to underground CAESs. The main limitations of μ CAESs are their high costs per kW and kWh, and their relatively low efficiency (up to 70%). A project to install an above ground CAES with 10 MW of peak power and 20 MWh of capacity is being developed in the city of New York (USA) [37, 86].

Model of the μ CAES

The basic configuration of a μ CAES is represented in Fig. 2.7 [120]. The air is injected into the tank by means of a compressor operated by an asynchronous motor, and extracted from it through a turbine driven by an asynchronous generator. Both the compressor and the turbine are connected in parallel to the dc link of the VSC through ac/dc converters.

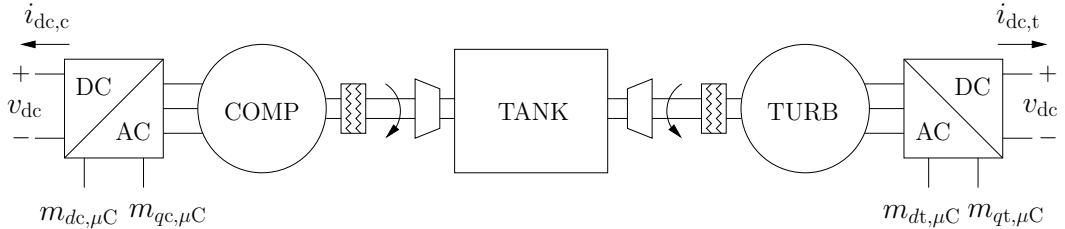


Figure 2.7: Scheme of a μ CAES.

The air is modeled as an ideal gas. Therefore the relation between the temperature, Θ , the pressure, Π and the Volume, V , is defined by:

$$\Pi V = n_{\text{air}} R \Theta \quad (2.12)$$

where n is the number of moles of air, and $R = 8.314 \times 10^{-5} \frac{\text{m}^3 \text{ bar}}{\text{mol K}}$ is the ideal gas constant .

Defining $n_{\text{air}} = \rho M_{\text{air}}/\pi_m$, with $\rho = 1.2041 \text{ kg/m}^3$ the air density; $\pi_m = 0.02896 \text{ kg/mol}$ the molecular weight of air; and M_{air} the amount of displaced air in m^3 , the variation of the pressure inside the tank can be thus calculated from (2.12), as follows:

$$\dot{\Pi}_2 = \frac{\rho R \Theta_2}{\pi_m V_{\mu C}} Q_{\mu C} \quad (2.13)$$

where Π_2 is the pressure inside the tank (in bar); Θ_2 is the temperature of the air inside the tank (in Kelvin); $V_{\mu C}$ is the volume of the tank (in m^3); and $Q_{\mu C} = \dot{M}_{\text{air}}$ is the air flow through the compressor/turbine (in m^3/s).

Assuming that both compression and expansion of air are polytropic processes [120], the behavior of the compressor of the μCAES is described by the following set of nonlinear equations (turbine equations are similar and are omitted):

$$0 = \frac{\gamma}{\gamma - 1} \Pi_1 Q_{\mu C} \left[\left(\frac{\Pi_2}{\Pi_1} \right)^{\frac{\gamma-1}{\gamma}} - 1 \right] - P_{\text{ef},\mu C} \quad (2.14)$$

$$H_{\mu C} \dot{\Omega}_{r,\mu C} = (T_{\text{el},\mu C} - T_{m,\mu C}) \quad (2.15)$$

$$0 = P_{\text{ef},\mu C} - \eta_{m,\mu C} P_{m,\mu C} \quad (2.16)$$

$$0 = \frac{P_{m,\mu C}}{\Omega_{r,\mu C}} - T_{m,\mu C} \quad (2.17)$$

$$0 = T_{\text{el},\mu C} \Omega_{r,\mu C} - P_{\text{el},\mu C} \quad (2.18)$$

$$0 = \frac{\omega_{s,\mu C} - \omega_{r,\mu C}}{\omega_{s,\mu C}} - \sigma_{\text{sr},\mu C} \quad (2.19)$$

$$0 = 0.5 n_{p,\mu C} \Omega_{r,\mu C} - \omega_{r,\mu C} \quad (2.20)$$

where $\gamma = 1.4$ is the air specific heat ratio; Π_1 is the atmospheric pressure; $P_{\text{ef},\mu C}$, $P_{m,\mu C}$ and $P_{\text{el},\mu C}$ are the effective, mechanical and electrical powers of the compressor, respectively; $T_{m,\mu C}$ and $T_{\text{el},\mu C}$ are the mechanical and electrical torques of the motor, respectively; $\Omega_{r,\mu C}$ and $\omega_{r,\mu C}$ are the mechanical and electrical rotor speeds of the compressor, respectively; $\sigma_{\text{sr},\mu C}$ is the motor slip; and $\eta_{m,\mu C}$, $n_{p,\mu C}$, $\omega_{s,\mu C}$, $H_{\mu C}$ are the mechanical efficiency, number of poles, electrical stator speed and machine inertia constant of the compressor, respectively.

The model considered for the electric machines of the compressor and the turbine is a standard 5th-order squirrel-cage induction machine model [66]. Using the generator convention, and the dq -frame representation, the voltages of the stator and rotor of the

μ CAES induction machine can be written as follows:

$$\begin{aligned}
v_{ds,\mu C} &= -R_{s,\mu C}i_{ds,\mu C} - \omega_{s,\mu C}\psi_{qs,\mu C} + \dot{\psi}_{ds,\mu C} \\
v_{qs,\mu C} &= -R_{s,\mu C}i_{qs,\mu C} + \omega_{s,\mu C}\psi_{ds,\mu C} + \dot{\psi}_{qs,\mu C} \\
v_{dr,\mu C} &= -R_{r,\mu C}i_{dr,\mu C} - \sigma_{sr,\mu C}\omega_{s,\mu C}\psi_{qr,\mu C} + \dot{\psi}_{dr,\mu C} = 0 \\
v_{qr,\mu C} &= -R_{r,\mu C}i_{qr,\mu C} + \sigma_{sr,\mu C}\omega_{s,\mu C}\psi_{dr,\mu C} + \dot{\psi}_{qr,\mu C} = 0
\end{aligned} \tag{2.21}$$

where the subscripts s and r stand for stator and rotor variables, respectively; $v_{\mu C}$, $R_{\mu C}$ and $i_{\mu C}$ are the machine voltage, resistance and current, respectively; and $\psi_{\mu C}$ is the flux linkage.

The expressions of the flux linkages are given by:

$$\begin{aligned}
\psi_{ds,\mu C} &= -(L_{s,\mu C} + L_{m,\mu C})i_{ds,\mu C} - L_{m,\mu C}i_{dr,\mu C} \\
\psi_{qs,\mu C} &= -(L_{s,\mu C} + L_{m,\mu C})i_{qs,\mu C} - L_{m,\mu C}i_{qr,\mu C} \\
\psi_{dr,\mu C} &= -(L_{r,\mu C} + L_{m,\mu C})i_{dr,\mu C} - L_{m,\mu C}i_{ds,\mu C} \\
\psi_{qr,\mu C} &= -(L_{r,\mu C} + L_{m,\mu C})i_{qr,\mu C} - L_{m,\mu C}i_{qs,\mu C}
\end{aligned} \tag{2.22}$$

where $L_{s,\mu C}$, $L_{r,\mu C}$ and $L_{m,\mu C}$ are the stator, rotor and mutual inductances, respectively.

The models of the ac/dc converters and their controllers are similar to those of the VSC, which are duly described in Subsection 2.1.2.

Finally, according to (2.14) and (2.15), the energy stored in the μ CAES can be expressed as follows:

$$E_{\mu C} = \frac{\gamma}{\gamma - 1} \Pi_1 V_{\mu C} \left[\left(\frac{\Pi_2}{\Pi_1} \right)^{\frac{\gamma-1}{\gamma}} - 1 \right] + H_{\mu C} \Omega_{r,\mu C}^2 \tag{2.23}$$

In (2.23), the main term is that related to the pressure Π_2 , as expected. However, for completeness, the term related to the mechanical rotor speed $\Omega_{r,\mu C}$ is also included.

Taking into account that the compressor and the turbine have similar sizes, it is assumed that both compressor and turbine electrical machines have same parameters. Therefore, it is modeled only one equivalent electrical machine capable of working, depending on the sign of $Q_{\mu C}$, as a compressor ($Q_{\mu C} > 0$) or a turbine ($Q_{\mu C} < 0$).

2.2.3 Flywheel Energy Storage

Flywheels store energy by accelerating a rotating mass connected to an electrical machine, thus increasing its rotational kinetic energy. FES systems are promising due to its high efficiency ($\sim 90\%$), high number of cycles in their life time (up to 100,000), low maintenance and operation costs, flexibility in their locations and environmental conditions, and modular designs for large capacities. High capital costs and self-discharge rates due to frictions losses ($\geq 55\%$ per day) are the main drawbacks of this technology. The biggest operational FES system has been installed in Pennsylvania (USA), and is able to provide 20 MW for 15 minutes (5 MWh) [38, 13, 14].

Model of the FES

The scheme of a FES connected to the dc side of the VSC is depicted in Fig. 2.8. The electrical equations of the FES induction machine are similar to those of the CAES ones (2.15-2.22) in Subsection 2.2.2 [66, 102].

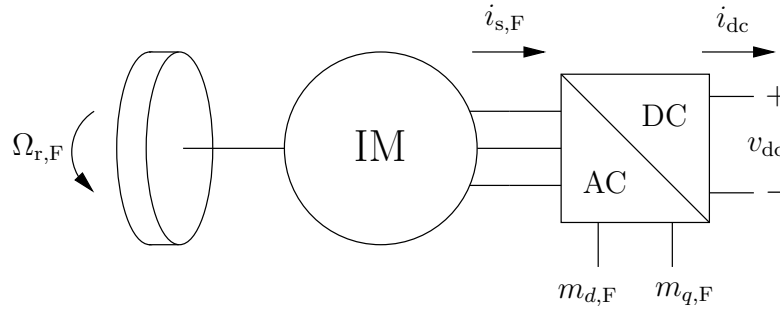


Figure 2.8: Scheme of a FES.

The mechanical equations of the induction machine are the following:

$$\begin{aligned} T_{el,F} &= \psi_{dr,F} i_{qr,F} - \psi_{qr,F} i_{dr,F} \\ H_F \dot{\Omega}_{r,F} &= (T_{m,F} - T_{el,F}) - D_F \Omega_{r,F} \end{aligned} \quad (2.24)$$

with $T_{el,F}$ and $T_{m,F}$ the electromechanical and mechanical torques, respectively; $\Omega_{r,F}$ the mechanical rotor speed of the machine; and H_F and D_F the inertia constant and rotor damping of the FES, respectively.

The active and reactive powers generated/absorbed by the machine are defined by [69]:

$$\begin{aligned} P_F &= v_{ds,F}i_{ds,F} + v_{qs,F}i_{qs,F} \\ Q_F &= v_{qs,F}i_{ds,F} - v_{ds,F}i_{qs,F} \end{aligned} \quad (2.25)$$

An ac/dc converter is used to connect, through its current output i_{dc} , the flywheel device with the dc side of the VSC. The converter, as well as its controllers, are modeled in a similar way as the VSC described in Subsection 2.1.2.

Finally, the actual energy stored in the FES can be computed as follows:

$$E_F = H_F \Omega_{r,F}^2 \quad (2.26)$$

2.2.4 Super Capacitor Energy Storage

Super capacitors (also known as ultra capacitors, double-layer capacitors and electrochemical capacitors) store energy by accumulating electrical charges in the double layer between the two conductors that compose the capacitor. SCESs are characterized by a high power density compared to BESs (up to 25 times bigger), a power response of tens of milliseconds, a nearly unlimited number of charge/discharge cycles, and an efficiency of up to 95%. On the other hand, SCESs have a self-discharge of about 5% per day, and the energy density of these devices (≤ 10 Wh/kg) is low compared with batteries (70-250 Wh/kg). There are currently works aimed at increasing super capacitors energy density, to make them competitive with batteries. For example, [30] highlights a method to increase the energy density of SCESs up to 41 Wh/kg.

Model of the SCES

Figure 2.9 shows the scheme of an SCES connected to the VSC through a bidirectional dc/dc converter (buck-boost) [61]. In the boost operation mode, the energy is delivered from the storage device to the grid, while in the buck mode, the energy is stored in the SCES.

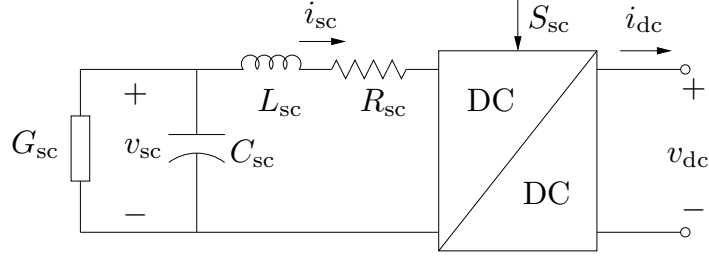


Figure 2.9: Scheme of a SCES.

The model that describes both the buck and the boost operation modes is as follows:

$$\begin{aligned}
 C_{sc}\dot{v}_{sc} &= -(i_{sc} + G_{sc}v_{sc}) \\
 L_{sc}\dot{i}_{sc} &= (v_{sc} - i_{sc}R_{sc} - v_{dc}S_{sc}) \\
 i_{dc} &= S_{sc}i_{sc}
 \end{aligned} \tag{2.27}$$

where S_{sc} is the logic state of the switches of the converter. Assuming average variable values, S_{sc} is continuous and represents the duty cycle of the converter.

Finally, the energy stored in the SCES is as follows:

$$E_{sc} = \frac{1}{2}C_{sc}v_{sc}^2 + \frac{1}{2}L_{sc}i_{sc}^2 \tag{2.28}$$

As in Subsection 2.2.2, both terms related to the energy stored in the SCES have been considered, despite the fact that the term related to the inductance L_{sc} is expected to be much smaller than the term related to the capacitance C_{sc} .

2.2.5 Superconducting Magnetic Energy Storage

In SMES systems, the energy is stored in the magnetic field created in a superconducting coil with solenoid or toroid configuration. The dc current flowing through the coil, which can be stored for long periods due to its low internal losses, can be delivered to the grid in few milliseconds, and vice versa. SMESs systems are also characterized by a high efficiency ($\geq 95\%$), they can provide up to 100 MW of peak power, and have a high lifetime. The main drawback of SMESs is their high installation and operational costs. High temperature superconductors can reduce the cooling related costs of SMESs in the near future. The largest installed SMES (Center of Advanced Power Systems, Florida State University) has a capacity of 100 MJ, and can provide 100 MW peak and ± 50 MW oscillatory power [71].

Model of the SMES

Figure 2.10 depicts the scheme of a SMES [56, 5, 81]. The SMES is connected in parallel to the VSC throughout a dc/dc chopper converter. The SMES stores magnetic energy and injects it into the network according to the duty cycle applied to the converter.

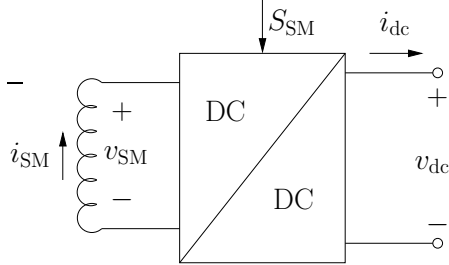


Figure 2.10: Scheme of the SMES and the boost converter.

The dynamics of the coil and the dc/dc converter are represented by the circuit equations:

$$\begin{aligned} \dot{i}_{SM} &= -\frac{v_{SM}}{L_{SM}} \\ 0 &= (1 - 2S_{SM})v_{dc} - v_{SM} \\ i_{dc} &= (1 - 2S_{SM})i_{SM} \end{aligned} \quad (2.29)$$

where all voltages and currents are average values; L_{SM} is the inductance of the superconducting coil; and S_{SM} is the duty cycle of the dc/dc converter.

Finally, the energy stored in the SMES is given by:

$$E_{SM} = \frac{1}{2}L_{SM}i_{SM}^2 \quad (2.30)$$

3 | Frequency Estimator Modeling: Introducing the Frequency Divider

3.1 Motivation

The conventional power system model for Transient Stability Analysis (TSA) is based on the assumption of quasi-steady-state phasors for voltages and currents. The crucial hypothesis on which such a model is defined is that the frequency required to define all phasors and system parameters is constant and equal to its nominal value. This model is appropriate as long as only the rotor speed variations of synchronous machines are needed to regulate the system frequency through standard primary and secondary frequency regulators. In recent years, however, an increasing number of devices other than synchronous machines are expected to provide frequency regulation. These include, among others, distributed energy resources such as wind and solar generation [6, 99, 74, 19, 85]; flexible loads providing load demand response [101, 73]; HVDC transmission systems [112, 83, 25]; and ESSs [124, 111, 70]. However, these devices do not generally impose the frequency at their connection point with the grid. There is thus, from a modeling point of view, the need to define with accuracy the local frequency at every bus of the network.

With regard to the work presented in this thesis, in real-world applications where the ESSs are responsible of regulating a given frequency of the system (e.g., of the bus of connection of the ESS), this frequency can be measured locally and used straightforwardly as input signal of the storage control of Subsection 2.1.1. However, from the simulation point of view, these devices pose the problem of properly defining the frequency signal to be used as input of the regulators. In fact, conventional electromechanical models for TSA structurally neglect frequency variations in transmission lines and loads. On the other hand, fully-fledged electromagnetic models, which would easily allow determining the frequency at any point of the system, are too computational demanding as the time scales of interest when dealing with frequency regulations are in the order of seconds/minutes, not milliseconds.

The most common way to estimate the system frequency in transient stability analysis is the evaluation of the Center of Inertia (COI), which is an arithmetic mean of rotor speeds of synchronous machines weighted through their inertia constants. The frequency of the COI is well-accepted and widely used in the literature on transient and frequency stability analysis [121, 96]. While the COI is particularly useful to define the frequency of clusters of coherent machines, it cannot capture local oscillations and is thus not adequate to implement and simulate the frequency controllers discussed above.

Another common approach consists in defining the numerical derivative of the phase angle of bus voltage phasors through some sort of filtering, e.g., a Washout Filter (WF). This approach was first discussed in [57] along with the COI model, and is commonly used in proprietary software tools for power system simulation, e.g., [35].

The issues of the numerical differentiation of voltage angles are well known. The literature on this subject has mainly focused on the definition of analytical expressions, e.g., [88], or more accurate numerical methods, e.g., [53], to define the derivative of the bus voltage angles. The common starting point of the two references above, as well as of this chapter, is the expression that links bus voltage phasors and current injections at buses through the network admittance matrix. This chapter proposes an analytical expression which is not model-dependent as that given in [88] and is considerably simpler, but consistent with standard approximations used in power system models for TSA. This accurate yet simple and computationally inexpensive formula is used to estimate the frequency at all buses of the system.

The remainder of this chapter is organized as follows. Section 3.2 describes the mathematical formulations of the frequency estimators studied in this work, namely the COI, the WF, and the proposed Frequency Divider (FD) formula in Subsections 3.2.1, 3.2.2 and 3.2.3, respectively. Section 3.3 illustrates, through a simple example, the validity of the FD and tests it considering different scenarios and load models. Section 3.4 provides a comparison of the performance of frequency control devices when their input signal is provided by the three frequency estimators. Section 3.5 presents simulation results based on two real-world systems, namely a 1,479-bus model of the all-island Irish system and a 21,177-bus model of the European ENTSO-E transmission system. Finally, Section 3.6 draws conclusions.

3.2 Modeling of Different Frequency Estimators

This section presents the model of different frequency estimators for power system simulators, namely COI, WF and FD in Subsections 3.2.1, 3.2.2 and 3.2.3, respectively.

3.2.1 Center of Inertia

The frequency of the COI, ω_{COI} , is a weighted arithmetic average of the rotor speeds of synchronous machines that are connected to a transmission system. Assuming a set \mathcal{G} of synchronous generators, the expression to compute the COI is:

$$\omega_{\text{COI}} = \frac{\sum_{j \in \mathcal{G}} H_j \omega_j}{\sum_{j \in \mathcal{G}} H_j} \quad (3.1)$$

where ω_j are rotor speeds and H_j are inertia constants.

The inertia-weighted nature of the COI makes this quantity particularly suited to study inter-area oscillations among machine clusters. However, local variations of the machines, especially those characterized by a small inertia, are lost. One can thus expect that the COI is not fully adequate to simulate local frequency controllers. This fact is duly discussed in the case study of Section 3.4 and in [90]. Moreover, from the modeling point of view, it is unrealistic to assume that distributed generators, microgrids and consumers will receive the instantaneous signal of the COI frequency from the system operator. The frequency is actually very likely measured locally, using well-assessed techniques based on the sampling of ac quantities (see, for example, [129]). Thus, it is important to capture local variations of the frequency to properly model the response of such devices.

3.2.2 Washout Filter

The numerical derivative of the bus voltage phase angles is another well-known approach to estimate the frequency of ac transmission systems [57, 88, 53]. As opposed to the COI, this technique can properly capture local oscillation modes but is prone to numerical issues. Figure 3.1 shows a typical implementation of the numerical derivative, i.e., a washout filter and a low pass filter.

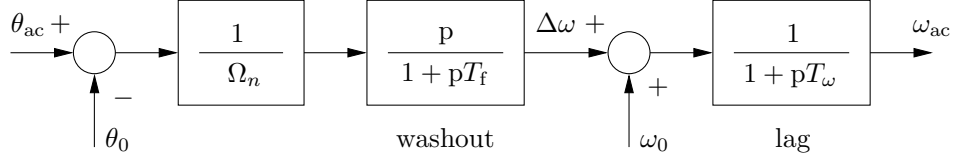


Figure 3.1: Numerical derivative of the bus voltage phase angle composed of a washout and a low pass filters. θ_0 is the initial value of the bus voltage phase angle in radians and ω_0 is the synchronous frequency in pu.

Differential equations of the WF are as follows:

$$\begin{aligned} px_\theta &= \frac{1}{T_f} \left(\frac{1}{\Omega_n} (\theta_{ac} - \theta_0) - x_\theta \right) \\ p\omega_{ac} &= \frac{1}{T_w} (\omega_0 + \Delta\omega - \omega_{ac}) \end{aligned} \quad (3.2)$$

where θ_0 is the initial bus voltage phase angle (e.g., the phase angle as obtained with the power flow analysis); Ω_n is the system nominal frequency in rad/s; ω_0 is the synchronous frequency in pu (typically, $\omega_0 = 1$ pu); T_f and T_w are the time constants of the washout and of the low-pass filters, respectively; x_θ is the state variable of the washout filter; $p(\cdot)$ indicates the total time derivative; and $\Delta\omega = px_\theta$.

In case of polar coordinates, to compute the frequency variation $\Delta\omega$, the bus voltage phase angle θ_{ac} has to be defined first. Instead of computing directly θ_{ac} , which might lead to numerical issues, one can define two fictitious state variables, namely $\sin \theta_{ac}$ and $\cos \theta_{ac}$, whose dynamics are defined as follows [35]:

$$\begin{aligned} p(\cos \theta_{ac}) &= \frac{1}{T_f} (v_{ac,d}/v_{ac} - \cos \theta_{ac}) \\ p(\sin \theta_{ac}) &= \frac{1}{T_f} (v_{ac,q}/v_{ac} - \sin \theta_{ac}) \end{aligned} \quad (3.3)$$

where $v_{ac} = \sqrt{v_{ac,d}^2 + v_{ac,q}^2}$. Then, $\Delta\omega$ is obtained as:

$$\Delta\omega = \begin{cases} \frac{p(\sin \theta_{ac})}{\Omega_n \cos \theta_{ac}}, & \text{if } |\cos \theta_{ac}| > |\sin \theta_{ac}|, \\ -\frac{p(\cos \theta_{ac})}{\Omega_n \sin \theta_{ac}}, & \text{otherwise.} \end{cases} \quad (3.4)$$

The interested reader can find in [35] a similar version of (3.3) but for voltages expressed in rectangular coordinates.

The washout filter block is necessary as the input quantity, i.e., the bus voltage phase angle θ_{ac} , is an algebraic variable and thus can *jump* as a consequence of discrete events, such as faults and line outages. The discontinuity of the derivative of θ_{ac} is the main issue of the WF approach. The low pass filter mitigates numerical issues but also introduces a delay that can be detrimental for the performance of local frequency controllers. A commonly accepted trade-off between accuracy and numerical efficiency is obtained with $T_f = 3/\Omega_n$ s and $T_w = 0.05$ s, where Ω_n is the nominal frequency of the system in rad/s. These are the values used in the simulations of this thesis.

3.2.3 Frequency Divider

The COI and the WF are two well-accepted techniques to estimate the frequency of ac transmission systems. However, as discussed above, they show relevant technical, theoretical and/or numerical drawbacks. An alternative approach is proposed in this thesis, namely the FD formula, based on the augmented admittance matrices of the system and on the assumption that the frequency along the impedances of transmission lines varies as in a *continuum matter* where synchronous machine rotor speeds define boundary conditions [80]. While the assumptions made in this section are common in transmission system studies, they generally cannot be applied in distribution systems. However, the frequency deviations from node to node in distribution systems are very small, and therefore they are not considered in this thesis.

The very starting point in the development of the FD formula is the augmented admittance matrix, with inclusion of synchronous machine internal impedances as it is commonly defined for short-circuit analysis [7]. System currents and voltages are linked as follows:

$$\begin{bmatrix} \bar{\mathbf{i}}_G \\ \bar{\mathbf{i}}_B \end{bmatrix} = \begin{bmatrix} \bar{\mathbf{Y}}_{GG} & \bar{\mathbf{Y}}_{GB} \\ \bar{\mathbf{Y}}_{BG} & \bar{\mathbf{Y}}_{BB} + \bar{\mathbf{Y}}_{G0} \end{bmatrix} \begin{bmatrix} \bar{\mathbf{e}}_G \\ \bar{\mathbf{v}}_B \end{bmatrix} \quad (3.5)$$

where $\bar{\mathbf{v}}_B$ and $\bar{\mathbf{i}}_B$ are bus voltages and current injections, respectively, at network buses; $\bar{\mathbf{i}}_G$ are generator current injections; $\bar{\mathbf{e}}_G$ are generator electromotive forces (EMFs) behind the internal generator impedance; $\bar{\mathbf{Y}}_{BB}$ is the standard network admittance matrix; $\bar{\mathbf{Y}}_{GG}$, $\bar{\mathbf{Y}}_{GB}$ and $\bar{\mathbf{Y}}_{BG}$ are admittance matrices obtained using the internal impedances of the synchronous machines; and $\bar{\mathbf{Y}}_{G0}$ is a diagonal matrix that accounts for the internal

impedances of the synchronous machines at generator buses. All quantities in (3.5) depend on the frequency. However, the dependency of the admittance matrices above on the frequency is neglected.

Let us assume that load current injections $\bar{\mathbf{i}}_B$ can be expressed as a linear function of the bus voltages $\bar{\mathbf{v}}_B$:

$$\bar{\mathbf{i}}_B = -\bar{\mathbf{Y}}_{B0}\bar{\mathbf{v}}_B \quad (3.6)$$

which leads to rewrite (3.5) as follows:

$$\begin{bmatrix} \bar{\mathbf{i}}_G \\ \mathbf{0} \end{bmatrix} = \begin{bmatrix} \bar{\mathbf{Y}}_{GG} & \bar{\mathbf{Y}}_{GB} \\ \bar{\mathbf{Y}}_{BG} & \bar{\mathbf{Y}}_{BB} + \bar{\mathbf{Y}}_{G0} + \bar{\mathbf{Y}}_{B0} \end{bmatrix} \begin{bmatrix} \bar{\mathbf{e}}_G \\ \bar{\mathbf{v}}_B \end{bmatrix} \quad (3.7)$$

Bus voltages $\bar{\mathbf{v}}_B$ are thus a function of generator EMFs and can be computed explicitly:

$$\begin{aligned} \bar{\mathbf{v}}_B &= -[\bar{\mathbf{Y}}_{BB} + \bar{\mathbf{Y}}_{G0} + \bar{\mathbf{Y}}_{B0}]^{-1}\bar{\mathbf{Y}}_{BG}\bar{\mathbf{e}}_G \\ &= \bar{\mathbf{D}}\bar{\mathbf{e}}_G \end{aligned} \quad (3.8)$$

At this point, the main assumption that is made in [80] is applied, i.e., that the variations of the frequency are “slow”, at least when considering electromechanical transient stability models. Hence:

$$p\bar{v}_h \approx j\omega_h\bar{v}_h \quad (3.9)$$

where $\omega_h = \omega_0 + \Delta\omega_h$ is the frequency at bus h . Expressions similar to (3.9) hold for all other ac quantities in the systems, i.e., generator EMFs $\bar{\mathbf{e}}$ and currents. For example:

$$p\bar{e}_i \approx j\omega_i\bar{e}_i \quad (3.10)$$

where ω_i is the rotor speed of generator i .

The approximated time derivatives (3.9) and (3.10) are used along with network constraints (3.8) to determine the FD. In particular, differentiating (3.8) with respect to time leads to:

$$p\bar{\mathbf{v}}_B = p[\bar{\mathbf{D}} \cdot \bar{\mathbf{e}}_G] = p\bar{\mathbf{D}} \cdot \bar{\mathbf{e}}_G + \bar{\mathbf{D}} \cdot p\bar{\mathbf{e}}_G \quad (3.11)$$

$$\Rightarrow p\bar{\mathbf{v}}_B \approx \bar{\mathbf{D}} \cdot p\bar{\mathbf{e}}_G \quad (3.12)$$

$$\Rightarrow \frac{d}{dt}\bar{\mathbf{v}}_B + j\omega_0\bar{\mathbf{v}}_B \approx \bar{\mathbf{D}} \cdot \frac{d}{dt}\bar{\mathbf{e}}_G + j\omega_0\bar{\mathbf{D}} \cdot \bar{\mathbf{e}}_G \quad (3.13)$$

$$\Rightarrow j \text{diag}(\Delta\omega_B) \bar{\mathbf{v}}_B \approx j\bar{\mathbf{D}} \cdot \text{diag}(\Delta\omega_G) \bar{\mathbf{e}}_G \quad (3.14)$$

where, in (3.11), it is assumed that $p\bar{\mathbf{D}} \approx \mathbf{0}$, i.e., constant transmission system, load and generator parameters; in (3.13), (3.8) is used to remove the equal terms $j\omega_0\bar{\mathbf{v}}_B$ and $j\omega_0\bar{\mathbf{D}} \cdot \bar{\mathbf{e}}_G$; $\text{diag}(\cdot)$ is a matrix where diagonal elements are the elements of its argument vector; and $\Delta\omega_B$ and $\Delta\omega_G$ are defined as:

$$\Delta\omega_B = \omega_B - \omega_0 \cdot \mathbf{1} \quad (3.15)$$

$$\Delta\omega_G = \omega_G - \omega_0 \cdot \mathbf{1}$$

The set of equations (3.14) and (3.15) allows determining the bus voltage frequencies ω_B . In fact, $\bar{\mathbf{D}}$ are parameters and ω_G , $\bar{\mathbf{v}}_B$ and $\bar{\mathbf{e}}_G$ are variables determined by integrating the set of Differential Algebraic Equations (DAEs) describing the power system. Equation (3.14) can be significantly simplified without a relevant loss of accuracy. The following approximations and assumptions are applied:

- $\bar{\mathbf{v}}_B \approx \mathbf{1}$ pu and $\bar{\mathbf{e}}_G \approx \mathbf{1}$ pu;
- The conductances of the elements of all admittance matrices utilized to compute $\bar{\mathbf{D}}$ are negligible, e.g., $\bar{\mathbf{Y}}_{BB} \approx j\mathbf{B}_{BB}$;
- Load admittances are negligible with respect to transmission system ones, hence, $|\bar{\mathbf{Y}}_{B0}| \ll \text{diag}(|\bar{\mathbf{Y}}_{BB}|)$.

Moreover, the condition $\omega_0 = 1$ pu usually holds. All simplifications above are motivated by usual assumptions and typical parameters of transmission systems. Substituting frequency deviations with the expressions in (3.15), (3.14) becomes:

$$\omega_B = \mathbf{1} + \mathbf{D}(\omega_G - \mathbf{1}) \quad (3.16)$$

where

$$\mathbf{D} = -(\mathbf{B}_{BB} + \mathbf{B}_{G0})^{-1}\mathbf{B}_{BG} \quad (3.17)$$

Equation (3.16) is the sought FD expression.

A final important remark is the following. From the computational point of view, (3.16) might not be the most adequate expression to implement in practice. In fact, while \mathbf{B}_{BB} , \mathbf{B}_{G0} and \mathbf{B}_{BG} tend to be extremely sparse matrices, \mathbf{D} is not. For this reason, the use of (3.16) is impractical for a computer-based implementation of the FD and may cause memory errors on common workstations if large systems are studied. Hence, an *acausal* expression was implemented as follows:

$$\mathbf{0} = (\mathbf{B}_{BB} + \mathbf{B}_{G0}) \cdot (\boldsymbol{\omega}_B - \mathbf{1}) + \mathbf{B}_{BG} \cdot (\boldsymbol{\omega}_G - \mathbf{1}) \quad (3.18)$$

Equation (3.18), not (3.16), has been used to obtain the results of the case studies presented in the remainder of this chapter. (3.18) shows another interesting property. If the estimated frequency $\boldsymbol{\omega}_B$ is used as input of frequency regulation devices, then $\boldsymbol{\omega}_G$ will depend also on $\boldsymbol{\omega}_B$. Adding the constraint (3.18) to the set of DAEs of the power system model allows taking into account properly this dependency. The interested reader can find in [113] an extensive discussion on causality and its implications on the modeling of physical systems.

3.3 Example: 3-Bus System

In this section, the FD formula (3.16) derived in the previous section is illustrated through a simple example. Such an example will serve to justify why (3.16) is called *frequency divider* and to compare the dynamic behavior of (3.16) with respect to conventional WFs as well as discuss its conceptual difference with respect to the ω_{COI} .

Let us consider the simple radial system shown in Figure 3.2. The lossless connection, with total reactance $x_{hk} = x_{hi} + x_{ik}$, represents the series of the internal reactances of the machines, and series reactances of the step-up transformers and the transmission line. Hence, the frequencies at buses h and k , say ω_h and ω_k , respectively, are the rotor speeds of the synchronous generators.

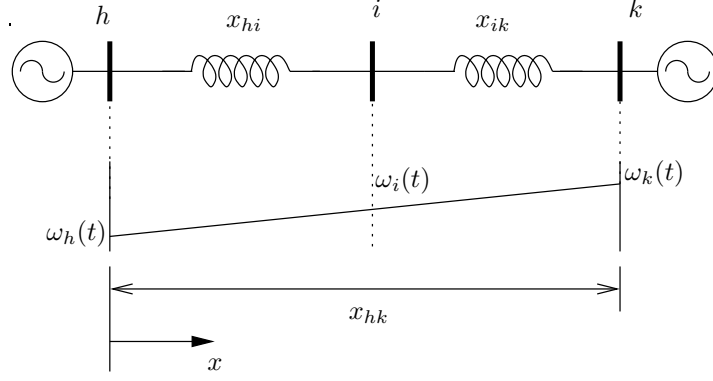


Figure 3.2: Two-machine radial system.

Applying the FD formula (3.16):

$$\begin{aligned}
 \omega_i(t) &= 1 + \mathbf{D} \cdot \begin{bmatrix} \omega_h(t) - 1 \\ \omega_k(t) - 1 \end{bmatrix} = 1 - (\mathbf{B}_{BB} + \mathbf{B}_{G0})^{-1} \mathbf{B}_{BG} \cdot \begin{bmatrix} \omega_h(t) - 1 \\ \omega_k(t) - 1 \end{bmatrix} \\
 &= 1 - \left[\frac{1}{x_{hi}} + \frac{1}{x_{ik}} \right]^{-1} \begin{bmatrix} -\frac{1}{x_{hi}} & -\frac{1}{x_{ik}} \end{bmatrix} \cdot \begin{bmatrix} \omega_h(t) - 1 \\ \omega_k(t) - 1 \end{bmatrix} \\
 &= 1 + \frac{x_{hi}x_{ik}}{x_{hk}} \begin{bmatrix} \frac{1}{x_{hi}} & \frac{1}{x_{ik}} \end{bmatrix} \begin{bmatrix} \omega_h(t) - 1 \\ \omega_k(t) - 1 \end{bmatrix} = \frac{x_{ik}}{x_{hk}} \cdot \omega_h(t) + \frac{x_{hi}}{x_{hk}} \cdot \omega_k(t)
 \end{aligned} \tag{3.19}$$

It is worth noticing that, as a direct consequence of (3.16), the instantaneous frequency $\omega_i(t)$ at a generic point i between the boundaries h and k is a linear interpolation between $\omega_h(t)$ and $\omega_k(t)$ (see lower part of Fig. 3.2). Such a linear relation is consistent with the assumption to assume steady-state conditions in the distribution of the frequency along the transmission line. Note also that (3.19) has the same formal structure of a voltage divider of a resistive circuit where the frequencies function as the voltage potential. Hence the chosen name to define (3.16).

The remainder of this section discusses the accuracy of (3.19) through numerical simulations based on the 3-bus system shown in Fig. 3.3, which includes two synchronous machines and a load. The impedances of the transmission lines include the step up transformers and transmission lines ($\bar{z} = 0.025 + j0.075$ pu). A standard model for TSA is firstly considered, where transmission lines are lumped and modeled as constant impedances and generator flux dynamics are neglected. Generators are equal and are modeled as a 6th order synchronous machine, a IEEE Type DC1 Automatic Voltage

Regulator (AVR) and a Turbine Governor (TG) with inclusion of servo and reheater models [78]. The load is modeled as a constant admittance. The disturbance is a three-phase fault that occurs at bus 3 at $t = 1$ s and is cleared after 150 ms by opening one of the two lines connecting buses 1 and 3.

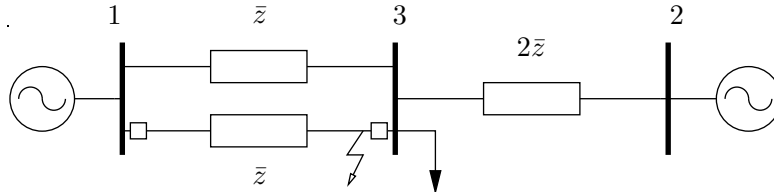


Figure 3.3: 3-bus system.

Figure 3.4 shows the transient behavior of synchronous machine rotor speeds, the ω_{COI} , and the estimated frequency at the load bus using the proposed FD approach. Since the inertias of the machines are equal, oscillations are averaged out from the value of ω_{COI} as it can be readily deduced by the COI frequency expression given in Subsection 3.2.1. On the other hand, the estimated bus frequency $\omega_{\text{Bus } 3}$ provided by (3.19) shows oscillations in phase with $\omega_{\text{Syn } 1}$, as expected, since the load bus is electrically closer to generator 1 ($x_{13} < x_{32}$). Clearly, the frequency of the COI is also unable to capture the proximity to any machine of the system. ω_{COI} can thus be used only as an indication of the overall *trend* of the system frequency but could be inadequate if utilized as a control signal for devices that regulate the frequency as those discussed in the introduction of this chapter.

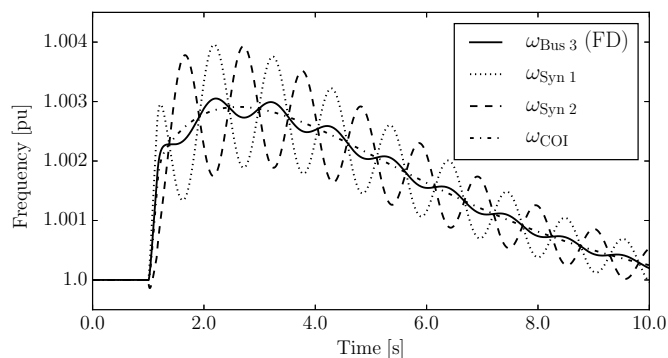


Figure 3.4: 3-bus system – Synchronous machine rotor speeds, COI frequency, and frequency at bus 3 estimated based on the proposed FD approach.

The model and the dynamics of the load connected to bus 3 are not included in (3.19) and need not to be known to define $\omega_{\text{Bus } 3}$. This is one of the major differences of the proposed approach with respect to [88]. Clearly, load models and dynamics do impact on the transient behavior of the system, which includes the machines at buses 1 and 2 whose rotor speeds are required to compute $\omega_{\text{Bus } 3}$. Load models are thus *implicitly* taken into account in the FD formula.

The trajectories of the frequency estimation at the load bus for the 3-bus system are now compared using the proposed FD and the conventional WF described in Subsection 3.2.2. Figure 3.5 shows the results obtained with a more detailed model of the system considering 8th order models of synchronous machines and dq -frame dynamic models of the transmission lines and the load at bus 3. All parameters are the same as in Fig. 3.4, which is obtained using standard transient stability models. This more accurate model shows that, during the fault, the frequency drops due to the effect of machine fluxes. After the fault occurrence and clearance, the frequency also shows small high-frequency oscillations which are properly captured by (3.19). These oscillations cause severe numerical issues along the entire simulation in the behavior of the WF – see also [53] for an in-depth discussion on this matter – as well as a significant delay of the filter to show the over-frequency after the line disconnection.

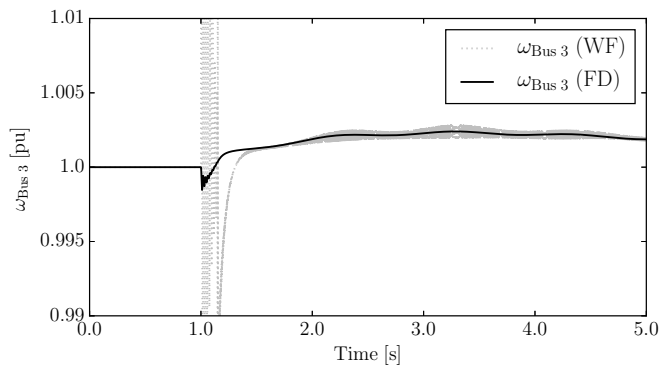


Figure 3.5: 3-bus system – Frequency at bus 3 estimated with FD and the conventional WF. The system is simulated using the fully-fledged dq -axis model.

As indicated in Subsection 3.2.3, one of the main assumptions on which the FD formula is based, is that load currents can be neglected in (3.5). This is a common assumption in most analyses based on the admittance matrix, e.g., short-circuit calculations [7]. Moreover, in standard TSA, loads are approximated using constant impedances (see, for example, [8]), which, by the way, could be easily included in (3.16).

In the remainder of this section, it is shown that the effect of loads, including non-linear and dynamic ones is actually negligible for the calculation of the bus frequencies. With this aim, the dynamic response of the 3-bus system of Fig. 3.3 is considered again following a short-circuit at bus 3, and the constant admittance load is substituted with a static voltage- and frequency-dependent load (see Fig. 3.6) and a 5th-order dq -axis model of an asynchronous motor (see Fig. 3.7).

The exponential voltage- and frequency-dependent load is modeled as follows [78, 51]:

$$\begin{aligned} p_i &= p_0 \left(\frac{v_i}{v_0} \right)^{\alpha_p} \omega_i^{\beta_p} \\ q_i &= q_0 \left(\frac{v_i}{v_0} \right)^{\alpha_q} \omega_i^{\beta_q} \end{aligned} \quad (3.20)$$

In the simulations carried out to obtain Fig. 3.6, the frequency ω_i is estimated using the WF or the proposed FD formula, depending on the model considered. The parameters p_0 , q_0 and v_0 are the initial load active and reactive powers and voltage magnitude at bus i , respectively, determined with the power flow analysis. The parameters α_p , β_p , α_q and β_q resemble those of an aluminum plant and are based on [18]. Finally, the dynamic model of the asynchronous motor is based on [66].

Simulation results confirm that the FD formula (3.16) is accurate as it is able to estimate the frequency at the load bus similarly to the WF but avoiding the numerical issues of the latter. It is interesting to note that the time evaluation of the frequency in the case of the asynchronous motor is consistently different from the static load model. The load model, in fact, does impact on the overall dynamic behavior of the system and, hence, also on the variations of rotor speeds of synchronous machines. Since the FD is based on such variations, load models are indirectly taken into account in (3.16).

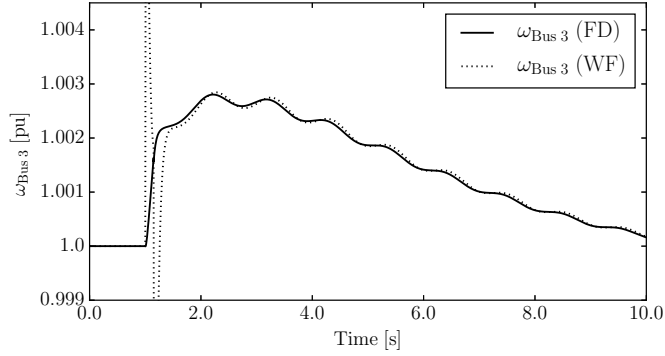


Figure 3.6: 3-bus system – Frequency at bus 3 estimated with the FD and the conventional WF. The load is modeled as a frequency-dependent load representing an aluminum plant ($\alpha_p = 1.8$, $\alpha_q = 2.2$, $\beta_p = -0.3$, $\beta_q = 0.6$).

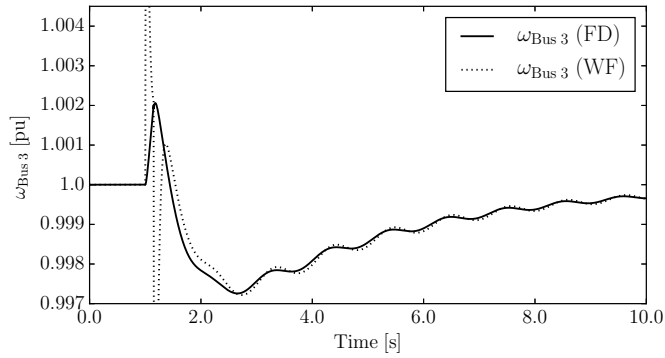


Figure 3.7: 3-bus system – Frequency at bus 3 estimated with the FD and the conventional WF. The load is a squirrel cage induction motor with a 5th-order dq -axis model.

Apart from the simulations included in this section, other nonlinear load models (e.g., induction motors) and several different scenarios have been considered. Moreover, other bigger test networks such as the IEEE 14-bus system and the New England 39-bus, 10-machine system have been considered to test the performance of frequency controlled devices whose input signal is provided by each of the frequency estimators described in this section, and results are provided in the remainder of this chapter. In every test, results were always consistent and similar to those shown in this section. It can be concluded that the proposed FD formula is accurate and that the approximations discussed in Section 3.2.3, including that related on load models, are reasonable.

3.4 Comparison of Different Frequency Estimators: Frequency Controlled Loads

This section compares the performance of frequency control devices in a power system when their input signal is provided by the COI, WF and FD. With this aim Thermostatically Controlled Loads (TCLs), which are dynamic loads with temperature control, are considered for the comparison [51]. These can be air conditioning systems, industrial refrigerators or heating systems. In most cases, the reference temperature is fixed to an assigned value. There are, however, prototypes of TCLs that include a measure of the system frequency and that vary the reference temperature in order to reduce frequency deviations [67, 109, 73]. The control scheme of the TCL is depicted in Fig. 3.8. The meaning of the variables are the following: Θ is the load temperature (lumped model); Θ_a is the ambient temperature; g is the equivalent load conductance, v is the load terminal voltage; and P the consumed active power.

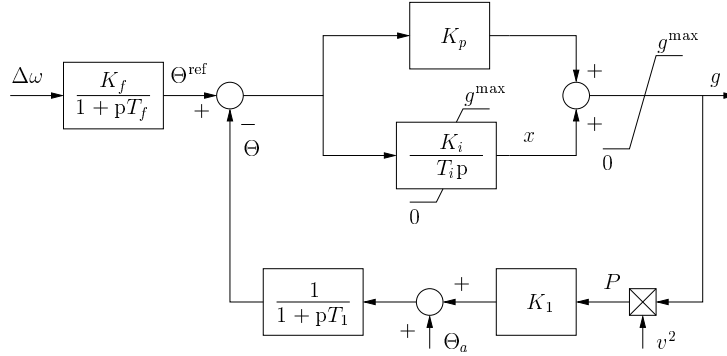


Figure 3.8: Thermostatically controlled load with frequency control.

The gain K_1 and the maximum conductance g^{\max} are determined based on the initial values of the voltage, v_0 , and the active power, p_0 , as follows:

$$K_1 = \frac{\Theta^{\text{ref}} - \Theta_a}{p_0}$$

$$g^{\max} = K_L g_0 \quad (3.21)$$

where $g_0 = \frac{p_0}{v_0^2}$ and K_L is the ceiling conductance output ratio ($K_L < 1$ for cooling systems and $K_L > 1$ for heating systems).

In this study, two benchmark networks are used: the IEEE 14-bus system (Subsection 3.4.1), and the New England 39-bus, 10-machine system (Subsection 3.4.2). All simulations and plots provided in this chapter, as well as in the remainder of the document, have been obtained using DOME [77]. The Dome version utilized in this case study is based on Python 3.4.1; ATLAS 3.10.1 for dense vector and matrix operations; CVXOPT 1.1.8 for sparse matrix operations; and KLU 1.3.2 for sparse matrix factorization. All simulations were executed on a server mounting 40 CPUs and running a 64-bit Linux OS.

3.4.1 IEEE 14-Bus Test System

This subsection considers the IEEE 14-bus test system (see Fig. 3.9) for the simulations. This benchmark network consists of 2 synchronous machines and 3 synchronous compensators, 2 two-winding and 1 three-winding transformers, 15 transmission lines and 11 loads. The system also includes AVRs, TGs and an Automatic Generation Control (AGC). All dynamic data of the IEEE 14-bus system as well as a detailed discussion of its transient behavior can be found in [65].

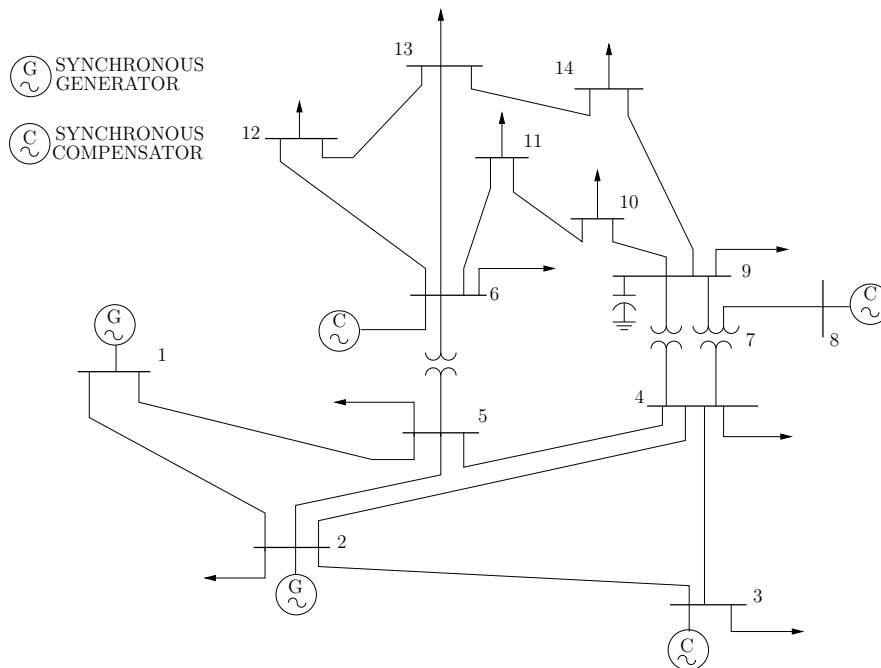


Figure 3.9: IEEE 14-bus test system.

For this scenario, primary and secondary frequency regulation are not included in order to study the effect of the frequency regulation of the TCLs solely. The contingency is the outage of the line connecting buses 2 and 4 in base loading conditions, as well as with 20% of overload. The amount of TCLs in the system is 30% of the total load.

Base Loading Conditions

Figure 3.10 shows the rotor speed of the synchronous machine at bus 2, the frequency of the bus estimated by the WF and the FD, and the frequency of the COI, for the base case loading conditions and without TCLs. While both WF and FD estimators show a trend similar to the rotor speed of the machine, the signal provided by the FD appears to be more accurate, since it includes oscillations of same period and similar amplitude than those of the rotor speed. On the other hand, the COI “filters” such oscillations, providing only information of the average frequency variation.

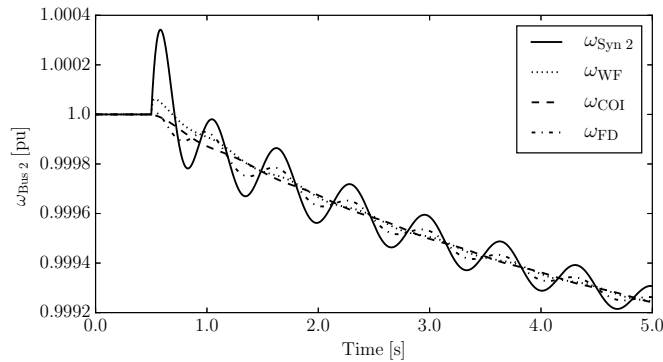


Figure 3.10: Frequency of bus 2 when TCLs are not included.

The differences in the estimated frequencies appear to be negligible when including the TCLs, as shown in Fig. 3.11. The rotor speed of the machine in bus 2 is depicted for the cases without and with TCLs. In the latter case, the dynamic response of TCLs is compared in three scenarios, corresponding to using as control input signals the frequency estimation provided by the WF, the COI and the FD, respectively.

The inclusion of the TCLs reduces the frequency drop by about 50% for the three cases. While in this case the transient response of the system does not appear to be affected by the model of the frequency estimation, one cannot conclude that this is always the case. Next subsection proves, in fact, that depending on the loading level the choice of the input signal of the TCLs can provide a considerably different performance of these devices, and therefore, a different behavior of the whole system.

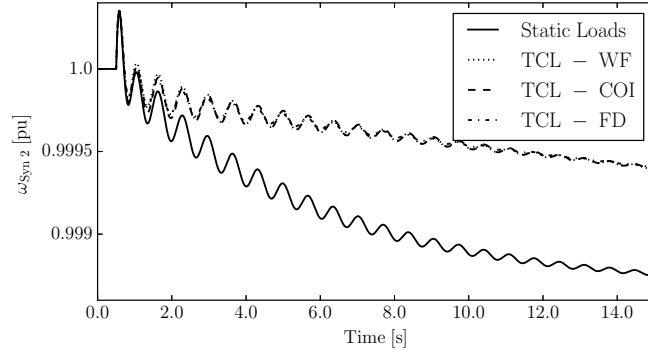


Figure 3.11: Rotor speed of the synchronous generator in bus 2 when TCLs are included.

20% Load Increase

Figure 3.12 is obtained for a 20% increase of the load with respect to the base case without TCLs and shows the trajectories of the rotor speed of the machine at bus 2 with the signals given by the WF, the COI and the FD.

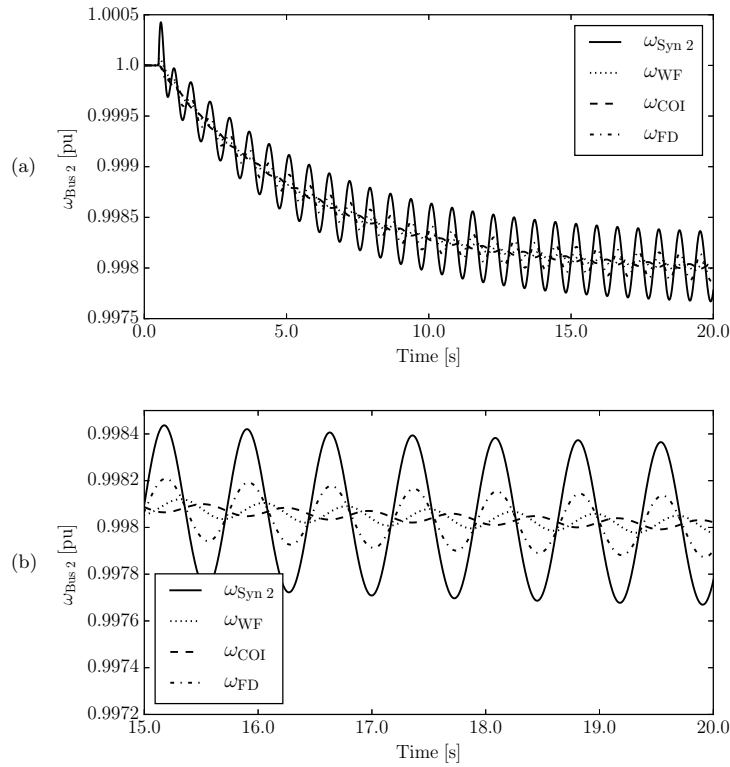


Figure 3.12: Frequency of bus 2 with 20% of system overload without TCLs.

Undamped oscillations can be observed due to the presence of a limit cycle in Fig. 3.12(a). From Fig. 3.12(b), it can be seen that the FD is again the most accurate,

while the WF includes a delay in the signal, and the COI contains counter-phase oscillations due to the large size of the synchronous machine at bus 1. Moreover, depending of the chosen frequency estimation technique, considerably different input signals are introduced into the TCLs controllers. This is shown in Fig. 3.13, where the estimated frequencies at the load bus 14 are compared.

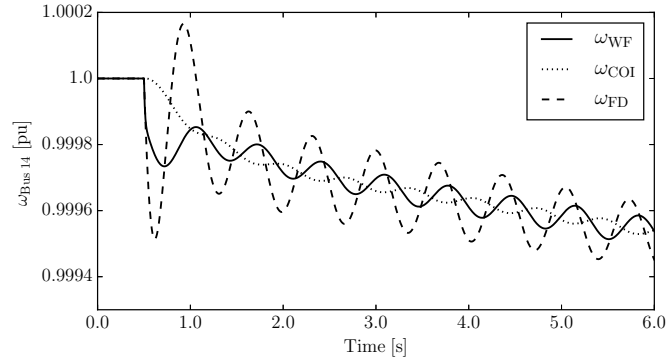


Figure 3.13: Estimated frequency at bus 14 using WF, FD and the COI.

Finally, the rotor speed of the machine at bus 2 is shown in Fig. 3.14, which is obtained including TCLs in the system. The frequency drop is again reduced by about 50%. However, while the WF and the COI signals lead to a stationary limit cycle, the usage of the FD indicates that oscillations are actually damped. It is worth noticing that the only difference in the model is the formula to estimate the frequency signal sent to the TCL. This difference in the frequency signal affects the response of frequency control devices such as the TCLs studied in this section, thus leading to a different behavior of the overall system. In this case, the WF and the COI appear to be more conservative from the control point of view. This is a consequence of the fact that these models do not capture the variations of local bus frequencies as accurately as the FD.

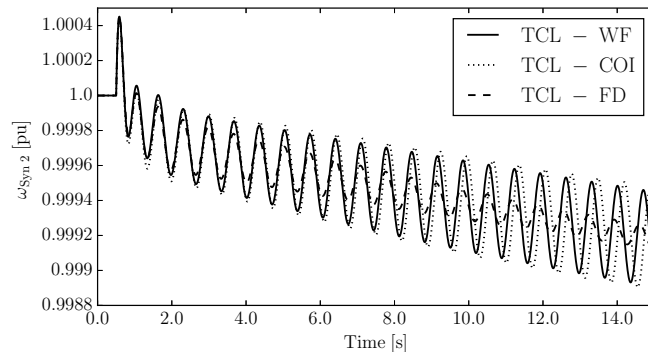


Figure 3.14: Rotor speed of the synchronous generator in bus 2 with 20% of system overload and TCLs.

3.4.2 New England 39-Bus, 10-Machine Test System

The single-line diagram of the New England 39-bus, 10-machine test system is depicted in Fig. 3.15. This benchmark network contains 19 loads totaling 7,316.5 MW and 1,690.9 MVar of active and reactive power, respectively (20% load increase with respect to the base case is assumed). The system model also includes generator controllers such as primary voltage regulators, as well as both primary and secondary frequency regulation (TGs and AGC). Dynamic data of the New England 39-bus, 10-machine system can be found in [59]. The contingency is a three-phase fault at bus 21, cleared by the opening of the line connecting buses 16 and 21 after 160 ms. TCLs are the 20% of the total load.

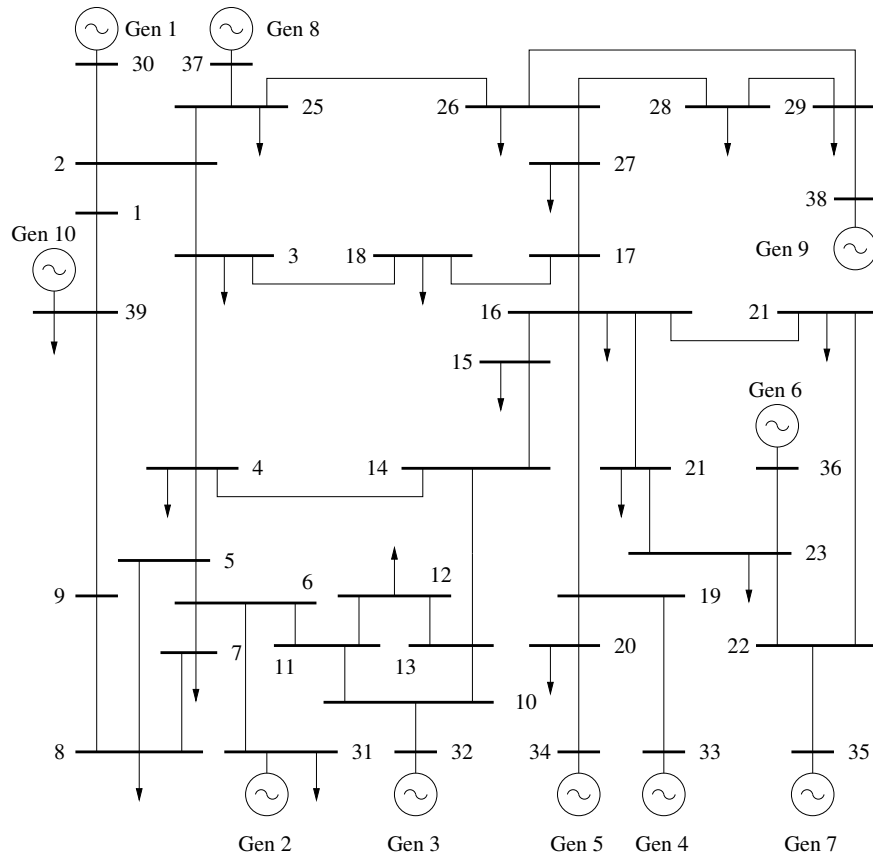


Figure 3.15: New England 39-bus, 10-machine system.

Figure 3.16 shows the rotor speed of the machine at bus 31 (Gen 2) without TCLs, and with TCLs considering the three control input signals, namely FD, WF and COI. Three different models of the synchronous machines of the system are compared: the one-axis 3rd order model (Fig. 3.16(a)), the Sauer and Pai's 6th order model (Fig. 3.16(b)), and the fully-fledged 8th order model (Fig. 3.16(c)) [78].

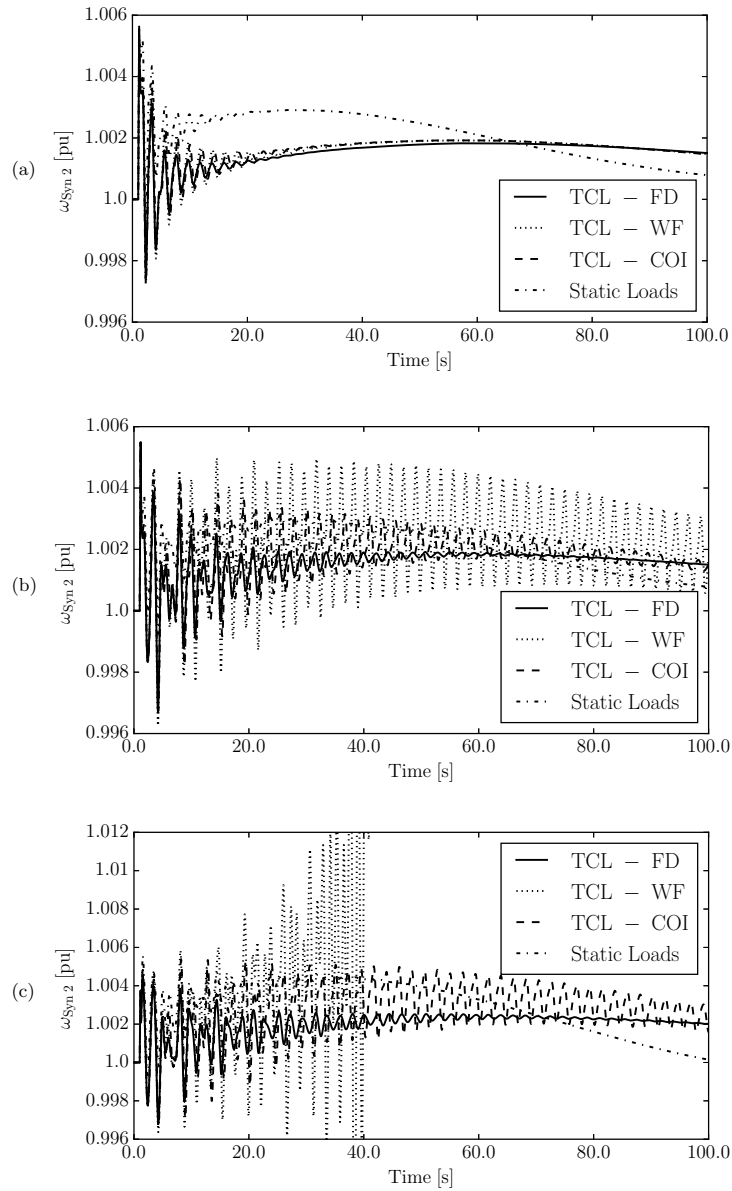


Figure 3.16: Rotor speed of the synchronous generator in bus 31 (Gen 2). (a) 3rd order synchronous machine model; (b) 6th order synchronous machine model; (c) 8th order synchronous machine model.

Figure 3.16(a) shows that including TCLs into the system allows reducing the frequency variations due to the fault. The TCLs reduces the damping of dominant modes. Such modes appear to be slightly better damped if the model includes the FD signal.

Figures 3.16(b) and 3.16(c) show the response of the system for more detailed and accurate models of the synchronous machines. In these cases, the dynamic interaction of the machine transient and subtransient dynamics with the TCLs causes poorly damped frequency oscillations. It is interesting to note that, when considering stator flux dynamics and the WF signal (see Fig. 3.16(c)) such oscillations become unstable and lead the system to collapse. On the other hand, the TCLs controller coupled to the FD shows that oscillations are properly damped.

3.4.3 Remarks

The following remarks are based on the simulation results presented in this section.

- i. The numerical derivative of the bus voltage phase angle of the WF can lead to non-physical oscillations and, possibly to numerical instabilities.
- ii. The average rotor speed provided by the COI filters local frequency variations. This fact may cause poorly-damped frequency oscillations, especially if coupled to devices with a slow response, such as TCLs.
- iii. Controllers using signals obtained with the FD are less prone to introduce numerically-driven undamped oscillations.

From the results above, it is clear that a proper modeling of the control signals can make a significant difference in the transient stability analysis of a power system with inclusion of frequency controllers other than primary frequency regulators of synchronous machines. The definition of a criterion to estimate the fidelity of such power system models is thus an interesting and urgent research topic.

3.5 Case Study: Frequency Estimators in Real Systems

In this section, two real-world systems are considered, namely, a 1,479-bus model of the all-island Irish transmission system; and a 21,177-bus model of the ENTSO-E transmission system, in Subsections 3.5.1 and 3.5.2, respectively. These systems are utilized to compare the performance and accuracy of the FD against the results obtained using the conventional WF. The topology and the steady-state data of both systems are based on the actual real-world systems provided by and the Irish TSO, EirGrid, and ENTSO-E,¹ respectively. However, all dynamic data are guessed based on the knowledge of the technology of power plants.

The dynamic model of the Irish system includes both conventional and wind power generation. This system allows understanding the accuracy of the FD considering a large penetration of induction machines and power electronic devices that are included in the models of wind turbines. The considered dynamic model of the ENTSO-E system includes only conventional power plants. Its large size allows comparing the computational burden of the conventional WF with the proposed FD, i.e., number of state and algebraic variables, size and sparsity of matrices and computing times.

3.5.1 Irish Transmission System

This subsection considers a dynamic model of the all-island Irish transmission system. The topology and the steady-state data of the system are based on the actual real-world system provided by the Irish TSO, EirGrid. However, all dynamic data are estimated based on the knowledge of the various power plant technologies used. The dynamic model of the Irish system includes both conventional and wind power generation. The system consists of 1,479 buses, 1,851 transmission lines and transformers, 245 loads, 22 conventional synchronous power plants modeled with 6th order synchronous machine models with AVRs and TGs, 6 Power System Stabilizers (PSSs) and 176 wind power plants, of which 142 are equipped with doubly-fed induction generators (DFIG) and 34

¹The data of the ENTSO-E system have been licensed to Prof. Milano by ENTSO-E. Data can be requested through an on-line application at www.entsoe.eu.

with constant-speed (CSWT). The schematic map of the all-island Irish transmission system is provided in Appendix C [42].

The large number of non-conventional generators based on induction machines and power electronics converters makes this system an excellent test-bed to check the accuracy of each of the frequency estimators presented. The stochastic processes applied to the wind follow a Weibull's distribution. A detailed description of the model of this process is provided in Appendix B.2. Two scenarios are considered: Subsection 3.5.1.1 shows the response of the Irish system facing a three-phase fault close to both a synchronous machine and a load, whereas Subsection 3.5.1.2 simulates a fault close to a wind power plant.

3.5.1.1 Fault close to a synchronous machine and a load

A three-phase fault occurs at $t = 1$ s, and is cleared by means of the disconnection of one transmission line after 180 ms. The location of the fault is close to a synchronous machine ($S_n = 181.7$ MVA), and a load (9.72 MW and 1.16 MVar), and their frequency is shown in Fig. 3.17.

Figure 3.17(a) depicts the rotor speed of the synchronous machine (Syn), as well as the estimated frequency of the bus where the machine is connected using both the FD and the WF. The time constant of the filter is $T_f = 0.01 \simeq 3/\Omega_n$ s, which is the default value in [35]. It can be seen how the FD tracks with high level of accuracy the rotor speed of the machine during and after the transient. On the other hand, the WF has a significant difference with respect to the rotor speed during the transient, and becomes accurate 4 s after the fault occurrence.

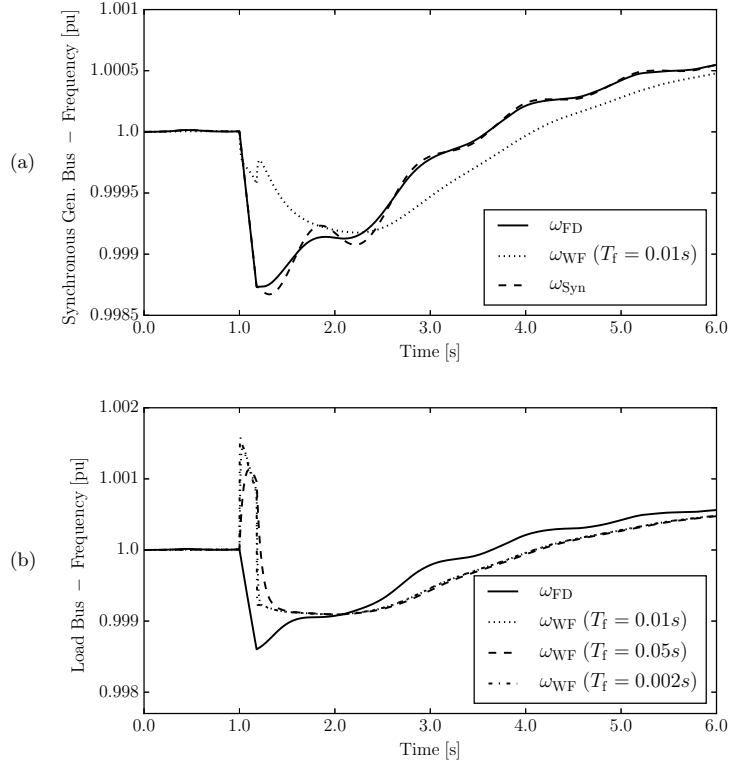


Figure 3.17: Frequency response of the Irish transmission system facing a three-phase fault close to a synchronous machine: (a) Synchronous machine bus; (b) Load bus.

The frequency of a load bus close to the fault is estimated using both the WF and the FD, and the comparison is shown in Fig. 3.17(b). To study how this frequency estimation is affected by the value of the filter time constant, three values are compared: the base value of $T_f = 0.01 \simeq 3/\Omega_n$ s used in the previous examples and simulations, as well as five times bigger and smaller time constants, i.e., $T_f = 0.05$ and $T_f = 0.002$ s, respectively. It can be observed that both estimators show a similar behavior about 2 s after the fault occurrence. However, the trajectories during the transient are significantly different. While the FD shows a behavior similar to that of the synchronous machine rotor speed shown in Fig. 3.17(a), the WF shows a peak in Fig. 3.17(b) right after the short-circuit and before the disconnection of the line that does not correspond to any physical behavior in the system.

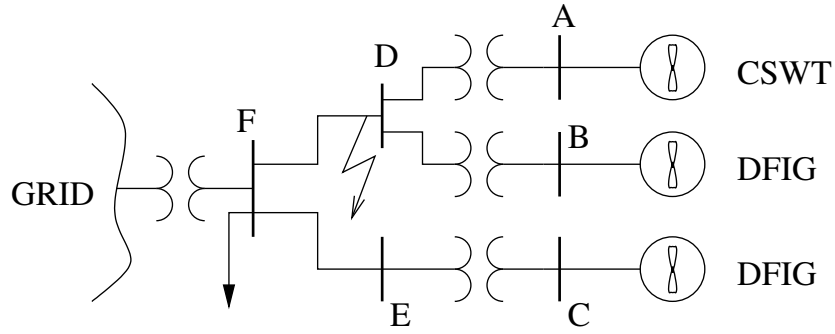


Figure 3.18: Scheme of a section of the Irish transmission system that includes a wind power plant.

3.5.1.2 Fault close to a wind power plant

In this subsection, a three-phase fault occurs close to a wind power plant, and is cleared after 240 ms (see Fig. 3.18). The wind plant is composed of 17 CSWTs (bus A), and 20 DFIGs split into 2 groups (buses B and C).

The frequency of bus A is estimated using both the WF and the FD, and the trajectories are shown in Fig. 3.19. The time constant of the filter is the default value of $T_f = 0.01$ s. As in the previous case, WF and FD trajectories are considerably different. While the FD shows a frequency response similar to the one obtained in Subsection 3.5.1.1, the filter adds a relatively high level of noise to the frequency measure. This is due to the fact that the WF estimates frequency variations based on a numerical derivative of the phase angle of the voltage at the point of connection of the wind turbine. Bus voltage angle varies in order to account for the small variations of the active power injected at the bus by the wind power plant. Such variations are a consequence of the stochastic behavior of the wind speed. However, the wind turbine does not impose the frequency at its node and, thus, the bus frequency is not related to wind turbine active power variations, as it happens for synchronous generators. Of course, the variations of the active power generation of the wind turbine do affect the dynamic behavior of synchronous machines which need to compensate the power unbalance. This is implicitly captured by the FD formula.

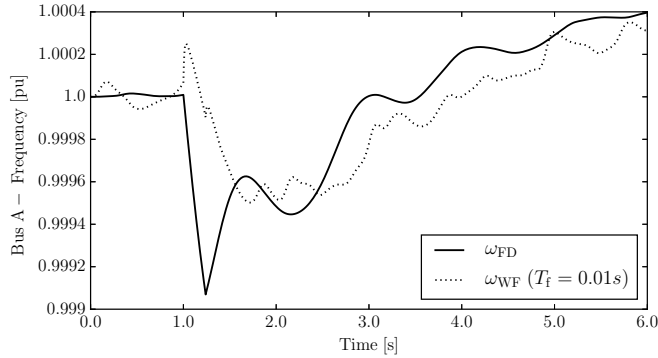


Figure 3.19: Frequency response of the Irish transmission system facing a three-phase fault close to a wind power plant.

3.5.2 ENTSO-E Transmission System

This subsection considers a dynamic model of the ENTSO-E transmission system. The model includes 21,177 buses (1,212 off-line); 30,968 transmission lines and transformers (2,352 off-line); 1,144 coupling devices, i.e., zero-impedance connections (420 off-line); 15,756 loads (364 off-line); and 4,828 power plants. Of these power plants, 1,160 power plants are off-line. The system also includes 364 PSSs.

This subsection provides a comparison of the computational burden of the FD and the WF, when these are connected to all buses. The case without any frequency estimator is also considered. Results are shown in Table 3.1.

Table 3.1: Computational burden of different bus frequency estimators.

	Base Case	Frequency Divider	Washout Filter
Number of state variables	49,396	49,396 (0.00%)	91,750 (+85.74%)
Number of algebraic variables	96,768	117,945 (+21.88%)	117,945 (+21.88%)
Size of DAE system	146,164	167,341 (+31.07%)	209,695 (+105.82%)
NNZ % of Jacobian Matrix	0.00256	0.00222 (-13.28%)	0.00153 (-40.23%)
Initialization of full DAE [s]	0.35087	0.40617 (+15.76%)	0.40063 (+14.18%)
Time Domain Analysis [s]	37.4006	41.2198 (+10.21%)	44.3770 (+18.65%)

The number of state and algebraic variables, and the size and sparsity of the state matrix in the three cases is first compared. Both the FD and the WF add to the system a number of algebraic variables equal to the number of buses of the system. Then, each WF defines two state variables per bus, whereas the FD does not include differential equations. This leads to an increase in the number of elements of the state matrix of

31.07% and 105.82% for the FD and the WF, respectively. The percentage of the non-zero elements with respect to the total number of elements is reduced by 13.28% by using the FD, while the WF decreases this number by 40.23%.

A power flow analysis followed by the initialization of dynamic devices is then carried out. The computational time of the initialization is also reported in Table 3.1. This consists mainly in the set-up of synchronous machines and primary regulators state and algebraic variables (second column), and the computation of the matrix \mathbf{D} (third column) or of the initial values of the variables of the WFs (fourth column), depending on the frequency estimator that is included in the model. It can be observed that both the FD and the WFs increase this value by 15.76% and 14.18%, respectively.

Finally, a time domain simulation (TDS) is performed for each scenario. The simulation lasts 5 s, and the contingency considered is a three-phase fault, cleared after 200 ms. The time step of the TDS is 0.02 s. The implicit trapezoidal method is used for the time integration, and each integration step is solved by using the dishonest Newton-Raphson method [78]. Observing Table 3.1, it can be observed that installing WFs at every bus increases the computational time of the TDS by 18.65%, while this time is only 10.21 % higher in the case of the proposed FD.

Finally, Table 3.2 shows the size and number of non-zero elements of the aforementioned matrices for the ENTSO-E system. It can be seen that, as opposed to matrices \mathbf{B}_{BB} , \mathbf{B}_{BG} and \mathbf{B}_{G0} , which are extremely sparse, matrix \mathbf{D} is almost dense and thus its computational burden is unacceptable for large systems. This fact justifies the implementation of equation (3.18) instead of (3.16).

Table 3.2: Size and number of non-zeros (NNZ) elements of matrices \mathbf{B}_{BB} , \mathbf{B}_{G0} , \mathbf{B}_{BG} and \mathbf{D} for the ENTSO-E system.

Matrix	Size	NNZ	NNZ %
\mathbf{B}_{BB}	$21,177 \times 21,177$	72,313	0.0161
\mathbf{B}_{BG}	$21,177 \times 4,832$	4,832	0.0047
\mathbf{B}_{G0}	$21,177 \times 21,177$	3,245	0.0007
$\mathbf{B}_{BB} + \mathbf{B}_{G0}$	$21,177 \times 21,177$	72,313	0.0161
\mathbf{D}	$21,177 \times 4,832$	86,169,456	84.2096

3.6 Concluding Remarks

This chapter describes different techniques to estimate the frequency for electromechanical models of power systems. Among the well-known center of inertia, and the commonly-used washout filter of bus voltage phase angles, this chapter also proposes a voltage divider-based formula. This *frequency divider* formula is a general expression to estimate frequency variations during the transient of electric power systems. The proposed expression is derived based on standard assumptions of power system models for TSA and can be readily implemented in power system software tools for TSA. The formula is aimed at improving the accuracy of bus frequency estimation in traditional electromechanical power system models.

Two real-world networks, namely a the all-island Irish and the European transmission systems, have been used to compare the features of the three frequency estimators. Simulation results show that the proposed formula is accurate, numerically robust and, if properly implemented, computationally efficient.

4 | Generalized Model of Energy Storage Systems

4.1 Motivation

Modeling ESSs is a complex and time-consuming task due to the number of different technologies that are currently available and that are expected to be developed in the future. While there are several studies aimed to define the economic viability and the effect on electricity markets of ESSs (see for example [15] and [11]), there is still no commonly-accepted simple yet accurate general model of ESSs for voltage and angle stability studies.

Several simplified ESS models have been proposed for these studies [93, 122, 110, 107, 48]. The main feature that the models proposed in the references above have in common is that the ESS dynamics are represented considering only active and reactive power controllers, as shown in Fig. 4.1 [93].

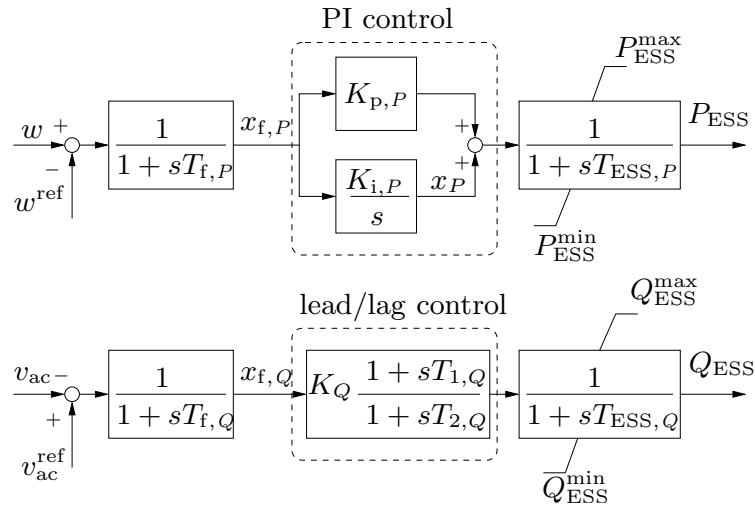


Figure 4.1: Scheme of a simplified ESS model.

The input signal w (see Fig. 2.1) is regulated through the active power while the voltage at the point of connection with the grid is regulated through the ESS reactive power. The physical behavior of the storage system is synthesized by the two lag blocks with time constants $T_{\text{ESS},P}$ and $T_{\text{ESS},Q}$. The main drawback of these “overly” simplified models is that the dynamics of the ESS itself are not preserved. Moreover, these models are also generally loss-less as dc and VSC circuitry is neglected.

The alternative to these simplified ESS models is to use the specific detailed models of each ESS technology described in Chapter 2. However, this can be a challenge if different technologies are going to be studied and/or compared, or if new control techniques are being developed, specially for complicated, highly nonlinear models (see for example the models of the BES and the CAES in Sections 2.2.1 and 2.2.2, respectively).

This chapter presents a generalized model of ESSs to simplify, without giving up accuracy, the simulation of different storage technologies [89]. The objective is to provide a balanced, fundamental-frequency model that can be defined through a reduced and fixed set of parameters and that can be readily implemented in power system simulators for voltage and angle stability analysis. The model proposed is based on the observation that most ESSs connected to transmission and distribution grids share a common structure, i.e., are coupled to the ac network through a VSC device, present a dc-link and then include another converter (either a dc/dc or a ac/dc device) to connect the main energy storage device to the dc link. Moreover, all storage systems necessarily imply potential and flow quantities (see Table 4.1), whose dynamics characterize the transient response of the ESS. This chapter proves that, to properly capture the dynamic response of the ESS, it is important to preserve such dynamics along with those of the VSC converter and its controllers. Controller hard limits, whose relevance has been discussed in [48] and [91], are also considered.

Table 4.1: Examples of energy storage technologies.

Types of Storable Energy	Potential Variables	Flow Variables	Technology
Electrochemical	Electrochemical Potential	Molar Flow Rate	BES
Fluid	Pressure	Mass Flow	CAES
Rotational	Angular Velocity	Torque	FES
Electrostatic	Electric Potential	Electric Current	SCES
Magnetic	Magneto Motive Force	Flux	SMES

In summary, the chapter provides the following contributions:

1. A simple yet accurate generalized storage device model that consists of a given set of parameters and linear DAEs. The structure and dynamic order of this set of DAEs is independent from the ESS technology.
2. A comprehensive validation of the dynamic response of the proposed ESS model versus detailed transient stability models representing specific technologies as well as simplified models that include only active and reactive power controllers.

The remainder of the chapter is organized as follows. Section 4.2 describes the hypotheses, the structure and the formulation of the proposed generalized model of ESSs, as well as how this model is able to describe the behavior of a variety of ESS technologies. Section 4.3 compares the dynamic response of the proposed model with detailed and simplified models of ESSs for TSA. All simulations are based on the WSCC 9-bus test system. Finally, section 4.4 draws conclusions.

4.2 Proposed Generalized Model of Energy Storage Devices

The Generalized ESS Model (GEM) proposed in this work is based on the linearization and dynamic reduction of the set of equations that describes the storage device. Let us assume that the dynamic behavior of the ESS can be described by the following nonlinear state-space representation:

$$\begin{aligned}\mathbf{T}\dot{\boldsymbol{\xi}}(t) &= \boldsymbol{\psi}(\boldsymbol{\xi}(t), \boldsymbol{\nu}(t)) \\ \boldsymbol{\varphi}(t) &= \boldsymbol{\eta}(\boldsymbol{\xi}(t), \boldsymbol{\nu}(t))\end{aligned}\tag{4.1}$$

where $\boldsymbol{\xi}(t)$ is the state vector ($\boldsymbol{\xi} \in \mathbb{R}^n$); $\boldsymbol{\nu}(t)$ is the input vector ($\boldsymbol{\nu} \in \mathbb{R}^m$); $\boldsymbol{\varphi}(t)$ is the output vector ($\boldsymbol{\varphi} \in \mathbb{R}^p$); $\boldsymbol{\psi} : \mathbb{R}^{n+m} \rightarrow \mathbb{R}^n$ are the differential equations; $\boldsymbol{\eta} : \mathbb{R}^{n+m} \rightarrow \mathbb{R}^p$ are the output equations; and \mathbf{T} is a time-invariant, not necessarily diagonal nor full rank time constant matrix of dimensions $n \times n$. The interested reader can find more information about the semi-implicit formulation used in this work in [79].

The first step towards the definition of the GEM is to linearize the system around the equilibrium point $(\boldsymbol{\xi}_0, \boldsymbol{\varphi}_0, \boldsymbol{\nu}_0)$. Thus, the expression for a linear time-invariant dynamical system is obtained:

$$\begin{aligned}\mathbf{T}\dot{\boldsymbol{\xi}}(t) &= \mathbf{A}\boldsymbol{\xi}(t) + \mathbf{B}\boldsymbol{\nu}(t) + \mathbf{K}_\xi \\ \boldsymbol{\varphi}(t) &= \mathbf{C}\boldsymbol{\xi}(t) + \mathbf{D}\boldsymbol{\nu}(t) + \mathbf{K}_\varphi\end{aligned}\quad (4.2)$$

where \mathbf{A} is the state matrix ($\dim[\mathbf{A}] = n \times n$); \mathbf{B} is the input matrix ($\dim[\mathbf{B}] = n \times m$); \mathbf{C} is the output matrix ($\dim[\mathbf{C}] = p \times n$); \mathbf{D} is the feedthrough matrix ($\dim[\mathbf{D}] = p \times m$); and $\mathbf{K}_\xi \in \mathbb{R}^n$ and $\mathbf{K}_\varphi \in \mathbb{R}^p$ account for the values of the variables at the equilibrium point. Equation (4.2) is written for $\boldsymbol{\xi}$, $\boldsymbol{\nu}$ and $\boldsymbol{\varphi}$, not the incremental values $\Delta\boldsymbol{\xi}$, $\Delta\boldsymbol{\nu}$, and $\Delta\boldsymbol{\varphi}$.

Then, the state vector $\boldsymbol{\xi}$ is split into two types of variables: the potential and flow variables related to the energy stored in the ESS, \boldsymbol{x} (see Table 4.1); and all other state variables, \boldsymbol{z} . Hence, $\boldsymbol{\xi} = [\boldsymbol{x}^T, \boldsymbol{z}^T]^T$. Since all ESSs are coupled to the ac network through a VSC device, the dc voltage and current of the VSC, v_{dc} and i_{dc} , are considered as an input and an output in (4.2), respectively. The input vector $\boldsymbol{\nu}$ is composed of the output signal of the storage control, u , and the dc voltage of the VSC, v_{dc} . Hence, $\boldsymbol{\nu} = [u, v_{dc}]^T$. Finally, the output vector $\boldsymbol{\varphi}$ is the dc current of the VSC, i_{dc} . Hence, $\boldsymbol{\varphi} = [i_{dc}]$. Applying the notation above, equation (4.2) is written as follows:

$$\begin{aligned}\mathbf{T}_x \dot{\boldsymbol{x}} &= \mathbf{A}_{xx}\boldsymbol{x} + \mathbf{A}_{xz}\boldsymbol{z} + \mathbf{B}_{xu}u + \mathbf{B}_{xv}v_{dc} + \mathbf{K}_x \\ \mathbf{T}_z \dot{\boldsymbol{z}} &= \mathbf{A}_{zx}\boldsymbol{x} + \mathbf{A}_{zz}\boldsymbol{z} + \mathbf{B}_{zu}u + \mathbf{B}_{zv}v_{dc} + \mathbf{K}_z \\ i_{dc} &= \mathbf{C}_x\boldsymbol{x} + \mathbf{C}_z\boldsymbol{z} + \mathbf{D}_u u + \mathbf{D}_v v_{dc} + \mathbf{K}_i\end{aligned}\quad (4.3)$$

where:

$$\begin{aligned}\begin{bmatrix} \mathbf{A}_{xx} & \mathbf{A}_{xz} \\ \mathbf{A}_{zx} & \mathbf{A}_{zz} \end{bmatrix} &= \mathbf{A} ; \quad \begin{bmatrix} \mathbf{B}_{xu} & \mathbf{B}_{xv} \\ \mathbf{B}_{zu} & \mathbf{B}_{zv} \end{bmatrix} = \mathbf{B} ; \quad \begin{bmatrix} \mathbf{T}_x & \mathbf{0} \\ \mathbf{0} & \mathbf{T}_z \end{bmatrix} = \mathbf{T} ; \\ [\mathbf{C}_x \ \mathbf{C}_z] &= \mathbf{C} ; \quad [\mathbf{D}_u \ \mathbf{D}_v] = \mathbf{D} ; \quad [\mathbf{K}_x \ \mathbf{K}_z]^T = \mathbf{K}_\xi ; \quad \mathbf{K}_i = \mathbf{K}_\varphi\end{aligned}$$

The dynamic order of (4.3) is reduced by assuming that the transient response of \mathbf{z} is adequately faster than that of \mathbf{x} or immaterial with respect to the overall dynamic behavior of the ESS. This assumption is based on the knowledge of detailed transient stability models and is duly verified through the simulations presented in Section 4.3. By neglecting the dynamics of \mathbf{z} (i.e., $\mathbf{T}_z \dot{\mathbf{z}} = \mathbf{0}$), from the second equation of (4.3), we obtain:

$$\mathbf{z} = -\mathbf{A}_{zz}^{-1} (\mathbf{A}_{zx}\mathbf{x} + \mathbf{B}_{zu}u + \mathbf{B}_{zv}v_{dc} + \mathbf{K}_z) \quad (4.4)$$

Then, substituting (4.4) into the first and third equations of (4.3), one has:

$$\begin{aligned} \mathbf{T}_x \dot{\mathbf{x}} &= (\mathbf{A}_{xx} - \mathbf{A}_{xz}\mathbf{A}_{zz}^{-1}\mathbf{A}_{zx}) \mathbf{x} + (\mathbf{B}_{xu} - \mathbf{A}_{xz}\mathbf{A}_{zz}^{-1}\mathbf{B}_{zu}) u \\ &\quad + (\mathbf{B}_{xv} - \mathbf{A}_{xz}\mathbf{A}_{zz}^{-1}\mathbf{B}_{zv}) v_{dc} + (\mathbf{K}_x - \mathbf{A}_{xz}\mathbf{A}_{zz}^{-1}\mathbf{K}_z) \\ i_{dc} &= (\mathbf{C}_x - \mathbf{C}_z\mathbf{A}_{zz}^{-1}\mathbf{A}_{zx}) \mathbf{x} + (\mathbf{D}_u - \mathbf{C}_z\mathbf{A}_{zz}^{-1}\mathbf{B}_{zu}) u \\ &\quad + (\mathbf{D}_v - \mathbf{C}_z\mathbf{A}_{zz}^{-1}\mathbf{B}_{zv}) v_{dc} + (\mathbf{K}_i - \mathbf{C}_z\mathbf{A}_{zz}^{-1}\mathbf{K}_z) \end{aligned} \quad (4.5)$$

Rewriting in compact form the matrices in (4.5), the proposed GEM can be written as follows:

$$\begin{aligned} \tilde{\mathbf{T}} \dot{\mathbf{x}} &= \tilde{\mathbf{A}} \mathbf{x} + \tilde{\mathbf{B}}_u u + \tilde{\mathbf{B}}_v v_{dc} + \tilde{\mathbf{K}}_x \\ i_{dc} &= \tilde{\mathbf{C}} \mathbf{x} + \tilde{\mathbf{D}}_u u + \tilde{\mathbf{D}}_v v_{dc} + \tilde{\mathbf{K}}_i \end{aligned} \quad (4.6)$$

where, for example, $\tilde{\mathbf{A}} = \mathbf{A}_{xx} - \mathbf{A}_{xz}\mathbf{A}_{zz}^{-1}\mathbf{A}_{zx}$.

It is important to take into account the state of charge of the storage device (in particular, to impose energy limits to the controller shown in Fig. 2.2). With this aim, the actual stored energy is given by:

$$E = \sum_{i=1}^n \rho_i \left(x_i^{\beta_i} - \chi_i^{\beta_i} \right) \quad (4.7)$$

where ρ_i , β_i and χ_i are the proportional coefficient, exponential coefficient and reference potential value of each variable x_i , respectively.

In summary, the proposed GEM is composed of the block diagram of the VSC represented in Fig. 2.4; the controllers depicted in Figs. 2.2 and 2.6; and (4.6), (4.7).

For the sake of clarity and example, the GEM for the ESSs technologies described in Subsections 2.2.1-2.2.5 are deduced below.

4.2.1 Generalized model of different storage technologies

SCES

The structure of the set of equations of the detailed transient stability model of the SCES in Section 2.2.4 and the proposed GEM is fairly similar, and thus, the general expression of the SCES is firstly derived. Applying the notation of the GEM (4.6-4.7) to (2.27-2.28), SCES variables and parameters are:

$$\begin{aligned}
 \mathbf{x} &= [v_{sc} \ i_{sc}]^T; \quad \mathbf{z} = \emptyset; \quad u = S_{sc}; \quad \tilde{\mathbf{T}} = \begin{bmatrix} C_{sc} & 0 \\ 0 & L_{sc} \end{bmatrix}; \quad \tilde{\mathbf{A}} = \begin{bmatrix} -G_{sc} & -1 \\ 1 & -R_{sc} \end{bmatrix}; \\
 \tilde{\mathbf{B}}_u &= [0 \ v_{dc,0}]^T; \quad \tilde{\mathbf{B}}_v = [0 \ S_{sc,0}]^T; \quad \tilde{\mathbf{K}}_x = \begin{bmatrix} G_{sc}v_{sc,0} + i_{sc,0} \\ -v_{sc,0} + R_{sc}i_{sc,0} + 2v_{dc,0}S_{sc,0} \end{bmatrix}; \quad (4.8) \\
 \tilde{\mathbf{C}} &= [0 \ S_{sc,0}]; \quad \tilde{\mathbf{D}}_u = [i_{sc,0}]; \quad \tilde{\mathbf{D}}_v = [0]; \quad \tilde{\mathbf{K}}_i = [i_{dc,0} - 2S_{sc,0}i_{sc,0}]; \\
 \boldsymbol{\rho} &= \left[\frac{1}{2}C_{sc} \ \frac{1}{2}L_{sc} \right]; \quad \boldsymbol{\beta} = [2 \ 2]; \quad \boldsymbol{\chi} = [0 \ 0]
 \end{aligned}$$

where $S_{sc,0}$, $v_{sc,0}$, $v_{dc,0}$, $i_{sc,0}$ and $i_{dc,0}$ are the values of S_{sc} , v_{sc} , v_{dc} , i_{sc} and i_{dc} at the equilibrium point, respectively.

Similar procedure is applied to the remaining energy storage technologies, and results are shown below in Tables 4.2-4.5.

BES

The nonlinearity of v_p in (2.9) implies that depending on the state of the battery (charge or discharge), two different sets of equations can be obtained by applying the proposed GEM. Therefore, the GEM has to be able to switch from one set to another depending on the BES operation.

Table 4.2: GEM variables and parameters of BES technology.

\mathbf{x}	\mathbf{z}	u	$\boldsymbol{\rho}$	$\boldsymbol{\beta}$	$\boldsymbol{\chi}$
$[Q_{e,B} \ v_B]^T$	$[i_B \ i_{m,B} \ v_{p,B}]^T$	S_B	$\left[-\frac{1}{Q_{n,B}} \ 0 \right]$	$[1 \ 1]$	$[Q_{n,B} \ 0]$

CAES

The air valve is not modeled in this work. Therefore, the output of the storage control, and thus the input to the GEM u is the air flow, $Q_{\mu C}$.

Table 4.3: GEM variables and parameters of CAES technology.

\mathbf{x}	\mathbf{z}				
$[\Pi_2 \ \Omega_{r,\mu C}]^T$	$[P_{ef,\mu C} \ P_{m,\mu C} \ P_{el,\mu C} \ T_{m,\mu C} \ T_{el,\mu C} \ \sigma_{sr,\mu C} \ m_{dc,\mu C} \ m_{qc,\mu C} \ m_{dt,\mu C} \ m_{qt,\mu C} \ \dots]^T$				
u	i_{dc}	$\boldsymbol{\rho}$	$\boldsymbol{\beta}$	$\boldsymbol{\chi}$	
$Q_{\mu C}$	$i_{dc,c} + i_{dc,t}$	$\left[\frac{\gamma}{\gamma-1} \Pi_1^{\gamma-1} V_{\mu C} \ H_{\mu C} \right]$	$\left[\frac{\gamma-1}{\gamma} \ 2 \right]$	$[\Pi_1 \ 0]$	

The dots in the vector \mathbf{z} stand for electrical machine and ac/dc converter variables. \mathbf{z} contains 25 state and algebraic variables. By using the proposed model, the nonlinear set of DAEs which models the CAES ((2.13)-(2.22), and equations of the ac/dc converters) is reduced to a set of three linear DAEs (4.6).

FES

Table 4.4: GEM variables and parameters of FES technology.

\mathbf{x}	\mathbf{z}	u	$\boldsymbol{\rho}$	$\boldsymbol{\beta}$	$\boldsymbol{\chi}$
$[\omega_{r,F} \ T_{el,F}]^T$	$[T_{m,F} \ v_{ds,F} \ v_{qs,F} \ \dots]^T$	$\omega_{s,F}$	$[H_F \ 0]$	$[2 \ 1]$	$[0 \ 0]$

The dots in the vector \mathbf{z} stand for the stator and rotor currents and flux linkages of the induction machine, and the ac/dc converter variables. \mathbf{z} contains 13 state and algebraic variables.

SMES

Table 4.5: GEM variables and parameters of SMES technology.

\mathbf{x}	\mathbf{z}	u	$\boldsymbol{\rho}$	$\boldsymbol{\beta}$	$\boldsymbol{\chi}$
$[i_{SM} \ v_{SM}]^T$	\emptyset	S_{SM}	$\left[\frac{1}{2} L_{SM} \ 0 \right]$	$[2 \ 1]$	$[0 \ 0]$

4.3 Case Study

This section validates the proposed GEM through time domain simulations. Three energy storage technologies are considered, namely, SMES, CAES and BES. With this aim, the WSCC 9-bus test system (see Fig. 4.2) is used for all simulations. This benchmark network consists of three synchronous machines, three transformers, six transmission lines and three loads. Primary frequency and voltage regulators (TGs and AVRs) are also included. All dynamic data of the WSCC 9-bus system as well as a detailed discussion of its transient behavior were originally provided in [8], and are publicly available (see for example [60]).

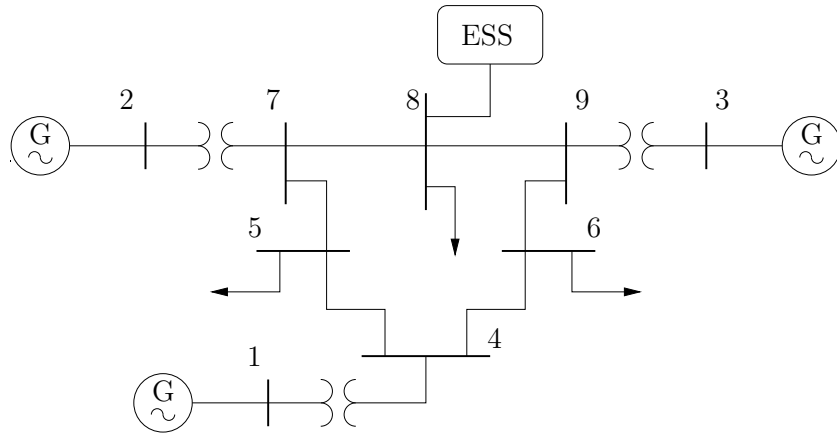


Figure 4.2: WSCC 9-bus test system with an ESS device connected to bus 8.

An ESS is connected to bus 8. The capacities of the ESSs used in this case study have been designed according to the power installed in the system. This leads to assume large ESSs. Different scenarios have been performed in this chapter: Subsection 4.3.1 shows the response of a SMES connected to the WSCC system following a three-phase fault (Subsection 4.3.1.1), and stochastic variations of the loads (Subsection 4.3.1.2). A similar analysis is carried out in Subsection 4.3.2 for a CAES device. In this case, the contingency is a loss of load (Subsection 4.3.2.1), and stochastic processes are applied to all load power consumptions (Subsection 4.3.2.2). Finally, a BES and a loss of load are considered in Subsection 4.3.3. Note that results shown in this section are not hand-picked but, rather, randomly selected among several hundreds of simulations that have been carried out to check the validity and accuracy of the proposed GEM.

4.3.1 SMES

In this subsection, the storage device connected to bus 8 is a 15 MW, 60 MJ SMES, (see Subsection 2.2.5). Two scenarios have been considered: Subsection 4.3.1.1 compares the dynamic response of the models of the SMES when the system faces a three-phase fault, whereas Subsection 4.3.1.2 considers stochastic variations of the loads and different initial states of charge of the SMES.

4.3.1.1 Contingency

A three-phase fault occurs at bus 7 at $t = 1$ s and is cleared after 70 ms through the disconnection of the line which connects buses 7 and 5. In this case, the frequency of the COI of the system, ω_{COI} , is regulated and its trajectory is shown in Figs. 4.3(a) and 4.3(b) using the detailed and the proposed models of the SMES. Figures 4.3(a) and 4.3(b) also show ω_{COI} when the SMES is modeled using the simplified model depicted in Fig. 4.1. In practical applications, the ω_{COI} signal can be obtained in real-time from the System Operator (e.g., EirGrid in Ireland). Note that the time-delays that may affect this signal are neglected in this study since the variations of ω_{COI} are relatively slow.

It can be observed that without ESS the frequency variation after the fault is around 1%, and the steady-state is reached after about 40 s. The inclusion of the SMES in the system allows reducing the overshoot by 60%. Moreover, the settling time is about 15 s.

Figure 4.3(c) compares the active power output of the SMES when the detailed and the proposed models are used. The SMES uses the load notation, therefore positive values of the power indicate that the SMES is storing energy, and vice versa.

Finally, Fig. 4.3(d) depicts the variation of the energy stored in the SMES. The base of the energy is 100 MJ, therefore the SMES increases its stored energy a maximum of about 57 MJ during and after the fault. The steady-state value of the energy after the occurrence of the disturbance is about 20 MJ over the initial conditions. As it can be observed from Fig. 4.3, the performance of the system is basically the same when using the detailed and the proposed models of the SMES.

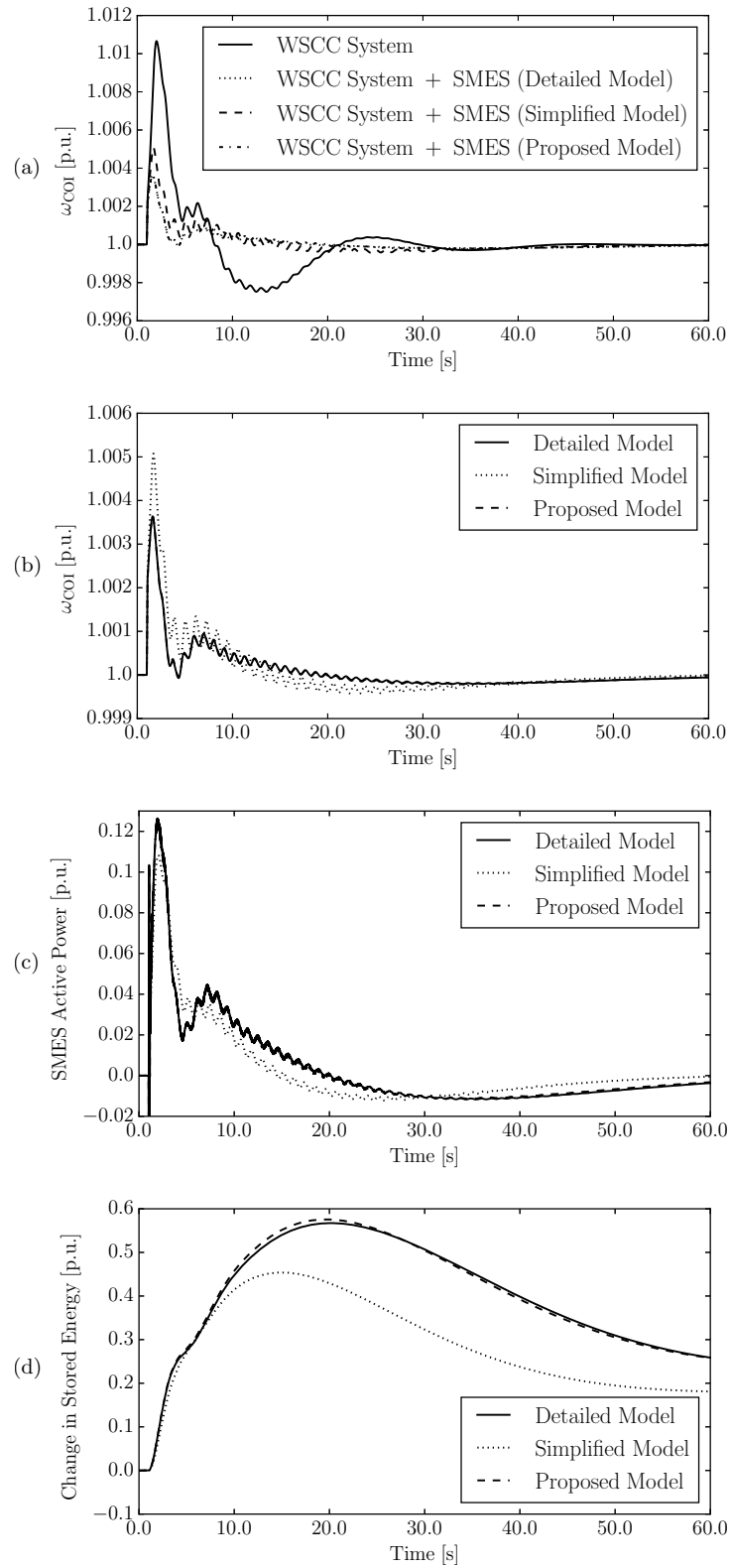


Figure 4.3: Response of the WSCC system with a SMES following a three-phase fault at bus 7. (a), (b) Frequency of the COI; (c) Active power of the SMES; (d) Change in the stored energy of the SMES.

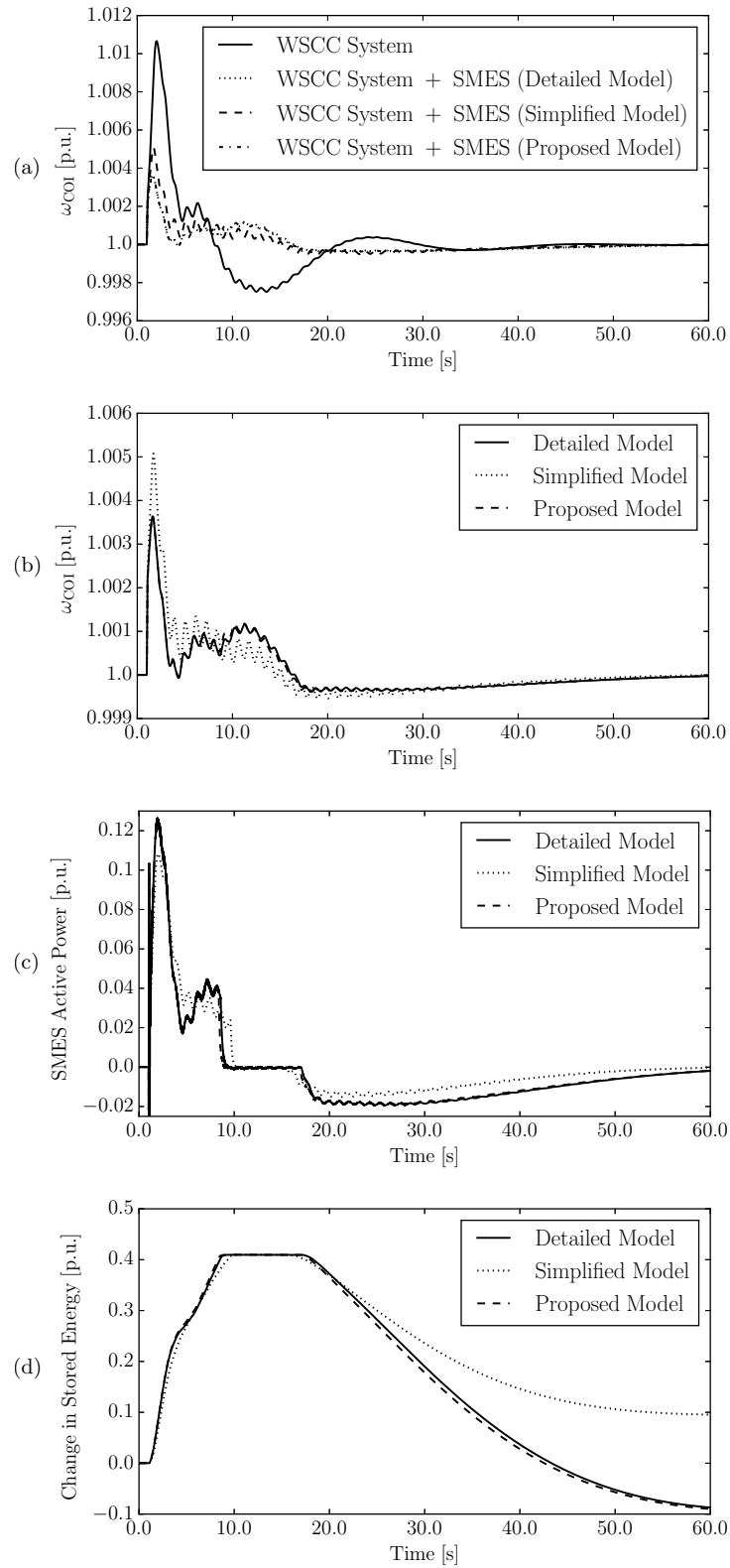


Figure 4.4: Response of the WSCC system following a three-phase fault at bus 7 when the SMES reaches its maximum storable energy. (a), (b) Frequency of the COI; (c) Active power of the SMES; (d) Change in the stored energy of the SMES.

Figure 4.4 shows the performance of the system when the SMES reaches its maximum storable energy. In this simulation, it has been considered a maximum variation in the energy of 40 MJ over the initial condition. It can be observed that the effect of this sort of nonlinearity is precisely captured by the proposed model, and the differences in the performance between the detailed and the proposed models are very small.

Figures 4.3 and 4.4 also show the transient response of the SMES when the commonly-used simplified model of ESSs is applied. Gains and time constants of the different controllers of Fig. 4.1 have the same value for all ESS models. The trajectories obtained by imposing the simplified model consistently deviate from the behavior of the detailed one, particularly after the transient (i.e., for $t \gtrsim 8$ s in Fig. 4.3) and after reaching the maximum variation of stored energy (i.e., for $t \gtrsim 18$ s in Fig. 4.4). Note that, for a fair comparison, energy limits are also included in the simplified model in Fig. 4.4. The proposed GEM is able to accurately track the behavior of the detailed one in both, fast (transient) and slow (post-contingency) dynamics. On the other hand, the simplified model is accurate only in the first few seconds after the disturbance. The poor performance of the simplified model is an expected consequence of the overly reduced order of its dynamic equations. From the simulation results presented in this section, it can be thus concluded that VSC dynamics and couplings with the storage device must be taken into account along with those of the storage device itself. This goal is successfully achieved by the proposed GEM.

4.3.1.2 Stochastic Load Variations

In this scenario, all loads are modeled considering stochastic variations of the power consumptions. The Ornstein-Uhlenbeck's process is used to model such variations (see Appendix B.1). The step size of the Wiener's process is $h = 0.01$ s, and the time step of the time integration Δt is set to 0.1 s. Initial values of the load and generation are set using a uniform distribution with 5% of variation with respect to the base-case.

Figure 4.5 shows the frequency of the COI and the state of charge of the SMES for three different load profiles and for an initial State of Charge (SOC) of 20%, 50%, and 80% in Figs. 4.5(a), 4.5(b), and 4.5(c), respectively. These percentages are expressed in terms of the allowed energy variability of the storage device. For each simulation, SMES models are simulated considering same load variation profiles, and energy limits are also included.

The following remarks are relevant:

- i. The proposed GEM tracks the behavior of the detailed model better than the commonly-used simplified model of the SMES, for any initial SOC.
- ii. The proposed model is more accurate the closer the SOC is to the point at which the matrices in (4.6)-(4.7) are computed.
- iii. Energy saturations of the storage device cause the greatest differences between the models, for any initial SOC. The proposed model can capture these saturations with better accuracy than the simplified one.
- iv. Based on the observation of hundreds of simulations considering large disturbances, different load profiles, and different linearization points, the best average accuracy of the proposed GEM is obtained if the matrices of (4.6)-(4.7) are computed for a 50% SOC.

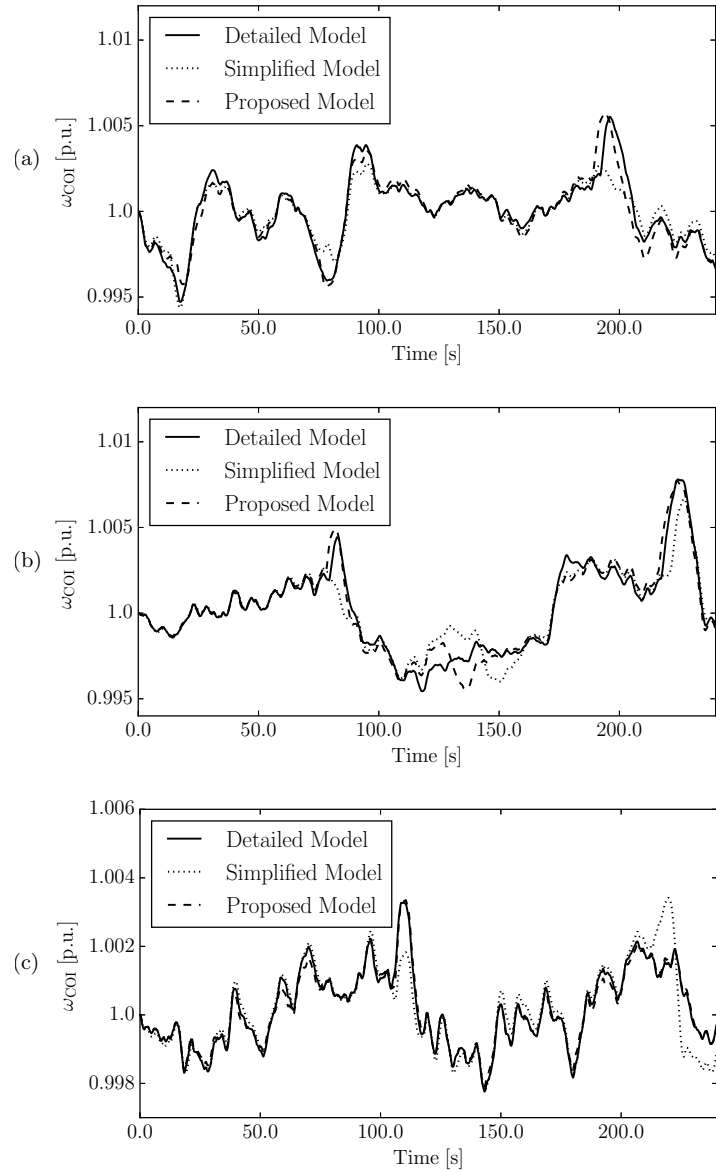


Figure 4.5: Response of the WSCC system with a SMES considering stochastic variations of the loads. (a) The initial SOC of the SMES is 20%; (b) The initial SOC of the SMES is 50%; (c) The initial SOC of the SMES is 80%.

4.3.2 CAES

In this case study, a 15 MW, 30 bar CAES is considered, (see Subsection 2.2.2). The CAES regulates the active power flowing through the transformer connecting buses 2 and 7. As in previous subsection, the CAES uses the load notation, and two scenarios are performed: Subsection 4.3.2.1 considers a loss of load as contingency, while Subsection 4.3.2.2 includes stochastic variations in all loads. Note that the maximum size of currently installed above-ground CAESs is up to 10 MW [86].

4.3.2.1 Contingency

The contingency is a loss of load of 15 MW occurring at bus 5 at $t = 10$ s. Finally, the load is reconnected at $t = 80$ s. Figures 4.6(a) and 4.6(b) illustrate the active power flowing through the transformer connecting buses 2 and 7 and the active power of the CAES, respectively. It can be seen that the response of the CAES simulated using the proposed model is accurate despite the complexity of the detailed CAES model shown in Subsection 2.2.2.

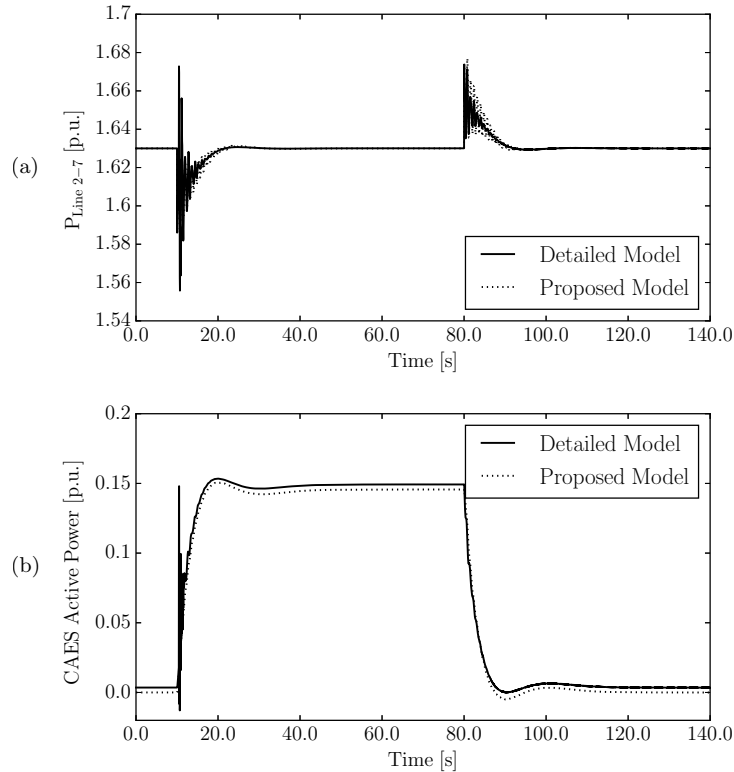


Figure 4.6: Response of the WSCC system with a CAES following a loss of load. (a) Power flowing through the transformer connecting buses 2 and 7; (b) Active power of the CAES.

4.3.2.2 Stochastic Load Variations

In this scenario, all loads are again modeled using the Ornstein-Uhlenbeck's process. Figure 4.7(a) depicts the active power of the CAES for each model of this device, for an initial SOC3 of 50%. All control parameters are the same for all models. The time constants of the simplified model of the CAES have been tuned after several trial and error attempts, in order to obtain the behavior as close as possible to the detailed model. Figure 4.7(a) shows that the response of the commonly-used simplified model differs considerably from the one of the detailed model. On the other hand, the proposed GEM appears to be very accurate.

In order to obtain a more accurate response of the storage device using the simplified model, it is required to properly tune the control gains $K_{p,P}$ and $K_{i,P}$ of the controller depicted in Fig. 4.1. Figure 4.7(b) depicts the response of the CAES considering the same load profiles as in Fig. 4.7(a), and when the gains $K_{p,P}$ and $K_{i,P}$ are three times smaller than the gains $K_{p,u}$ and $K_{i,u}$ of the storage controller of Fig. 2.2, respectively.

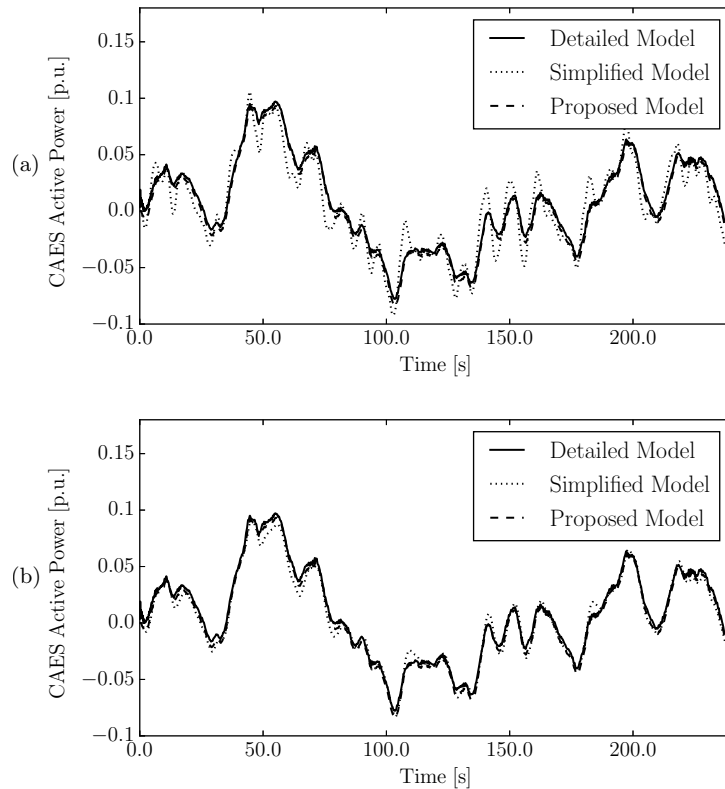


Figure 4.7: Response of the WSCC system with a CAES considering stochastic perturbations in the loads. (a) Same control parameters for all models; (b) Control parameters of the simplified CAES model are three times smaller than those of the detailed and the proposed ones.

Some remarks can be deduced:

- i. The accuracy of the proposed GEM does not appear to be affected by the complexity and the size of order reduction of the original detailed model. Note that the order reduction achieved in the case of the CAES is from 29 variables in the detailed model to only 5 in the proposed one.
- ii. The accuracy of the commonly-used simplified model cannot be guaranteed even if a lengthy and careful tuning of its control parameters is carried out.
- iii. Because of the required tuning, the design of control strategies cannot be based on the simplified model. On the other hand, exactly same control parameters can be used for both the generalized and detailed ESS models.

4.3.3 BES

In this example, a 40 MW BES is installed at bus 8. The data of the BES is taken from [75], that describes a 55 MW, 76.7 GJ BES used for frequency control. The contingency is a loss of a 40 MW load at bus 5. The load is disconnected at $t = 10$ s, and is reconnected at $t = 100$ s. In this case study, the BES regulates the frequency of the COI.

Figures 4.8(a) and 4.8(b) show the frequency of the COI and the power output of the BES, respectively. The initial SOC_B of the battery is set to 85% to force operating close to the nonlinear voltage-current characteristic of the battery [115, 105]. As stated in Subsection 4.2.1, two sets of matrices for the general model of the BES have to be considered because of the discontinuity in the polarization voltage, $v_{p,B}$, depending on whether the battery is charging (time from $t = 10$ s to $t = 100$ s) or discharging (time from $t = 100$ s). It can be seen from Fig. 4.8 that the GEM is able to track, with a good level of accuracy, the behavior of the detailed model of the BES for both operating conditions, despite the nonlinearity of the device at such a high initial SOC_B , and the switching between the two operating modes.

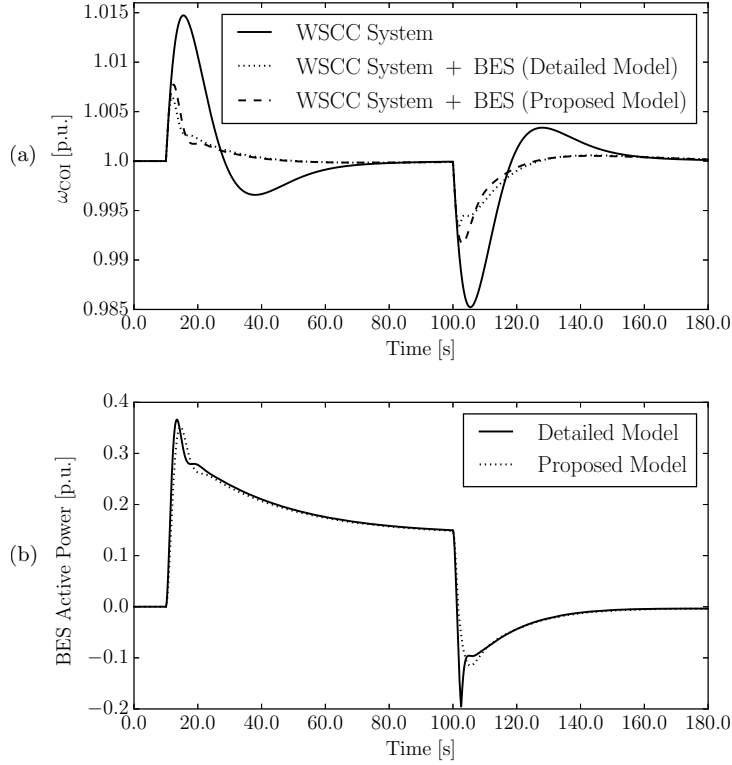


Figure 4.8: Response of the WSCC system with a BES following a loss of load. (a) Frequency of the COI; (b) Active power of the BES.

4.4 Concluding Remarks

The following remarks on the proposed GEM are relevant.

1. *The proposed GEM provides a good compromise between simplicity and accuracy.* In fact, the proposed model has a reduced and constant dynamic order but, nevertheless it can reproduce faithfully the behavior of ESSs whose detailed transient stability models are considerably more complex (e.g., CAES). On the contrary, the case study shows that simpler models of ESSs might not be precise, particularly if energy limits are reached.
2. *Linearization of a subset of ESS equations does not affect accuracy.* The rationale behind this observation is that most ESS variables involved in nonlinear equations are bounded and, hence, the ESS operating point does not vary consistently even after a large perturbation. Moreover, the smaller the variations of the state of charge with respect to the point at which the matrices of (4.6) are calculated, the higher the accuracy of the proposed model. This is an expected property of linearized models.

3. *Detailed ESS models are needed to define the parameters of the proposed model.*
These data have to be provided by ESS manufactures, in the same way makers provide d - and q -axis reactances and time constants of the synchronous machine Park model. Hence, the proposed GEM can be an opportunity to define an ESS standard for TSA.
4. *Control strategies designed for the proposed GEM can be directly applied to the detailed ESS models.* The linear structure of the equations of the proposed model simplifies the design of more advanced and robust control strategies for ESSs that could be applied subsequently to the detailed models of these devices.

5 | Formulation, Design and Comparison of Control Strategies for Energy Storage Systems

5.1 Motivation

The best known and most commonly used ESS control technique is the PI-based controller [84, 69]. However, other more sophisticated and robust controllers have been proposed in the literature. These can be deterministic and, typically, model-dependent, e.g., H-infinity (H_∞) control [107, 130], Sliding Mode (SM) control [61, 62, 46], Model Predictive Control (MPC) [87, 114], or based on heuristics, such as Fuzzy Logic Control (FLC) [128]. These references show the advantages of robust techniques with respect to the PI controller. However, the focus is only on a specific energy storage technology and a given system operating condition. Moreover, the references above do not consider real-world applications. The chapter aims at classifying, through a comprehensive stochastic approach, the dynamic behavior of each control technique considering different ESS technologies, contingencies and system scenarios [92].

One of the main difficulties involved in achieving the goal of the chapter is the wide variety of available energy storage technologies, which highly complicates the implementation and design of the controllers, in particular, for techniques that are strongly model-dependent, e.g., H_∞ and SM. To solve this issue, without compromising the fidelity of the simulations, the generalized ESS model (GEM) proposed in Chapter 4 is used in this chapter. It is worth remarking the interesting property of the GEM to retain the physical meaning of the main energy quantities, i.e., potential and flow variables. This chapter shows that, thanks to this property, the GEM proves to be particularly suited to being coupled with robust controllers such as the H_∞ and SM.

The chapter recalls the main features of three control techniques, namely, PI, H_∞ and SM, and describes the formulation of such techniques above based on the GEM. Then, an exhaustive comparison of the robustness of the dynamic response of the ESS

controllers based on PI, H_∞ and SM techniques is presented. With this aim, uncertainties related to both generation and demand, different loading levels and contingencies, i.e., faults and line and generator outages, are considered. Both ESS active power and frequency regulations are studied considering all the above. Preliminary results on the performance of the GEM coupled with different control strategies are presented based on the IEEE 14-bus test system.

Finally, an exhaustive and comprehensive comparison of the three control techniques based on a Monte Carlo method is applied to a 1,479-bus model of the Irish transmission grid with an existing Hybrid ESS (HESS), that is composed of a FES and a BES systems. The grid model is formulated as a set of Stochastic Differential Algebraic Equations (SDAEs) as discussed in [82].

The remainder of this chapter is organized as follows. Section 5.2 describes the detailed formulation of PI, H_∞ and SM controllers, and how to set them up with the GEM. Preliminary results of the comparison of PI, H_∞ and SM based on the IEEE 14-bus system with one ESS are presented in Section 5.3, while Section 5.4 discusses the case study based on the all-island Irish transmission system. Finally, conclusions are drawn in Section 5.5.

5.2 Control Strategies for ESSs

This section describes the main features and the formulation of three ESS control techniques, namely, the PI, H_∞ and SM, for the GEM presented in Chapter 4. Note that, if necessary, the designed controller can be applied to the original detailed ESS model without modification, which is a relevant advantage of the GEM formulation.

5.2.1 PI Control

For the sake of clarity, Fig. 5.1 depicts the typical ESS PI controller scheme presented in Subsection 2.1.1.

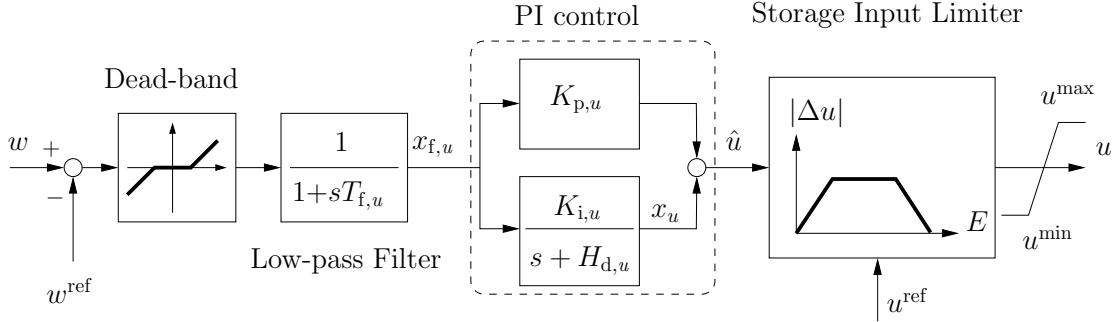


Figure 5.1: PI-based control for ESSs.

The PI regulator is composed of a proportional gain, $K_{p,u}$, and an integrator with gain $K_{i,u}$ and integral deviation coefficient $H_{d,u}$. These parameters are commonly tuned by trial-and-error or pole-placement techniques. The simplicity of the implementation and design, as well as the mass utilization of this controller in industrial applications are its main strengths. Note also that the structure of the PI does not depend on the energy storage technology considered. However, it has been shown that system uncertainties and topological changes can significantly deteriorate the behavior of this controller, and thus of the entire system [46]. This justifies the need for the development of more sophisticated and robust controllers, such as the ones that are described in the remainder of this section.

5.2.2 H_∞ Control

To cope with system and model uncertainties, alternatives to the PI regulator to improve the robustness of the control have been proposed in the literature. One of the most recognized and widely-used techniques is the H_∞ control, which formulates and solves the control problem as an optimization problem. The main objective of any optimal control approach consists of synthesizing a controller such that the closed-loop system is stable, and the performance output is minimized, given a class of disturbance inputs. Since the minimization of the energy gain of the closed-loop system can be too complicated to achieve in practice, the H_∞ approximates the solution of the problem above by minimizing the H_∞ norm of the closed-loop transfer function of the system shown in

Fig. 5.2 [20]. Applications of H_∞ control include a wide variety of areas. Examples of these areas are fluid dynamics [12], robotics [72], and ESSs in power systems [107, 130].

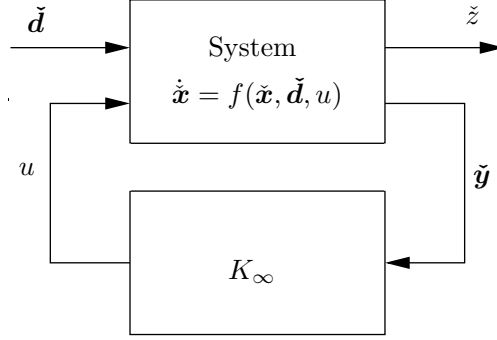


Figure 5.2: H_∞ controller.

The synthesis of a H_∞ controller is challenging even considering only a linear time-invariant system, as input and output quantities have to be chosen with care. With this aim, the relevance of the fixed and linear structure of the GEM outlined in the previous chapter becomes apparent. In fact, since the vector \boldsymbol{x} always includes potential and flow quantities, which can be used to determine the overall energy of the ESS, it is relatively simple to set up a linear controller K_∞ . Using similar notation to that in (4.6), the equations of the upper block in Fig. 5.2 are:

$$\begin{aligned}\check{\mathbf{T}}_x \dot{\check{\boldsymbol{x}}} &= \check{\mathbf{A}}\check{\boldsymbol{x}} + \check{\mathbf{B}}_1\check{\boldsymbol{d}} + \check{\mathbf{B}}_2u \\ \check{z} &= \check{\mathbf{C}}_1\check{\boldsymbol{x}} + \check{\mathbf{D}}_{11}\check{\boldsymbol{d}} + \check{\mathbf{D}}_{12}u \\ \check{\boldsymbol{y}} &= \check{\mathbf{C}}_2\check{\boldsymbol{x}} + \check{\mathbf{D}}_{21}\check{\boldsymbol{d}} + \check{\mathbf{D}}_{22}u\end{aligned}\tag{5.1}$$

where:

- $\check{\boldsymbol{x}} = [x_1 \ x_2 \ x_u]^\text{T}$, where x_1 and x_2 are the state variables of the system in (4.6); and x_u is the output of the integrator in Fig. 5.1;
- $\check{\mathbf{T}}_x = \begin{bmatrix} \mathbf{T}_x & \mathbf{0} \\ \mathbf{0} & 1 \end{bmatrix}$;
- $\check{\boldsymbol{d}} = [x_f \ v_{\text{dc}}]^\text{T}$ are the external perturbations;
- $\check{z} = x_u - K_u u$ is the regulated output signal. K_u is a positive weight coefficient to couple the output of the PI controller and the converter of the storage device.
- $\check{\boldsymbol{y}} = [\hat{u} \ v_{\text{dc}}]^\text{T}$ are the measurement outputs of the system.

Note that the inclusion of the output of the integrator, x_u , in the state vector of (5.1) allows implementing a droop frequency control through the ESS (if $H_{d,u} \neq 0$ in the control scheme of Fig. 5.1).

The synthesis of a H_∞ controller requires that a set of well-posedness constraints are satisfied, as follows:

- i. $(\check{\mathbf{A}}, \check{\mathbf{B}}_2)$ is stabilizable;
- ii. $(\check{\mathbf{C}}_2, \check{\mathbf{A}})$ is detectable;
- iii. $\check{\mathbf{D}}_{11} = \mathbf{0}$ and $\check{\mathbf{D}}_{22} = \mathbf{0}$;
- iv. $\text{rank}[\check{\mathbf{D}}_{12}] = \dim u = 1$, i.e., $\check{\mathbf{D}}_{12} \neq 0$ (full control penalty);
- v. $\text{rank}[\check{\mathbf{D}}_{21}] = \dim \check{\mathbf{y}} = 2$, i.e., $\check{\mathbf{D}}_{21}$ must be right invertible (full measurement noise);
- vi. $\text{rank} \begin{bmatrix} j\omega \mathbf{I}_3 - \check{\mathbf{A}} & \check{\mathbf{B}}_2 \\ \check{\mathbf{C}}_1 & \check{\mathbf{D}}_{12} \end{bmatrix} = \dim \check{\mathbf{x}} + \dim u = 4$,
for all real ω ;
- vii. $\text{rank} \begin{bmatrix} j\omega \mathbf{I}_3 - \check{\mathbf{A}} & \check{\mathbf{B}}_1 \\ \check{\mathbf{C}}_2 & \check{\mathbf{D}}_{21} \end{bmatrix} = \dim \check{\mathbf{x}} + \dim \check{\mathbf{y}} = 5$,
for all real ω .

Conditions iv to vii impose that the problem is not singular. If (5.1) satisfies all conditions above, then a suboptimal solution for K_∞ can be found by solving two algebraic Riccati equations, which have same order as the original system to be controlled.¹ The structure of the resulting controller indicated as K_∞ in Fig. 5.2 is as follows:

$$\begin{aligned} \dot{\mathbf{x}}_\infty &= \mathbf{A}_\infty \mathbf{x}_\infty + \mathbf{B}_\infty \check{\mathbf{y}} \\ u &= \mathbf{C}_\infty \mathbf{x}_\infty + \mathbf{D}_\infty \check{\mathbf{y}} \end{aligned} \tag{5.2}$$

It is important to note that the H_∞ problem is formulated for an augmented model of the GEM, i.e., (5.1) and that it does not involve nor require the knowledge of the dynamics of the whole transmission system. This fact makes feasible the implementation of (5.1)-(5.2) in real-world applications.

¹In the case study, the Fortran library SLICOT is used to solve Riccati equations [17].

5.2.3 Sliding Mode Control

The basic principle of the SM control is to take advantage of a switching control logic to force the trajectories of a dynamic variable-structure system to follow a given path, called *sliding surface*. If the sliding surface, say \mathcal{S} , satisfies usual requirements of existence and reachability, which in turn are needed to satisfy Lyapunov asymptotic stability conditions, the motion associated with the SM control is robust against disturbances and bounded uncertainty conditions [119]. Due to the switching logic requirements, natural targets for SM controllers are devices that include power electronic converters. Applications of SM control also include industrial electric drives such as dc, permanent-magnet and induction motors [118], robotics [106] and automotive [64]. With regard to ESSs, SM control has been proposed for the regulation of SCES [61] and FES systems [62].

The SM control also shows some drawbacks. The switching logic, in fact, is prone to produce the *chattering* effect (see Fig. 5.3), which is a persistent high-frequency periodic motion around the sliding surface \mathcal{S} and is caused by the deviation of the real system from the ideal model. Typical inevitable causes of the chattering are small control delays, hysteresis and dead-bands of physical devices. Moreover, since the SM control is a model-dependent technique, its implementation for nonlinear systems is often a challenge. With this aim, the linear structure of the GEM highly simplifies the implementation of SM on ESSs.

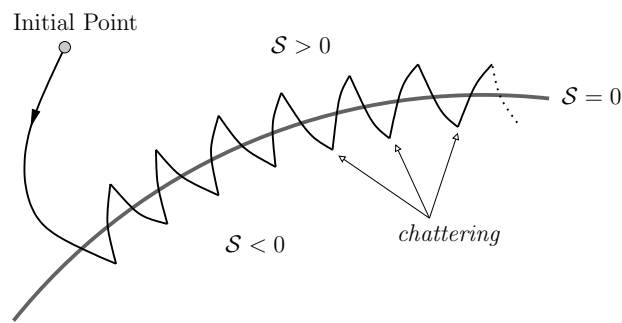


Figure 5.3: Graphical representation of the dynamic behavior of a sliding control. Note the chattering effect arising once the trajectory of the variable reaches the sliding surface \mathcal{S} .

The first step to formulate the SM for the GEM is to assume that the discontinuous output signal of the storage control, u , can be rewritten as the sum of two terms, as follows:

$$u = u_{\text{eq}} - K_{\text{SM}} \text{sign}(\mathcal{S}) \quad (5.3)$$

where u_{eq} is the equivalent continuous component of the control during the sliding mode operation; and K_{SM} is a positive gain designed to reduce the effect of external perturbations and disturbances. The rationale behind this assumption is given at the end of this section.

A sliding surface, \mathcal{S} , must be next chosen. Since the measured variable to be regulated, w , is generally an active power flow or a bus frequency (which highly depends on the active power injected) of the network, and the variables x_1 and x_2 of the GEM in (4.6) have the meaning of a potential and a flow, the following expression becomes a good candidate for \mathcal{S} :

$$\mathcal{S} = x_{f,u} - s_{x_{12}} x_1 x_2 \quad (5.4)$$

where $x_1 x_2$ has the unit of a power; $x_{f,u}$ is the filtered deviation of the measured signal w to be regulated ; and $s_{x_{12}}$ is a coefficient that accounts for the unit of the variables in \mathcal{S} . Note that, during sliding mode operation, $\mathcal{S} = 0$.

Linearizing (5.4) around the equilibrium point for which the GEM in (4.6) is obtained:

$$(\mathcal{S} - \mathcal{S}_0) = (x_{f,u} - x_{f,u0}) - s_{x_{12}} [x_{20}(x_1 - x_{10}) + x_{10}(x_2 - x_{20})] \quad (5.5)$$

At the equilibrium point, $\mathcal{S}_0 = 0$ and $x_{f,u0} = 0$. Therefore:

$$\mathcal{S} = x_{f,u} + \mathbf{s}_x (\mathbf{x} - \mathbf{x}_0) \quad (5.6)$$

where $\mathbf{s}_x = -[s_{x_{12}} x_{20}, s_{x_{12}} x_{10}]$. If, at a given time t_{SM} , the trajectory falls on the sliding surface and $\dot{\mathcal{S}} = 0$, then $\mathcal{S} = 0$ for $t > t_{\text{SM}}$. Moreover, $\dot{x}_{f,u} = 0$ must hold during sliding mode. Hence, the derivative of (5.6) with respect to time is given by:

$$\dot{\mathcal{S}} = \dot{x}_{f,u} + \mathbf{s}_x \dot{\mathbf{x}} = \mathbf{s}_x \dot{\mathbf{x}} = 0 \quad (5.7)$$

and, from (4.6), one has:

$$\dot{\mathbf{S}} = \mathbf{s}_x \mathbf{T}_x^{-1} [\tilde{\mathbf{A}}\mathbf{x} + \tilde{\mathbf{B}}_u u + \tilde{\mathbf{B}}_v v_{\text{dc}} + \tilde{\mathbf{K}}_x] = 0 \quad (5.8)$$

The value of u that equals (5.8) to zero is the so-called *equivalent control*, u_{eq} , seen in (5.3), and can be defined from (5.8) as follows:

$$u_{\text{eq}} = -(\mathbf{s}_x \mathbf{T}_x^{-1} \tilde{\mathbf{B}}_u)^{-1} \mathbf{s}_x \mathbf{T}_x^{-1} [\tilde{\mathbf{A}}\mathbf{x} + \tilde{\mathbf{B}}_v v_{\text{dc}} + \tilde{\mathbf{K}}_x] \quad (5.9)$$

Therefore, SM can be applied to the ESS if $\mathbf{s}_x \mathbf{T}_x^{-1} \tilde{\mathbf{B}}_u \neq 0$. If any variable $x_i \in \mathbf{x}$ is algebraic, i.e., $\mathbf{T}_{x,ii} = 0$, \mathbf{T}_x^{-1} is not defined. A possible solution is to use the singular perturbation approach, i.e., assign $\mathbf{T}_{x,ii} = \epsilon$, with $0 < \epsilon \ll 1$, or pass such a variable through a low-pass filter.

5.3 Case Study: IEEE 14-Bus Test System

This section provides a comparison of the dynamic response of the three control strategies discussed above, i.e., PI, H_∞ and SM. With this aim, the IEEE 14-bus test system described in Section 3.4.1 is considered for the simulations.

Some modifications have been made in this network to study the interaction of the storage device with the rest of the system:

- The capacity of the synchronous generator placed in bus 1 is reduced by 5 times its original value.
- The synchronous generator placed in bus 2 is substituted by a 60-turbines wind power plant of the same power capacity.
- A 30 MW ESS is connected to bus 4.

In this case study, the stochastic process applied to the wind follows a Weibull's distribution (see Appendix B.2). Values of the mean wind speed, scale and shape factors are taken from [28]. Two wind profiles (low and high mean wind speed) have been used in the simulations, and data have been collected from the months of December and August at the height of 65 meters, respectively.

Two scenarios have been considered to study the performance of the ESS applying the three control strategies: in Subsection 5.3.1 the system faces a line outage, whereas a loss of load is considered in Subsection 5.3.2.

5.3.1 Line Outage

In this subsection, the contingency is the outage of the line that connects buses 2 and 4 at $t = 25$ s, during low wind (Fig. 5.4) and high wind (Fig. 5.5) periods. The wind speeds corresponding to this profiles are shown in Figs. 5.4(a) and 5.5(a), respectively. The system variable regulated by the ESS is the frequency of COI (ω_{COI}), and its evolution is depicted in Figs. 5.4(b), 5.4(c) and Figs. 5.5(b), 5.5(c) for the system without storage device and with storage regulated using each one of the control strategies in Section 5.2. For each controller, same control parameters are used in both scenarios in order to check how different operating conditions can affect their performance. The three controllers are able to greatly reduce the frequency fluctuations of the system before and after the line outage and for the two wind profiles. In both cases, the H_∞ control smooths these fluctuations slightly better than the other techniques.

Finally, Figs. 5.4(d) and 5.5(d) show the active power consumed/provided by the ESS. Positive power indicates that the ESS is storing energy, and vice versa. Before the line outage, the three techniques have a similar behavior. After the occurrence of the contingency, however, high frequency oscillations can be appreciated for the SM, due to the effect of the chattering commented in Subsection 5.2.3. It is relevant to note that the wind speed variation, and therefore, the change of the initial operating point, does not affect the performance of any of the controllers.

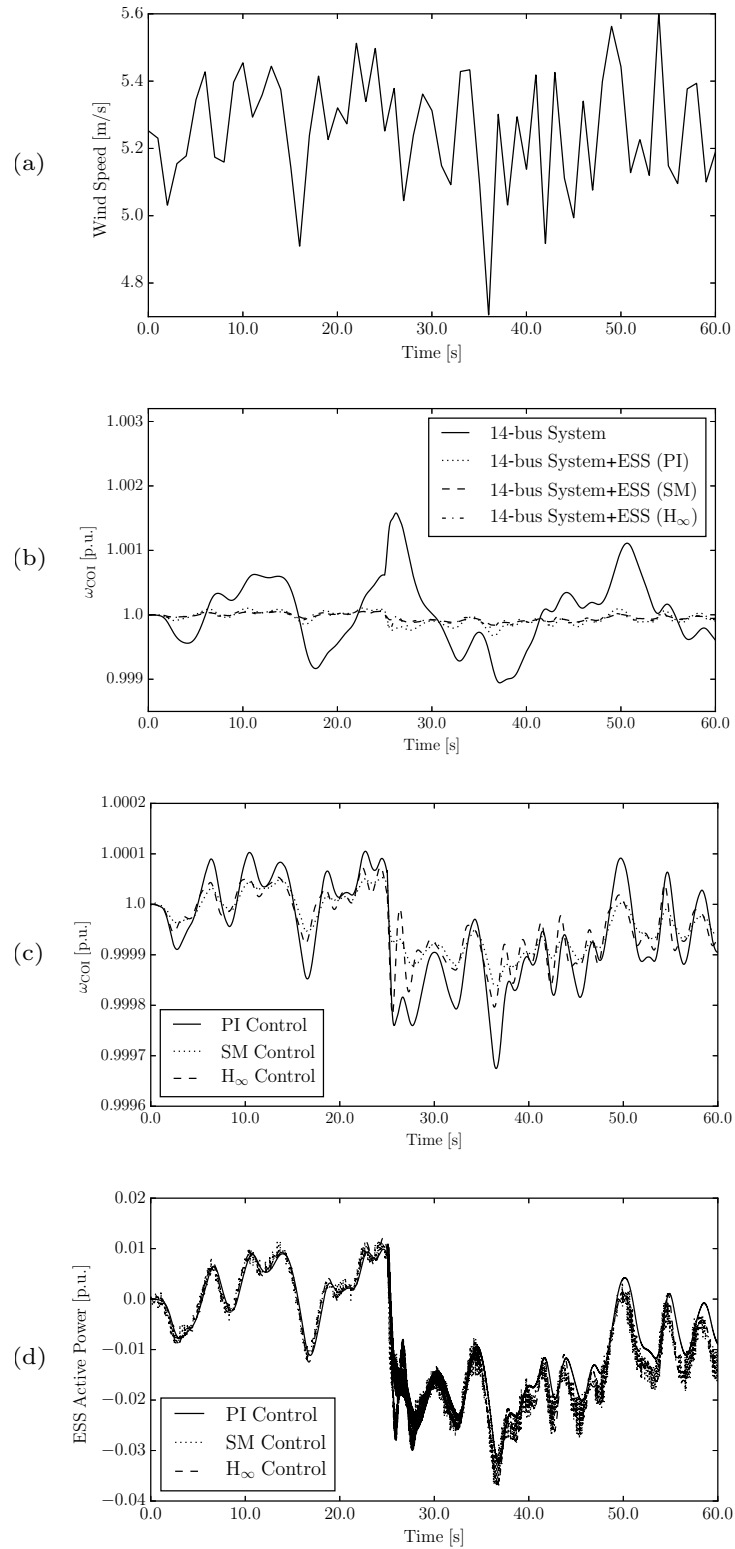


Figure 5.4: Response of the 14-bus system with an ESS following the opening of line 2-4 for a low wind profile. (a) Wind speed; (b), (c) Frequency of the COI; (d) Active Power of the ESS.

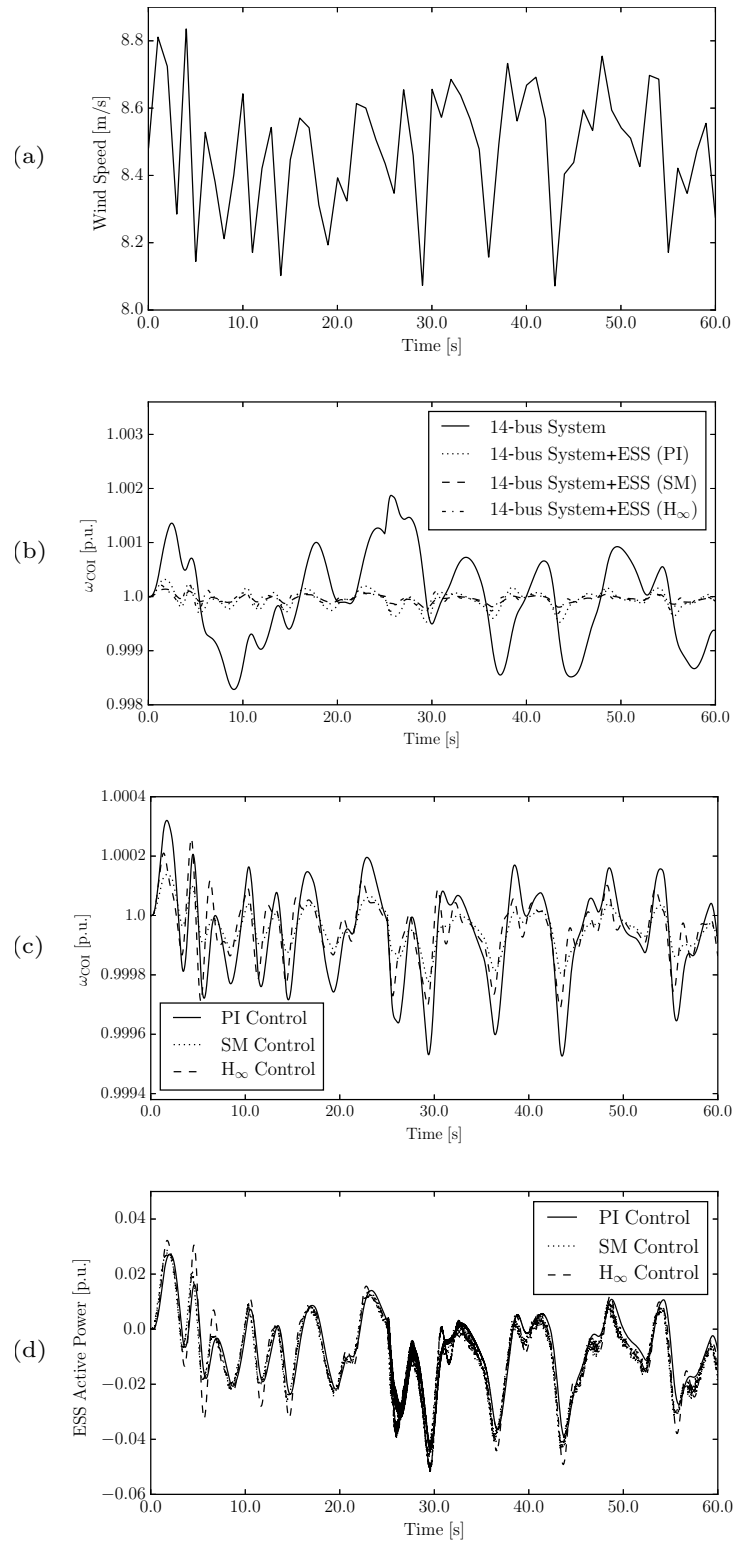


Figure 5.5: Response of the 14-bus system with an ESS following the opening of line 2-4 for a high wind profile. (a) Wind speed; (b), (c) Frequency of the COI; (d) Active Power of the ESS.

5.3.2 Loss of Load

To study the performance of the ESS regulated by the three controllers facing a large disturbance, the loss of load connected to bus 9 is simulated in this subsection (Fig. 5.6). The contingency occurs at $t = 25$ s during a high wind period (Fig. 5.6(a)). The regulated variable is again the ω_{COI} , and its evolution is shown in Figs. 5.6(b) and 5.6(c). The loss of the load causes a peak in the frequency greater than 1.5% (~ 1 Hz) that is not acceptable for the system. The inclusion of the ESS reduces this peak to about 0.6% in the case of the SM, and about 0.3% in the case of PI and H_∞ controllers. As in the previous cases, the H_∞ control behaves slightly better than the others during the transient, but the performance of the three is fairly similar before and after this transient. As in the previous example, the response of the controllers is not affected by the change in the operating condition that derives from the disconnection of the load. All three control strategies appear thus robust with respect to the loss of load considered in this study.

Figure 5.6(d) depicts the active power consumed/provided by the ESS. The SM shows relatively high oscillations after the disturbance, due to the time that this controller requires to reach the sliding surface. The H_∞ control, on the other hand, shows a quicker response but, because of that, also a greater storage of energy in the device is required. This fact is relevant if limits of the energy stored in the device are considered. Figure 5.7 shows the response of the system for the same scenario as in Fig. 5.6, except for the initial state of charge of the ESS, that is assumed to be closer to its upper limit. At about $t = 60$ s, the storage device regulated by the H_∞ control is not able to store more energy, causing a variation in the frequency of greater amplitude than after the loss of the load.

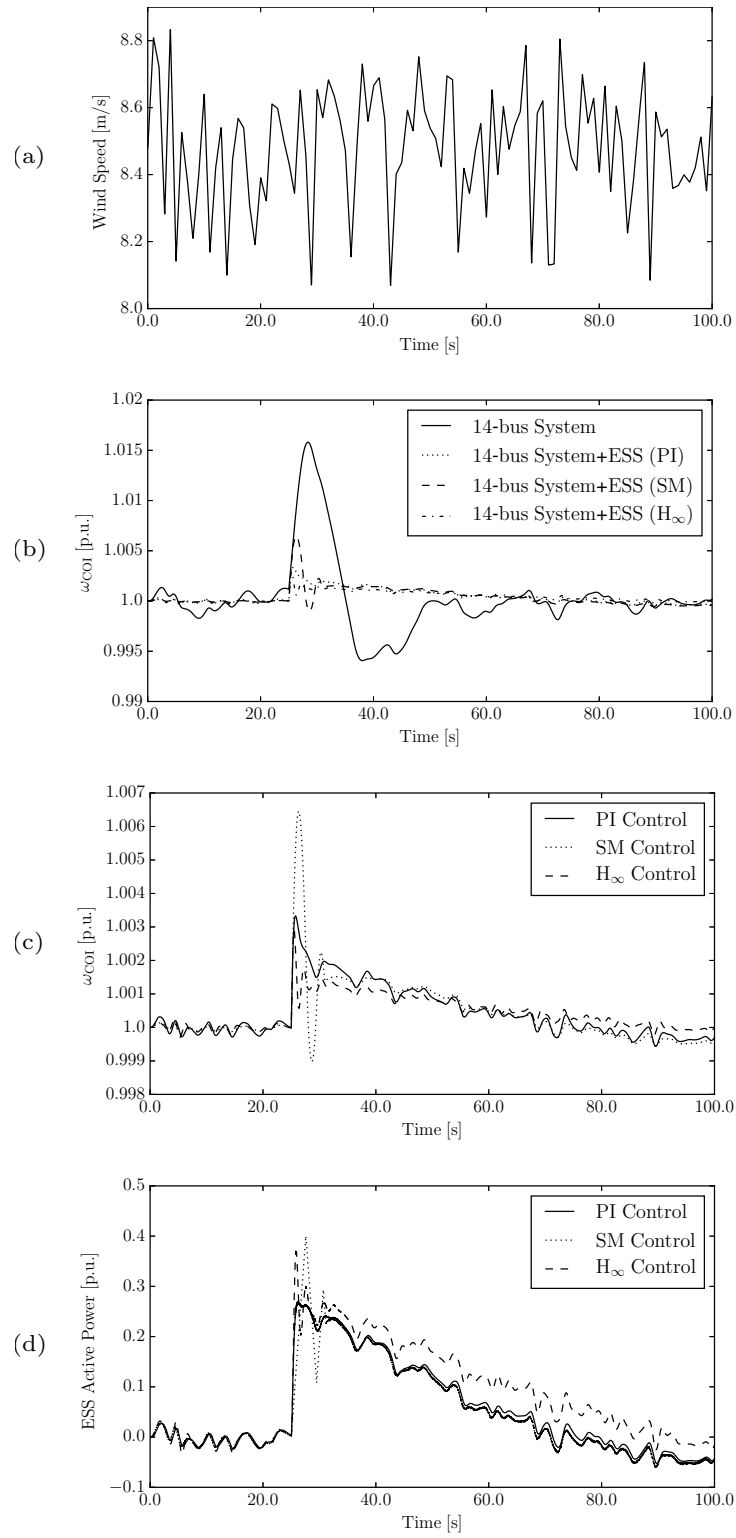


Figure 5.6: Response of the 14-bus system with an ESS following the loss of the load at bus 9 for a high wind profile. (a) Wind speed; (b), (c) Frequency of the COI; (d) Active Power of the ESS.

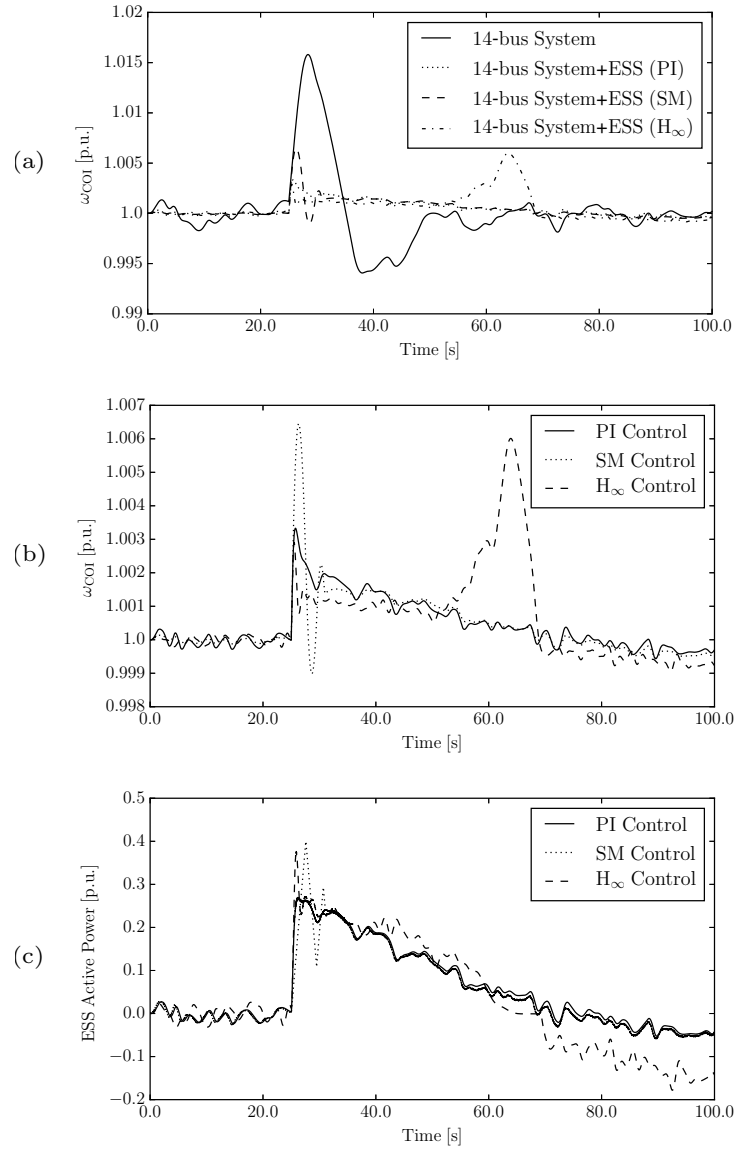


Figure 5.7: Response of the 14-bus system with an ESS following the loss of the load at bus 9 for a high wind profile and considering energy limits of the storage device. (a), (b) Frequency of the COI; (c) Active Power of the ESS.

5.4 Case Study: Irish Transmission System

In this section, the all-island Irish transmission system described in Subsection 3.5.1 is utilized to compare the dynamic behavior of the ESS controllers described in the previous section. The following remarks on the Irish system are relevant:

- Wind power plants do not provide primary frequency regulation, as it occurs in the actual Irish system.
- The wind speed profile of each wind power plant is modeled as an uncorrelated Weibull distribution (see Appendix B.2).
- Stochastic load variations are taken into account and modeled using Ornstein-Uhlenbeck processes (see Appendix B.1).

In 2015, the company Schwungrad Energie installed a pilot HESS in a site close to Rhode, county Offaly, Ireland, [104], consisting of a BES and a FES. The installation is still a prototype and currently not complete but the ultimate goal is to use the HESS to provide primary frequency regulation and/or regulate the active power flowing through a high voltage transmission line physically close to the HESS. The details of the regulations provided by the HESS have still to be agreed with the TSO [103, 34]. The power rating of the fully-operative HESS is expected to be about 20-30 MW. The FES will be responsible for filtering fast transients (≤ 1 minute) due to its speed of response, while the BES will provide active power reserves over longer periods thanks to its higher energy capacity and power rate.

For the purposes of this case study, a HESS composed of a 50 MW BES and a 20 MW FES are assumed to be installed at a bus representing the town of Rhode. Note that the size of the HESS is larger than those that are currently installed in practice. By increasing the size of the HESS, the system level impacts of the HESS dynamics can be better appreciated. Moreover, it is expected that the size of these devices will increase substantially in the near future.

The case study presented in this section considers both active power flow and frequency regulation of the ESS, stochastic variations of both the wind and the

loads, different system loading levels, and a variety of large disturbances such as faults followed by line outages, and the loss of generation units. The size of the grid, and the variety of scenarios considered in this section are designed to provide a fair and exhaustive comparison of the control techniques described in Section 5.2, in terms of performance against contingencies and disturbances, robustness against system uncertainties, computational burdens and possible numerical/technical issues, such as saturations.

This section is organized as follows. Subsection 5.4.1 compares the performance of the HESS controllers providing line active power control following the clearing of a three-phase fault and line disconnection. Subsection 5.4.2 assumes that the HESS provides primary frequency control and considers the outage of a synchronous machine of the system.

For the analysis provided in this section, the Monte Carlo method is used. With this aim, 1,000 time domain simulations are carried out for each case. Each simulation is solved for 20 s in Subsection 5.4.1, and for 25 s in Subsection 5.4.2, with a time step of 0.004 s when SM is applied, and 0.02 s otherwise. Note that, for the considered time scale, the response of the BES is too slow for the SM to be effective and, hence, only the FES is regulated with the SM, while the H_∞ is applied to the BES. Finally, again for the considered time scale, the energy saturations of the HESS are neglected.

5.4.1 Line Active Power Flow Regulation

In this subsection, it is assumed that the control of the HESS is designed to regulate the active power flowing through a high voltage transmission line of the Irish system, P_{line} , at 55 MW. The contingency is a three-phase fault near the regulated line occurring at $t = 15$ s. This is then cleared by means of the disconnection of a transmission line after 180 ms. Note that $t = 15$ s is chosen to make sure that the stochastic processes of the wind and the load are in stationary conditions.

For fair comparison, the PI is tuned in order to obtain as similar performance as possible to the H_∞ and SM controllers, as shown in Fig. 5.8(a) for a single trajectory. As an example of the HESS performance, the active power provided/consumed by the

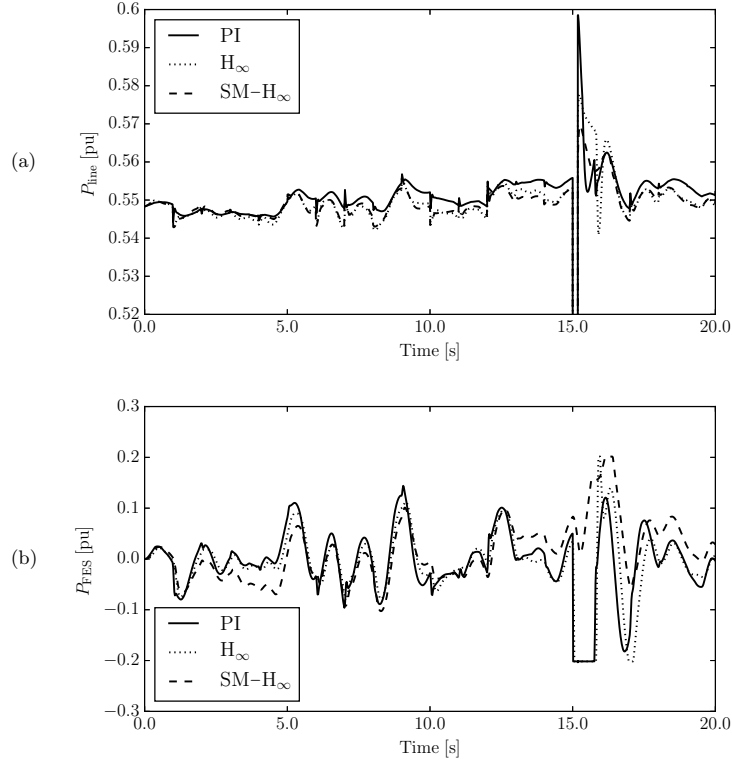


Figure 5.8: Irish system with HESS and a three-phase fault followed by a line trip. (a) Power flowing through the regulated line; (b) Active power provided/consumed by the FESS.

FES with each controller is shown in Fig. 5.8(b). Positive power indicates charging periods.

In the following, three different cases are considered: a base case loading condition, a 15% load increase, and a 15% load decrease.

5.4.1.1 Base Case Initial Loading Conditions

In this first case, the initial loading condition for each simulation is considered to be the same as the base case, i.e., the initial power flow of the regulated line is $P_{\text{line}}^0 = 55$ MW. This is also the reference power used for the HESS regulation.

The case without HESS is firstly considered. All the trajectories of P_{line} and their histogram and Probability Density Function (PDF) are calculated at $t = 20$ s, i.e., 5 s after the disturbance. The results are shown in Fig. 5.9, where the dashed and dotted lines represent μ_P and $\mu_P \pm 3\sigma_P$, respectively, with μ_P and σ_P the mean and the standard

deviation of P_{line} . It can be seen how the fault, along with the variations of the wind and the load, can cause variations of P_{line} of up to ± 6.6 MW ($\pm 12\%$) after the transient.

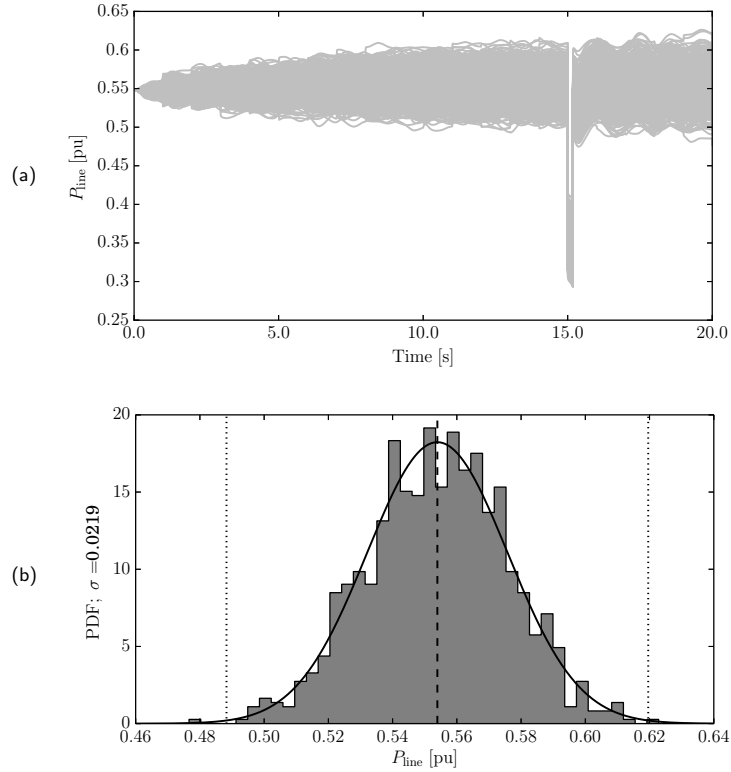


Figure 5.9: Irish system without HESS and a three-phase fault followed by a line trip: Active power flowing through the regulated line. (a) All trajectories; (b) Histogram and PDF-fit of the trajectories at $t = 20$ s. Dashed line: μ_P ; dotted lines: $\mu_P \pm 3\sigma_P$.

A similar analysis is carried out considering a HESS in the system when both FES and BES are regulated by the PI controller (Fig. 5.10(a)), the H_∞ controller (Fig. 5.10(b)), and the combination of SM- H_∞ controllers (Fig. 5.10(c)). From these figures, it can be observed how adding a HESS in the system can significantly reduce the variations of P_{line} by about 60-70%. Comparing σ_P , the best performance is obtained when the SM control is applied to the FES, and the H_∞ control to the BES.

The total computational time to obtain all 1,000 trajectories for each case is: 18 m and 35 s for PI, 18 m and 45 s for H_∞ , and 4 h and 15 m for SM and H_∞ . The reason why the computational time when SM is included is so high compared to the other techniques is because SM high frequency switching requires a much smaller time step for the time domain simulations. While the first two controllers consider a time step of 0.02 s, the

SM requires 0.004 s or smaller. Also, SM needs a higher number of iterations to solve each point of the time integration method (the implicit trapezoidal method is used in this study) whenever the SM switches its manifold. Clearly this numerical issue does not affect the actual implementation of the SM on the physical storage device.

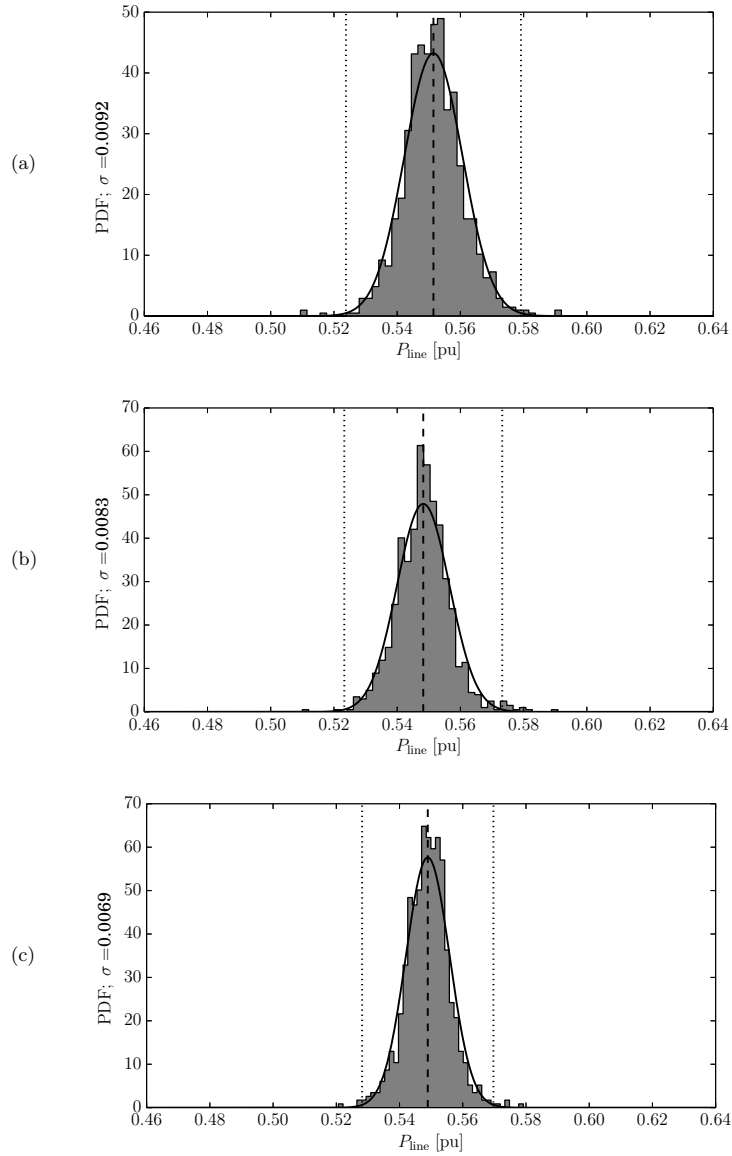


Figure 5.10: Irish system with HESS and a three-phase fault followed by a line disconnection: Active power flowing through regulated line. (a) PI control; (b) H_{∞} control; (c) SM- H_{∞} control. Dashed line: μ_P ; dotted lines: $\mu_P \pm 3\sigma_P$.

5.4.1.2 Variations of the Initial Loading Conditions

The robustness of each controller is studied in this subsection considering different initial loading conditions, namely a 15% load increase ($P_{\text{line}}^0 = 63.25$ MW) and a 15% load decrease ($P_{\text{line}}^0 = 46.75$ MW). These are also the reference powers used for the HESS regulation for each case. For this study, the wind generation is assumed independent from the load variations, and therefore the power provided by the wind power plants remains the same for the three loading conditions. The power balance is kept by varying the power generated by the synchronous machines proportionally to the load variations. The same control parameters used for the base case are used for all control strategies. The standard deviation σ_P of the values of P_{line} and the number of trajectories for which the FES and the BES reach current saturations, n_{sat} , at $t = 20$ s for each of the three scenarios are listed in Tables 5.1 and 5.2, respectively.

Table 5.1: Comparison of σ_P for different loading levels during a fault in the Irish system.

σ_P [p.u.]	No HESS	PI	H_∞	SM- H_∞
Base Case (55.0 MW)	0.0219	0.0092 (−57.99%)	0.0083 (−62.10%)	0.0069 (−68.49%)
15% Load Increase (63.25 MW)	0.0251	0.0110 (−56.18%)	0.0101 (−59.76%)	0.0093 (−62.95%)
15% Load Decrease (46.75 MW)	0.0188	0.0079 (−57.98%)	0.0068 (−63.83%)	0.0059 (−68.62%)

Table 5.2: Comparison of n_{sat} of the HESS for different loading levels during a fault in the Irish system.

n_{sat}	PI	H_∞	SM- H_∞
Base Case (55.0 MW)			
FES	75	1 (−98.67%)	103 (+37.33%)
BES	269	116 (−56.88%)	51 (−81.04%)
15% Load Increase (63.25 MW)			
FES	48	0 (−100.0%)	61 (+27.08%)
BES	201	55 (−72.64%)	27 (−86.57%)
15% Load Decrease (46.75 MW)			
FES	78	1 (−98.72%)	132 (+69.23%)
BES	343	158 (−53.94%)	75 (−78.13%)

The following are relevant remarks on the comparison of line active power flow regulation of the HESS from Tables 5.1 and 5.2:

- For all scenarios, the highest reduction of P_{line} variations is obtained when SM and H_{∞} are applied to the FES and BES, respectively.
- Comparing σ_P , the PI is, counter-intuitively, the least sensitive to variations of the system loading level in terms of regulation capability.
- The PI has the highest probability of reaching current saturation of the HESS overall. The SM saturates the FES the most, since the effort to reach the sliding surface after a contingency is mainly taken by this device due to its fast response. On the other hand, the probability of the BES of reaching saturation in this case is the lowest in all scenarios. Finally, H_{∞} has the lowest probability of current saturations of the HESS overall. Note that the FES saturations in this case are very unlikely.
- Current saturations of the HESS are overall more likely for lower loading levels for all control strategies studied. As the initial loading level decreases, the overall inertia of the system is also reduced. This fact makes the system less resilient to large perturbations, which in turns results in higher variations of P_{line} , and thus, to a greater contribution of the HESS.

5.4.2 Primary Frequency Regulation

In this scenario, the system variable regulated by the HESS is the frequency of the bus that the storage device is connected to. With this aim, the frequency divider formula described in Subsection 3.2.3 is used to estimate the bus frequency. The contingency considered is the disconnection, at $t = 15$ s, of one of the synchronous machines of the system. The active power provided by the generation unit is 50 MW. Stochastic variations of both the wind speeds and the load power demands are also included in order to simulate system volatility in power production and consumption, respectively.

The same four cases discussed in subsection 5.4.1, namely no HESS, and with HESS applying PI, H_{∞} , and SM- H_{∞} controllers, are considered. Also in this scenario, the PI

Table 5.3: Comparison of σ_ω and $\Delta\mu_\omega$ for different HESS controllers during a synchronous machine outage in the Irish system.

	No HESS	PI	H_∞	SM- H_∞
Before Loss of Sync. Machine				
σ_ω [Hz]	0.0124	0.0081 (-34.68%)	0.0079 (-36.29%)	0.0079 (-36.29%)
Frequency Nadir				
$\Delta\mu_\omega$ [Hz]	0.06	0.0415 (-30.83%)	0.03 (-50.00%)	0.035 (-41.67%)
σ_ω [Hz]	0.0125	0.0076 (-39.20%)	0.0067 (-46.40%)	0.007 (-44.00%)
After Loss of Sync. Machine				
σ_ω [Hz]	0.013	0.0081 (-37.69%)	0.0088 (-32.31%)	0.0079 (-39.23%)

regulator is initially tuned so to show a dynamic performance as similar as possible to the H_∞ and SM. Then, 1,000 simulations are performed for each case, and the results of the standard deviations of the bus frequency, σ_ω , and the highest variation of the frequency means, $\Delta\mu_\omega$, are listed in Table 5.3 for three conditions: right before the contingency, at the frequency nadir, and 10 s after the generation unit outage.

Several observations can be made based on Table 5.3, as follows.

- Before the occurrence of the contingency, all controllers provide a fairly similar robustness against fluctuations of wind speeds and load powers.
- The highest reduction of both $\Delta\mu_\omega$ and σ_ω at the frequency nadir is obtained when applying H_∞ control, followed by the combined SM- H_∞ controller.
- The SM- H_∞ strategy provides the best behavior 10 seconds after the loss of the synchronous machine, whereas the H_∞ controller provides the poorest performance.

5.5 Concluding Remarks

Based on simulation results, the following conclusions can be drawn.

- i. Overall, the most robust behavior of the HESS is achieved by applying the SM control to the FES and the H_∞ control to the BES. This combination is found to be the most effective to reduce both active power and frequency fluctuations. However, this approach shows the highest probability of current saturations of the FES.
- ii. Applying H_∞ to both FES and BES provides the lowest probability that current saturations will be experienced by the HESS. This approach provides also the highest reduction in frequency nadir variations after the loss of a synchronous machine. On the other hand, its performance is surpassed by the SM- H_∞ controller for all other considered cases.
- iii. While the dynamic performance of the PI control is overall the worst of the three techniques, it nevertheless shows a fair robustness against different loading conditions and contingencies, and system uncertainties. Moreover, the PI reduces the number charge/discharge processes and current saturations of the ESS when compared to the SM control, thus improving the operational life of the storage device. In other words, the PI control provides a good trade-off between performance and simplicity of implementation and design. Therefore, the PI control can be used to provide a preliminary study of the behavior of the ESS in a power system, e.g., to check if the chosen location is the best one possible, and then H_∞ or SM control can be finally designed and applied to the ESS.
- iv. Despite the deterministic nature of H_∞ and SM, all controllers have an heuristic component in their formulation and designs (gains of the PI regulator, K_u of the H_∞ controller, and K_{SMC} of the SM). These have to be carefully tuned to achieve an acceptable performance of the controllers. This is an important practical remark that is seldom pointed out in the literature that describes robust control techniques.

6 | Stochastic Transient Stability Analysis of Transmission Systems with Inclusion of Energy Storage Devices

6.1 Motivation

Power system stability is the ability of an electric power system, for a given initial operating condition, to regain a state of operating equilibrium after being subjected to a physical disturbance, with most system variables bounded so that practically the entire system remains intact [58].

While power system stability analysis has always been an important area of study, it has recently regained popularity due to the high penetration of non-dispatchable energy resources. Power systems may undergo several forms of instabilities according to their physical nature, the size of the disturbances, the time frame of interest, etc. (see Fig 6.1).

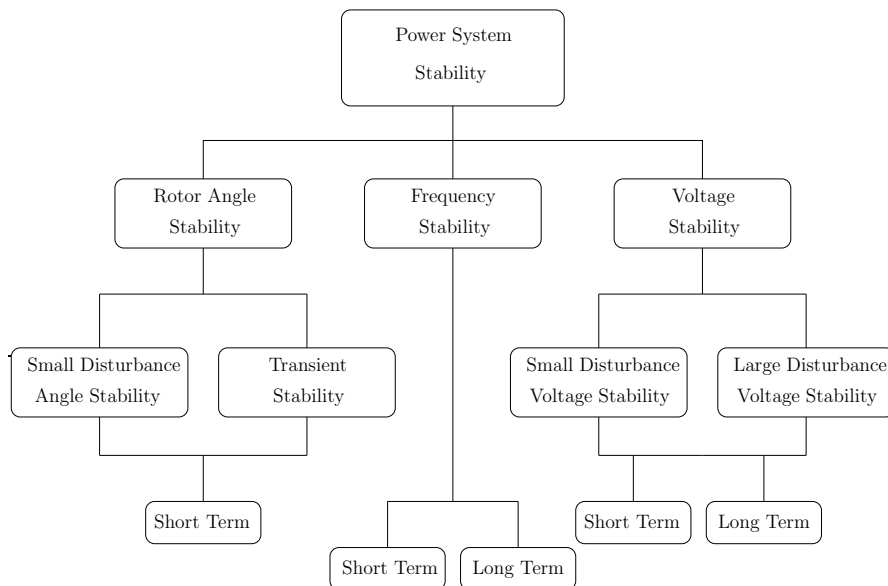


Figure 6.1: Classification of the categories of power system stability.

Three main categories can be defined according to the physical nature of the instability: frequency stability, rotor angle stability and voltage stability. The frequency stability of the power system with inclusion of ESSs has been studied in previous chapters. On the other hand, since one of the main components of the ESSs studied in this work is the VSC device, their impact on the voltage stability will be similar to the one provided by FACTS devices. Therefore, this chapter will focus on the transient stability (i.e., large-disturbance rotor angle stability), which is defined below:

Transient stability refers to the ability of synchronous machines of an interconnected power system to remain in synchronism after being subjected to a large disturbance. It depends on the ability to maintain/restore equilibrium between electromagnetic torque and mechanical torque of each synchronous machine in the system. Instability that may result occurs in the form of increasing angular swings of some generators leading to their loss of synchronism with other generators [58].

The potential of VSC-based ESSs to provide ancillary services to a transmission grid has been demonstrated in the previous chapters, and in the references therein. These services include flattening the power provided by non-conventional power plants based on renewable sources (e.g., wind power plants), active power regulation in a transmission line, local and/or global frequency regulation, and Rate of Change of Frequency (RoCoF) mitigation. While these objectives are the main reasons that justify the economic viability of such devices, the ESS inherent ability to control both active and reactive powers is also expected, as a relevant byproduct, to increase the Critical Clearing Times (CCTs) associated with a fault, thus improving the transient stability of the system [63]. There is a lack, however, of studies that analyze in a systematic way the contribution of ESSs to the system transient stability following a large disturbance. Moreover, these studies usually consider only one ESS technology, deterministic simulations, and/or small and simple test networks [63, 4, 3]. This chapter aims to fill this gap and provides a comprehensive analysis that quantifies the impact of different VSC-based ESSs on the transient stability of a large transmission system modeled as a set of SDAEs.

The remainder of the chapter is organized as follows: Section 6.2 illustrates the contribution of ESSs to the improvement of the system transient stability. The different existing approaches to study the transient stability of power systems are described in

Section 6.3. Section 6.4 presents an exhaustive probabilistic Transient Stability Analysis (TSA) based on the stochastic model of the all-island Irish transmission system with a variety of ESSs, as well as with a Static Synchronous Compensator (STATCOM) device. Finally, concluding remarks are drawn in Section 6.5.

6.2 Effect of ESSs on the Transient Stability of Power Systems

This section explains, through qualitative examples, the effect on transient stability of installing a VSC-based ESS in a power system. With this aim, the well-known One-Machine Infinite-Bus (OMIB) system is considered, and the Equal Area Criterion (EAC) is applied [50]. The section is organized as follows: Subsection 6.2.1 explains graphically the transient stability of the OMIB. The effect of the reactive and active power supports provided by an ESS is then studied separately in Subsections 6.2.2 and 6.2.3, respectively.

6.2.1 One-Machine Infinite-Bus

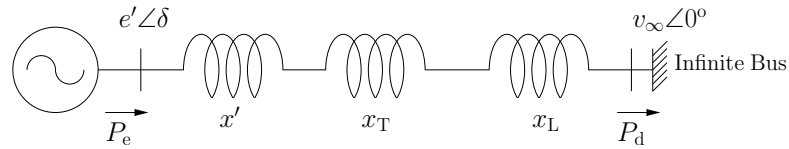


Figure 6.2: Scheme of a generator connected to an infinite bus through a transformer and a transmission line.

Consider the case of a lossless OMIB with a step-up transformer, depicted in Fig. 6.2. The swing equation of the machine can be expressed as:

$$2H\dot{\omega} = P_m - P_e = P_d - P_e = P_{acc} \quad (6.1)$$

where ω is the rotor speed of the machine; H and ω_0 are the inertia constant and the synchronous mechanical rotor speed of the machine, respectively; P_m and P_e are the mechanical and electrical powers of the machine, respectively; and P_d is the system demand power. In steady-state (pre-fault) conditions, $P_{m,0^-} = P_{d,0^-}$ to guarantee $\omega = 1$ p.u., and thus, the acceleration power, P_{acc} , is null.

The electrical power supplied by the generator, P_e , is given by:

$$P_e = \frac{e'v_\infty}{x_{eq}} \sin \delta \quad (6.2)$$

where x_{eq} is the equivalent reactance of the internal machine impedance, x' , and the reactances of the transformer, x_T , and the line, x_L .

Consider δ_0 for which $P_e = \frac{e'v_\infty}{x_{eq}} \sin \delta_0 = P_m$. Assuming that the fault has zero impedance, and that both pre- and post-contingency conditions are the same, the EAC can be thus graphically represented by plotting P_e as a function of δ , as shown in Fig. 6.3, where δ_{cl} is the angle at the time of the fault clearance; and δ^{\max} is the maximum rotor angle.

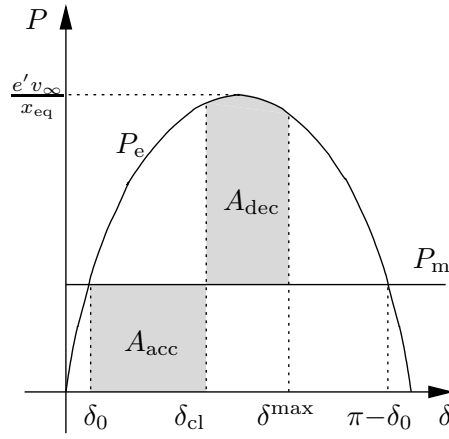


Figure 6.3: EAC of an OMIB system.

The generator will remain in synchronism if there exists a δ^{\max} such that the decelerating area, A_{dec} , equals the accelerating area, A_{acc} :

$$A_{acc} = \int_{\delta_0}^{\delta_{cl}} P_{acc} d\delta = \int_{\delta_{cl}}^{\delta^{\max}} P_{dec} d\delta = A_{dec} \quad (6.3)$$

The critical clearing angle, δ_{cr} , is thus obtained when $\delta^{\max} = \pi - \delta_0$. If $\delta_{cl} > \delta_{cr}$, the machine will lose synchronism.

6.2.2 One-Machine Infinite-Bus with a STATCOM device

The core device of the ESSs studied in this thesis is the VSC. With this aim, the effect on the transient stability of the installation of a STATCOM device in the OMIB system of

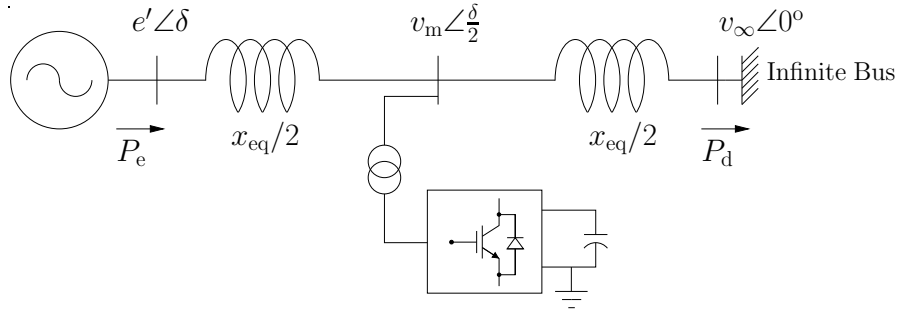


Figure 6.4: Scheme of a generator connected to an infinite bus with the inclusion of a STATCOM device.

Fig. 6.2 is considered first [125]. Figure 6.4 depicts the OMIB system with a STATCOM device connected at equal electrical distance between the machine and the infinite bus.

Assuming that the STATCOM regulates the bus voltage such that $v_m = v_\infty$, the electrical power supplied by the generator is now expressed as:

$$P_e = \frac{e'v_\infty}{x_{eq}/2} \sin \frac{\delta}{2} \quad (6.4)$$

Note that in (6.4) it was assumed that $e' = v_m = v_\infty$, so that the angle difference is $\frac{\delta}{2}$.

Comparing (6.4) with (6.2), it can be seen that the modulus of P_e has doubled, while the angle has halved. The EAC is then applied, and the result is shown in Fig. 6.5.

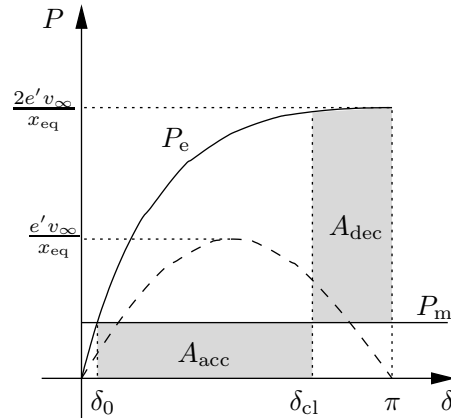


Figure 6.5: EAC of an OMIB system. Solid line: with STATCOM. Dashed line: without STATCOM

The inclusion of the STATCOM (solid line) increases δ_{cr} with respect to the one obtained in the previous subsection (dashed line), thus increasing the stability of the OMIB system against large disturbances.

6.2.3 One-Machine Infinite-Bus with an ESS

In this subsection, the effect of active power support on the system stability is studied, and a storage device is installed in the OMIB system, as depicted in Fig. 6.6.

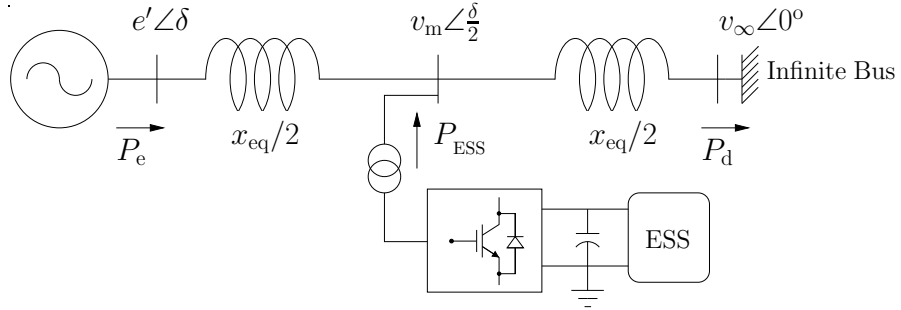


Figure 6.6: Scheme of a generator connected to an infinite bus with the inclusion of an ESS.

In steady-state situation, the active power supplied/consumed by the ESS, P_{ESS} is null. However, during and after a large disturbance such as a fault, $P_{ESS} \neq 0$, and depending on the location of the fault, different response of the ESS is observed, as represented in Fig. 6.7. Note that the ESS is assumed to have instantaneous response.

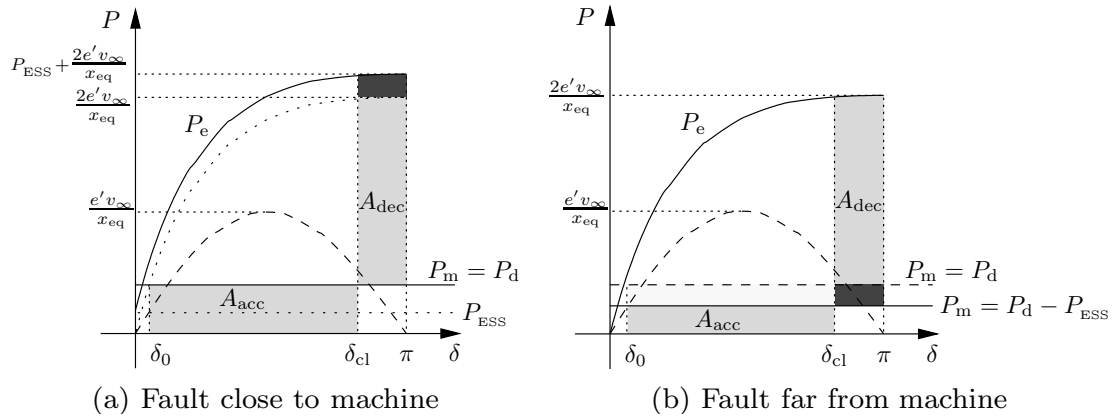


Figure 6.7: EAC of an OMIB system. Solid line: with ESS. Dashed line: without ESS

If the fault is located between the generator and the ESS (Fig. 6.7(a)), during the transient the fault acts as a “*barrier*”, limiting the active power support from the ESS. After the clearance of the fault, P_{ESS} can be supplied, thus increasing the decelerating area of the machine (dark grey area). On the other hand, if the fault occurs further than the location of the ESS with respect to the synchronous machine, depending on the speed of response of the ESS, P_{ESS} can be supplied before the fault clearance (Fig. 6.7(b)). Therefore, from the generator point of view, the demand is reduced, and thus: $P_{\text{m}} = P_{\text{d}} - P_{\text{ESS}}$. As a result, the accelerating area is reduced (light grey area), and the decelerating area is increased (dark grey area), thus increasing the fault CCT.

In the remainder of this chapter, the effect of VSC-based ESSs on the transient stability of power systems is studied through a probabilistic stochastic analysis, and considering a large, more complex system such as the Irish transmission grid.

6.3 Probabilistic Stochastic Transient Stability Analysis

The approach that has been most widely utilized to study the transient stability of power systems is through time domain simulations applying deterministic stability criteria [8, 68]. With this aim, N-1 and/or N-2 criteria are applied by selecting and simulating the most critical contingencies that can occur based on the knowledge of the power system under study. However, these contingencies are, generally, also the less likely to occur in the system. Thus, results from this approach are, usually, too conservative. Moreover, this method does not properly take into account the uncertainties of the power system (e.g., power generated by RESs, load levels, network topology changes, etc.).

In recent years, the complexity and uncertainty of power systems has significantly increased, along with the computational power of modern simulators. These facts have inspired the development of new techniques to study the transient stability of present power systems. One of these new approaches consists in carrying out a probabilistic TSA [22, 21, 126]. In this kind of analysis, the probability of occurrence of relevant contingencies is defined prior to the study, leading to more “credible” results. Moreover, the stochastic nature of power systems is usually taken into account at the beginning of the time domain simulation, being the system deterministic for the rest of the simulation. This approach, while providing more consistent and comprehensive results than the

conventional TSA, does not consider the stochastic behavior of the different components of the power system during the simulation, which can degrade the quality of the results for long simulations.

Another technique to study the TSA of power systems, based on stochastic calculus, has been presented in the literature [40]. In this approach, commonly known as Stochastic Transient Stability Analysis (STSA), the system is modeled as a set of SDAEs that take into account the different system uncertainties during the entire simulation, such as loads levels and system faults. While this technique can provide more accurate information of the stability of the system against any kind of faults, it can be computationally too demanding for large power system models.

In this work, the main features of the probabilistic and stochastic approaches have been considered to provide a comprehensive study of the contribution of ESSs to the transient stability of a large power system. In particular, the following assumptions are made:

- *Uncertainties in the load and generation are taken into account at the beginning of the simulation.* The rationale behind is that load variations are generally slow when compared to the time of the simulation for TSA. On the other hand, the power generated by RESs, which can represent up to 50% in modern power systems, are characterized by certain variability and uncertainty in their forecasts. With this aim, initial load and RES generation levels are randomly selected by using a normal distribution, with the base loading and generation conditions as mean values. In this manner, most extreme conditions are also the less likely to occur, as it happens in real power systems.
- *Different topologies are considered to account for uncertainties in system faults.* The implementation and simulation of stochastic models for system faults such as the ones presented in [40] can be a challenge and too demanding for large power systems. Instead, this thesis considers a small set of different topologies of the network to account for the possible relative locations of the fault with respect to the main devices of the power system such as the synchronous machines and the ESSs studied. A set of different fault clearing times are also considered to study the probability of losing synchronism for each of them.

6.4 Case Study: Irish Transmission System

The STSA of ESSs provided in this chapter is again based on the dynamic model of the all-island, 1,479-bus Irish transmission system, used in Section 5.4. In this case study, a 40 MW/100 MVar FES and a 50 MW/100 MVar BES are studied separately in order to better understand the impact of each individual device on the transient stability of the system. The area where the ESS is installed (Co. Clare) includes a synchronous machine that provides 139 MW and 15 MVar as well as several wind power plants and loads. The controllers of both FES and BES devices are designed to regulate the frequency. This can be either the local frequency measured at the point of connection of the storage device (ω_{bus}) or the frequency of the center of inertia of the system (ω_{COI}). ω_{bus} is estimated by using the frequency divider formula (Subsection 3.2.3). Note that the power ratings of the FES and the BES are again larger than currently installed ones.

To study the interaction of the active and reactive power regulations provided by VSC-based ESS devices, the analysis is also carried out for a 100 MVar STATCOM device [125]. This device is coupled to the system through the same VSC as the ESS in Fig. 2.1, but does not include the storage device and control and can thus provide exclusively reactive power regulation.

The following are relevant assumptions on the system model:

- Wind speeds of the wind power plants are modeled using uncorrelated stochastic differential equations that reproduce Weibull distributions (see Appendix B.2).
- Load uncertainty is accounted through random loading levels in the range of $\pm 10\%$ with respect to base case conditions.
- VSC devices and control parameters are the same for the FES and the BES.
- STATCOM parameters are the same as those of the VSC device and controller contained in the ESS.

The analysis is based on the results of stochastic time domain simulations (1,000 simulations per scenario, 60 scenarios). The contingency is a three-phase fault, and two different locations of the fault are considered in order to represent two possible system

topologies according to the relative position of the fault and the ESS with respect to the synchronous machine. These topologies are qualitatively illustrated in Fig. 6.8.

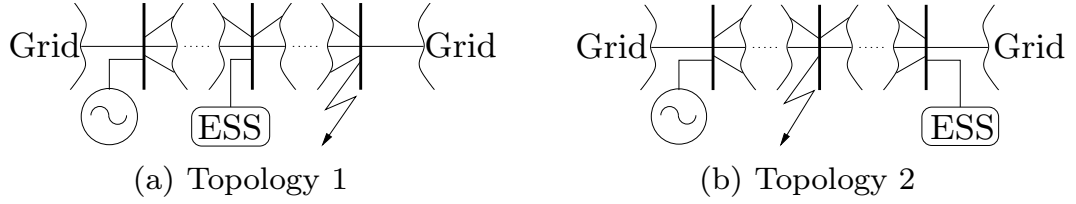


Figure 6.8: Topologies of a power system facing a fault. (a) Topology 1: The ESS and the synchronous machines are on the same side with respect to the fault; (b) Topology 2: The fault occurs between the synchronous machine and the ESS.

The percentage of simulations that are unstable due to the loss of synchronism of the machine is then computed for different clearing times (CTs), and shown in Tables 6.1 and 6.2, for each of the following scenarios:

- i. Irish system without ESSs.
- ii. One FES/BES providing local ω_{bus} control.
- iii. One FES/BES providing ω_{COI} control.
- iv. One STATCOM device providing local bus voltage, v_{ac} , control.

Note that both FES and BES devices also control v_{ac} through the quadrature component of the VSC.

Table 6.1: Percentage of unstable simulations after a three-phase fault for Topology 1 in the Irish system for different CTs.

CT [ms]	105	110	115	120	125
No ESS	25.3	44.4	65.6	83.1	99.9
ω_{bus} Control					
FES	3.0	26.2	46.5	65.0	85.1
BES	8.9	31.8	50.4	71.1	88.0
ω_{COI} Control					
FES	1.5	24.1	43.5	63.6	81.9
BES	2.4	25.4	43.9	64.2	82.1
v_{ac} Control					
STATCOM	5.8	28.9	47.0	67.5	84.7

Table 6.2: Percentage of unstable simulations after a three-phase fault for Topology 2 in the Irish system for different CTs.

CT [ms]	105	110	115	120	125
No ESS	29.8	48.7	69.4	86.5	100.0
ω_{bus} Control					
FES	19.2	41.0	57.0	80.2	97.7
BES	22.9	43.3	62.4	81.8	100.0
ω_{COI} Control					
FES	17.5	39.7	58.2	78.1	96.2
BES	17.8	39.8	59.1	78.2	96.6
v_{ac} Control					
STATCOM	16.7	39.1	57.4	76.9	95.5

6.5 Concluding Remarks

Tables 6.1 and 6.2 show that regardless the variable regulated and the topology considered, the ESS always improves the transient stability of the system. Moreover, due to its fast response, a 40 MW FES has a greater effect than a 50 MW BES in the system transient stability for all scenarios considered. These results are well aligned with expectations. However, other less intuitive results are obtained from the simulations.

- i. *The reactive power support of the ESS plays the major role in transient stability enhancement.* The comparison of the performances of ESS and STATCOM devices shows that the reactive regulation has a substantially greater impact than the active one. Sustaining the voltage during the fault, in fact, reduces the probability that the machine loses synchronism. Figure 6.9 compares the behavior of the system (Topology 1) with and without the reactive power support provided by the STATCOM device. The reduction of the v_{ac} drop (Fig. 6.9(a)) leads to a reduction of the rotor angle of the synchronous generator, δ_{syn} , (Fig. 6.9(b)), and so to an improvement of the transient stability of the system.
- ii. *Regulating the frequency of the COI provides fairly similar results than controlling a local bus frequency.* Following the transient caused by the fault, the trends of both ω_{COI} and ω_{bus} are similar in the system, and so the active power response of the ESS. This fact, and the greater impact of the reactive power support, lead

to such small differences between the regulation strategies on the system transient stability. Figure 6.10 compares δ_{Syn} during a fault (Topology 2) when the FES is regulating ω_{bus} and ω_{COI} .

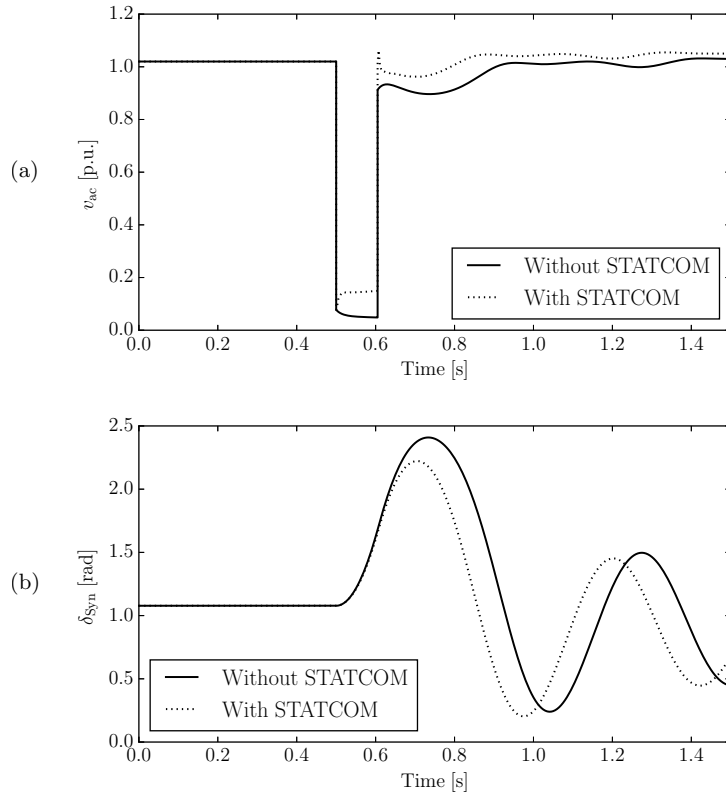


Figure 6.9: Response of the Irish transmission system during a three-phase fault (Topology 1). (a) ac voltage of the bus of connection of the STATCOM/ESS; (b) Rotor angle of the synchronous machine.

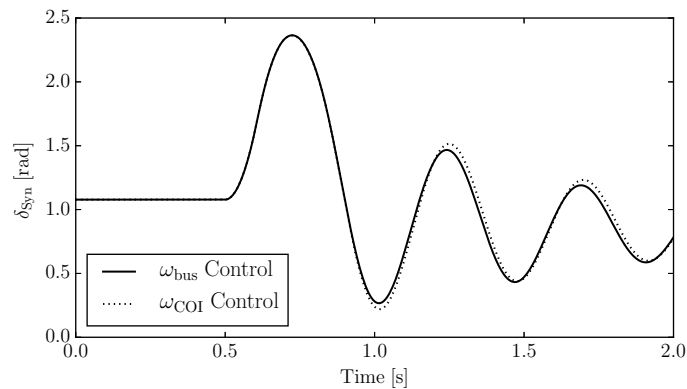


Figure 6.10: Rotor angle of the synchronous machine during a three-phase fault (Topology 2) with a FES regulating ω_{bus} and ω_{COI} .

- iii. *If the fault occurs between the synchronous machine and the ESS, the support provided by the latter is substantially diminished.* This is due to the closer location of the fault with respect to the synchronous machine, and to the “*barrier effect*” that the fault creates between the machine and the ESS, limiting the support provided by the latter. This is represented in Fig. 6.11, which compares δ_{Syn} during a fault for the two different topologies. The system includes a BES that regulates ω_{bus} , and same fault length (110 ms) and initial system loading (base case conditions) are considered.

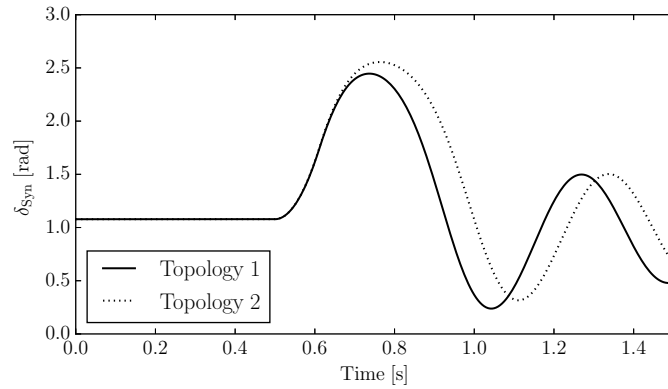


Figure 6.11: Rotor angle of the synchronous machine during a three-phase fault for the two topologies with a BES regulating ω_{bus} .

- iv. *The STATCOM device outperforms the ESS in some scenarios.* One would expect that the ESS, in the worst case, performs as good as a STATCOM device. However, this is not always the case, especially when the BES regulates the ω_{bus} . While the STATCOM regulates v_{ac} and v_{dc} separately, the ESS couples the control of v_{dc} and the control of the storage device (whose output is the current injected into the dc link of the VSC, i_{dc}). This coupling, along with the nonlinear relation $p_{\text{dc}} = v_{\text{dc}}i_{\text{dc}}$, appears to affect the overall behavior of the ESS. If the dynamics of the storage device and/or of its controller are not sufficiently fast (as in the case of the BES) the overall performance of the ESS can be less effective than the STATCOM alone. Moreover, recent studies suggest that current saturations of the VSC increase the risk of instability of the converter [123]. Fast, large transients such as three-phase faults may require a big amount of active power to be supplied/absorbed by the storage device very quickly, increasing the risk of saturation of the ESS, and therefore, reducing the CCT of the fault.

7 | Conclusion and Scope for Future Work

With the increase of the penetration of renewable energy sources in power systems, it is necessary to develop new techniques and strategies to optimally regulate the frequency of the system and its rate of change. VSC-based ESSs are expected to be one of the main players to improve the stability and behavior of low-inertia power systems. In this thesis, the dynamic modeling, control, and transient stability of VSC-based ESSs are studied in detail. Moreover, an exhaustive and comprehensive analysis of the features and performance of different ESS technologies and control techniques in a variety of systems and scenarios is presented. The most relevant conclusions of this work are drawn in the remainder of this chapter.

A generalized model of energy storage devices (GEM) for voltage and angle stability analysis has been firstly proposed in Chapter 4. Such a model allows simulating different technologies using a fixed set of DAEs and parameters. Simulation results show that the proposed model is able to accurately reproduce the dynamic behavior of detailed transient stability models for large disturbances, namely faults and loss of loads, and across their whole operating cycle. The nonlinearity of ESS controllers, i.e., hard limits, are also properly taken into account by the proposed model. On the other hand, other overly simplified ESS models that have been presented in the literature, and that represent only active and reactive power control dynamics, prove to be significantly less accurate than the GEM. Since, in the proposed GEM, the storage device is formulated as a fixed set of linear DAEs, it appears to be particularly useful to synthesize and compare different control strategies for ESSs. Moreover, the same control scheme can be straightforwardly used for testing the dynamic response of different technologies. Limitations of the GEM are the need of the parameters of the detailed transient stability models of each ESS technology in order to obtain the parameters of the generalized model, and the small but inevitable lack of accuracy as the storage device approaches to its upper or lower state of charge limit.

Based on the GEM described in Chapter 4, a variety of ESS control strategies have been studied in Chapter 5. The features and mathematical formulations of the commonly-used PI regulator, as well as the H_∞ and SM controllers, have been duly defined and explained in detail. A comparison of these control strategies based on the well-known IEEE 14-bus test system is provided first. In this comparison, a generic ESS is tested when the system faces line outages and loss of loads, for a variety of stochastic wind profiles. Simulation results show the overall good performance of each technique, including the PI-based control, when perturbations and contingencies of different nature affects the system. The H_∞ controller proves to regulate slightly better than the others, but is more sensitive to energy saturations of the storage device. A second statistical study of the PI, H_∞ and SM controllers, based on a stochastic model of the all-island Irish transmission system with a hybrid ESS installed, is next provided. The case study considers both line active power flow and primary frequency regulation provided by each controller for a large variety of scenarios, including generation and load stochastic fluctuations. Simulation results show again the good performance of each control technology for all scenarios, being the combination of SM and H_∞ the best option. The good trade-off between performance and complexity of the PI control makes this technique a good candidate for a first testing of the ESS that is being installed in the system. Once the location of the ESS, as well as its main objective in the power system regulation are decided, H_∞ or SM can be designed and implemented at the final stage of the installation of the ESS.

A stochastic analysis of the transient stability of the Irish transmission system with inclusion of an ESS device has been presented in Chapter 6. The performance of the ESS is tested against three-phase faults in different locations of the network, and compare to that of a STATCOM device. The case study provides both intuitive and less intuitive results. As expected, one can conclude that the ESS is able to increase considerably the critical clearing times of the faults that can occur in the system. The improvement of transient stability through ESS devices is fairly insensitive with respect to the kind of frequency signal (local or system-wide) utilized in the control. On the other hand, less intuitively, the performance of the ESS is not always better than that of a STATCOM. Moreover, such a performance highly depends on the relative position of the ESS with respect to both the fault and synchronous machines, as well as on the energy storage

technology. Statistical information on potential fault locations appears thus to be crucial for the optimal placement of ESSs, as this increases the probability that such a device can properly support synchronous machines against faults. Finally, it appears that the performance of the ESS can be optimized if the controls of v_{dc} and i_{dc} are decoupled, as this would help minimize the negative effect of nonlinearity and slow dynamics of the ESS.

The work presented in this thesis provides a comprehensive and thorough discussion on the theory, modeling and numerical appraisal needed to properly study the dynamic behavior of VSC-based ESSs. These devices are expected to be key for the frequency regulation of low-inertia power systems in the near future. Therefore, it is crucial to start studying the interaction of these devices with the rest of the system, along with the optimization of economical aspects, which so far has been the main focus of the research on ESSs.

Future Work

The work presented in this thesis can be extended in several different ways.

Further investigation can be performed to validate the FD formula proposed in Chapter 3. With this aim, data from real measures from Phasor Measurement Units (PMUs), or results from Electromagnetic Transient Program (EMTP) simulations can be used to test the accuracy of the FD.

The GEM presented in Chapter 4 can lay the foundation of the definition of a standard model for transient stability analysis of ESSs. The parameters required to define the dynamic behavior of the GEM are, in fact, always the same regardless the technology and the size of the ESS. Moreover, the definition of the GEM for other VSC-based ESSs that are not included in this thesis (e.g., variable-speed PHES), and that may be developed in the future, can be carried out.

Other advanced control strategies for ESSs can be developed based on the GEM. With this aim, fuzzy logic (FLC) and model predictive (MPC) controllers appear relevant. In particular, MPC is suitable for the design of secondary frequency control,

due to its ability to coordinate several devices at a time, and to take appropriate steps to optimize the performance of the overall system. Moreover, MPC can be used to coordinate not only several ESSs but also primary controllers of conventional synchronous machines and RESs, thus effectively integrating all devices able to regulate the active power into the AGC.

While this thesis focuses on ESSs in transmission grids, the studies presented can be conducted considering other networks. Firstly, in distribution systems, the difference between the frequency variations in buses that are within a certain neighborhood are very small. If an ESS is installed in such a neighborhood, its controller can take an average frequency of measures from several surrounding buses, rather than a single frequency at the bus of connection, thus reducing noises and other numerical issues in the signals. In this regard, the proposed FD formula becomes apparent. Secondly, the accuracy of the GEM can be tested in other than transmission grids, such as distribution networks, and/or islanded grids. Finally, the enhancement of the transient stability of such systems with ESSs is another interesting research topic.

Finally, with the increasing number of small-scale, highly-distributed ESSs in the distribution grid such as residential batteries and electric vehicles (while the latter is not a ESS in itself, it has the potential to provide certain regulation during their charge periods), the definition of an aggregated statistical transient stability model of these distributed small ESSs becomes apparent. The dynamic behavior of such an aggregated model and control can be sensibly addressed by means of stochastic differential equations, taking into account the probability distribution of the availability and state of charge of ESSs.

Appendix

A | Storage Input Limiter

This appendix discusses and illustrates, through time domain simulations, the dynamic behavior of the Storage Input Limiter (SIL) of the control scheme described in Subsection 2.1.1 (see Fig. A.1) [91]. With this aim, the WSCC 9-bus test system described in Section 4.3 is used for all simulations. The storage device considered in this case study is a 40 MW BES and is connected to bus 8.

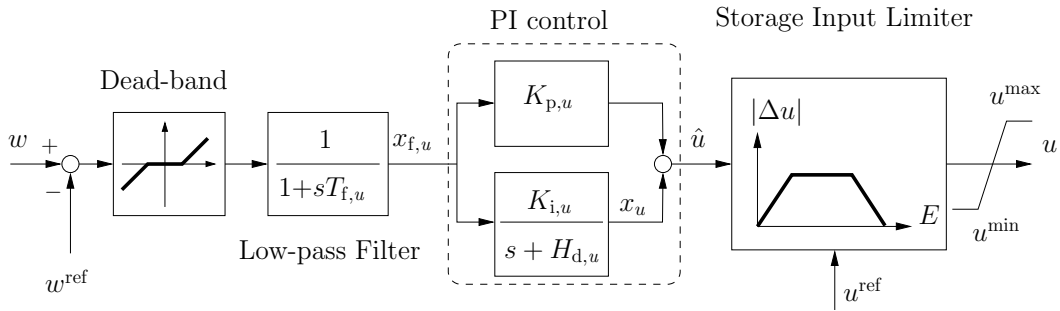


Figure A.1: Storage control scheme.

Particularizing the proposed SIL to the BES model described in Section 2.2.1, it is straightforward to relate the energy and its limits in (2.1) and (2.2) to the SOC_B of the battery in (2.10). The output of the controller, u , is the duty cycle of the dc/dc converter in (2.11), S_B . Finally, if $\Delta u < 0$ the BES is charging and, if $\Delta u > 0$, discharging.

Two scenarios are considered: Section A.1 shows the response of the WSCC system with a BES facing a deterministic variation of one load, whereas Section A.2 includes stochastic perturbations for all loads.

A.1 Deterministic Variation of Load

As an example of the performance of the proposed SIL when the BES reaches its maximum and minimum storable energy, Fig. A.2 shows the response of the WSCC system in case of deterministic variations of the load. The disconnection of a 40 MW load occurs at bus 5 at $t = 10$ s, and is reconnected after 70 s. Finally, a 50 MW load is connected to bus 5 at $t = 130$ s and is disconnected after 110 s.

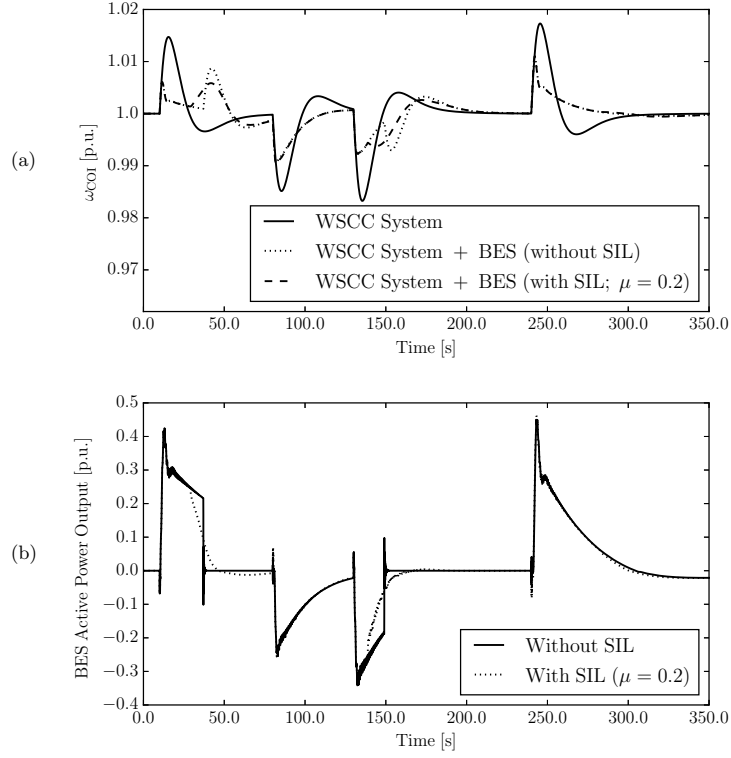


Figure A.2: Response of the WSCC system with a BES to deterministic variations of the load. (a) Frequency of the COI; (b) Active power output of the BES.

In this example, the frequency of the COI (ω_{COI}) of the system is regulated, and its performance is shown in Fig. A.2(a). It can be observed from Fig. A.2(a) that without BES, the largest variation of ω_{COI} is around 1.8%. This variation is reduced by 50% when the BES is included in the system. Figure A.2(a) also shows the effect of the energy saturations of the BES after about 40 s (maximum level) and 150 s (minimum level) of simulation. The inclusion of the SIL ($\mu = 0.2$) avoids the abrupt variations of the ω_{COI} caused by these saturations.

The active power output of the BES with and without SIL is compared in Fig. A.2(b). The SIL smooths the control of the input signal of the BES when is reaching one of its limits, and thus, avoids the step decrease (increase) of the power consumed (injected) by the BES.

A.2 Stochastic Variation of Load

For this case study, stochastic perturbations have been considered for all loads. These stochastic processes have been modeled by using the Ornstein-Uhlenbeck's (see Appendix B.1).

A step size of $h = 0.01$ s has been used to generate the trajectories of the Wiener's process, and 1000 simulations are performed for each scenario. The initial load and generation levels are set by using a uniform distribution with $\pm 5\%$ of variation with respect to their original values. The step size for the time integration Δt is set to 0.1 s, and the final simulation time is 200 s.

As for the previous section, the regulated variable ω_{COI} and its evolution is depicted in Fig. A.3 for the 1000 simulations of each scenario: (i) WSCC system (Fig. A.3(a)); (ii) WSCC system and an oversized BES (Fig. A.3(b)); (iii) WSCC system and an undersized BES without SIL (Fig. A.3(c)); and (iv) WSCC system and an undersized BES with SIL (Fig. A.3(d)). The maximum and minimum levels of the SOC_{B} of the battery in scenarios depicted in Figs. A.3(c) and A.3(d) have been set with the aim of obtaining a relatively high probability to reach energy saturation. As it can be observed from Figs. A.3(a) and A.3(b), using an oversized BES that never reaches energy saturations reduces the variations of ω_{COI} by about 60% with respect to the system without storage. On the other hand, Fig. A.3(c) shows that energy saturations of the BES causes transients that lead to frequency variations even larger than those obtained by the system without battery, whereas Fig. A.3(d) demonstrates that the inclusion of the SIL ($\mu = 0.2$) reduces the amplitude of such transients, getting a similar performance than in the case with the oversized BES.

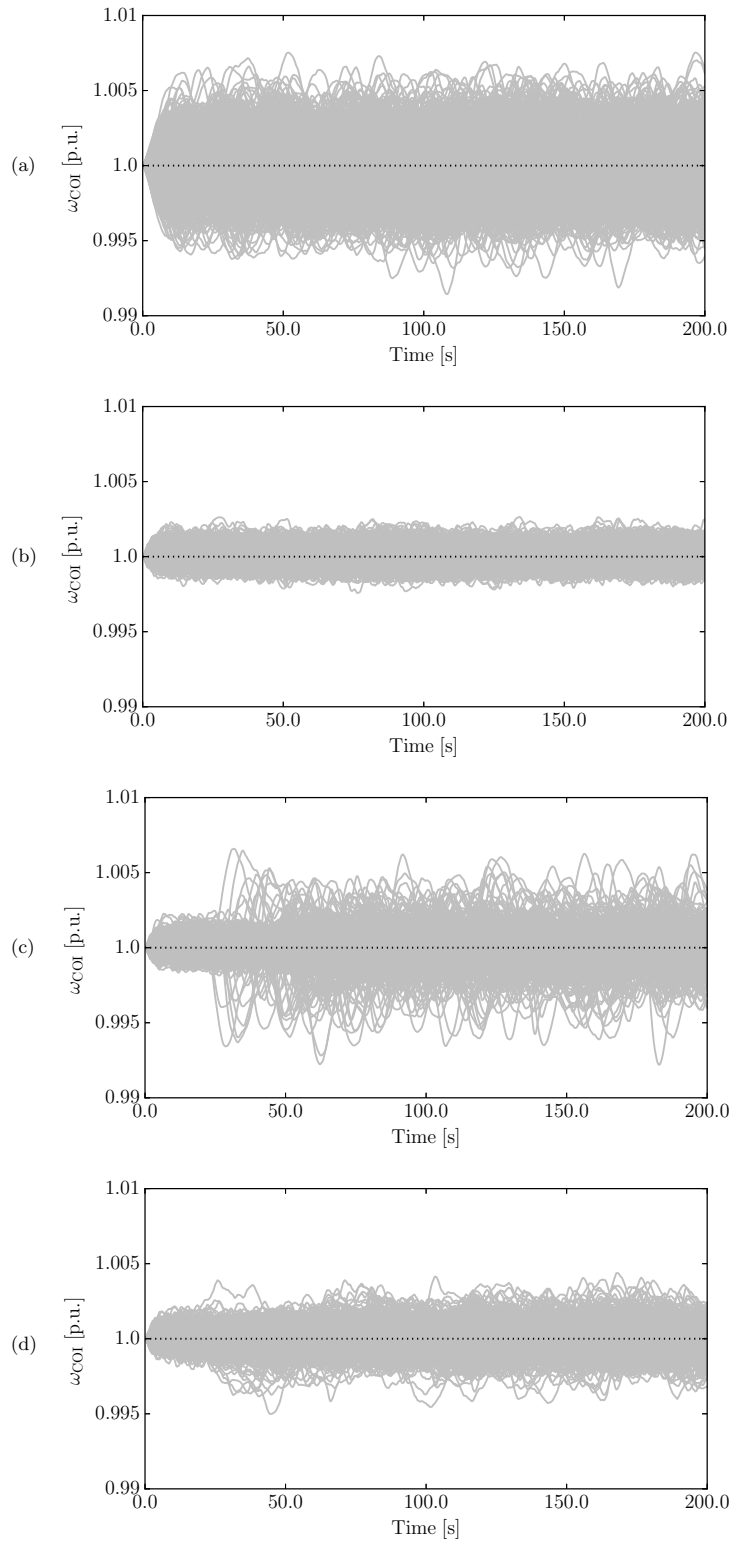


Figure A.3: Frequency of the COI when stochastic perturbations are considered for the loads. (a) WSCC System; (b) WSCC System + BES (oversized); (c) WSCC System + BES (without SIL); (d) WSCC System + BES (with SIL; $\mu=0.2$)

A.3 Concluding Remarks

Simulation results show that the SIL is able to smooth abrupt transients caused by the energy saturation of the BES. The stochastic analysis shows that the proposed control block allows reducing the size of the ESS while maintaining acceptable dynamic performance, thus leading to a reduction of the cost of the device. The simplicity of this control strategy, which only requires to set the maximum and minimum storable energy thresholds, allows to easily implement this control block to all sorts of VSC-based ESSs described in this thesis.

B | Stochastic Models of Wind and Loads

This appendix presents the SDAEs that represent the stochastic processes applied in this work to the load demand profiles (B.1) and the wind speeds (B.2).

The use of continuous SDAEs appears as a natural choice as the standard power system model for transient angle and voltage stability analysis is based on DAEs which can be assumed continuous except for a reduced set of discrete events [52]. The interested reader can find further discussion on the modelling of power systems as a set of SDAEs in [82].

B.1 Load Stochastic Processes

Uncorrelated stochastic processes of the loads have been considered in this work. These are modeled by using the Ornstein-Uhlenbeck's process, also known as *mean-reverting* process [97, 49, 82]. The main feature of the Ornstein-Uhlenbeck's process that makes it interesting in this context is its property to keep the standard deviation bounded. This appears as a sensible feature in several physical processes, where the variability and/or uncertainty does not increase with time. The stochastic load model used in this work is defined by the following set of SDAEs:

$$\begin{aligned} p_L(t) &= (p_{L0} + \eta_p(t))(v(t)/v_0)^\gamma \\ \dot{\eta}_p(t) &= \alpha_p(\mu_p - \eta_p(t)) + b_p\xi_p \end{aligned} \tag{B.1}$$

where p_L is the active power of the loads, p_{L0} represents the initial active load power; v_L is the voltage magnitude at the bus where the load is connected; v_{L0} is the initial value of the bus voltage magnitude; exponent γ_L is a parameter that characterizes the dependence of the load with respect to voltage; η_p is the stochastic variable; α_p and b_p are the *drift* and *diffusion* of the stochastic process, respectively; μ_p is a pre-specified mean value; and ξ_p is the white noise. Similar equations are used to define the trajectories of load reactive powers. The interested reader can find a detailed description of this model in [82].

B.2 Wind Stochastic Processes

In this work, the stochastic process applied to the wind follows a Weibull's distribution [78]:

$$f(v_w, c_w, k_w) = \frac{k_w}{c_w^k} v_w^{k-1} e^{-\left(\frac{v_w}{c_w}\right)^{k_w}} \quad (\text{B.2})$$

where v_w is the wind speed, and c_w and k_w are the scale and shape factors, respectively. Time variations of the wind speed, $\xi_w(t)$, are computed as follows:

$$\xi_w(t) = \left(-\frac{\ln \iota(t)}{c_w} \right)^{\frac{1}{k_w}} \quad (\text{B.3})$$

where $\iota(t)$ is a uniform variate generator of random numbers ($\iota \in [0, 1]$). Finally, the wind speed is computed setting the initial average speed v_w^a determined at the initialization step as mean speed:

$$\check{v}_w(t) = (1 + \xi_w(t) - \xi_w^a) v_w^a \quad (\text{B.4})$$

where ξ_w^a is the average value of $\xi_w(t)$. To emulate the autocorrelation of the wind speed, i.e., to avoid unrealistic sudden jumps, the wind speed is processed through a low pass filter before entering into the wind turbine equations.

Other, more sophisticated, SDAE-based models to represent wind stochastic processes have been proposed in the literature, e.g., [127], and are beyond the scope of this thesis.

C | Map of the All-Island Irish Transmission

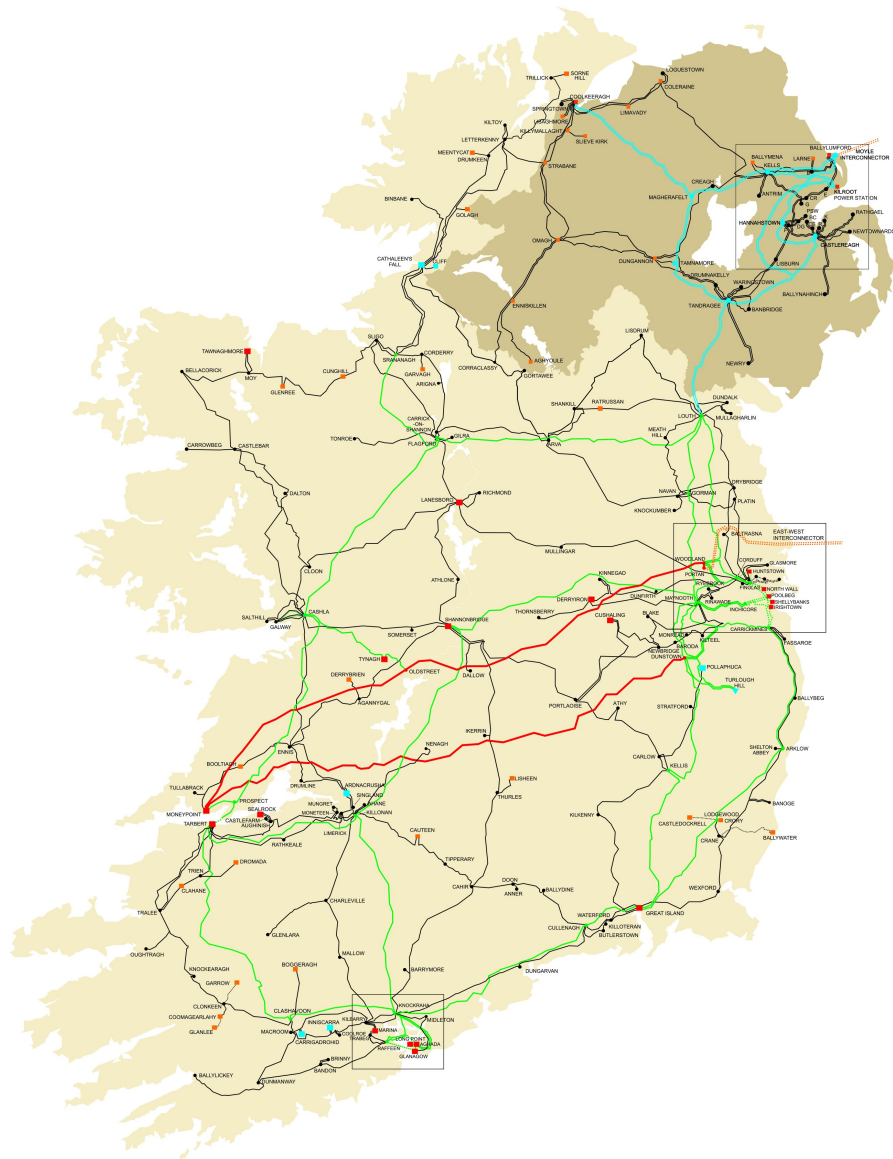


Figure C.1: Schematic map of the all-island Irish transmission system [42].

Bibliography

- [1] E. Acha and B. Kazemtabrizi, "A New STATCOM Model for Power Flows Using the Newton-Raphson Method," *IEEE Transactions on Power Systems*, vol. 28, no. 3, pp. 2455–2465, Aug. 2013. 16
- [2] A. A. Akhil, G. Huff, A. B. Currier, B. C. Kaun, D. M. Rastler, S. B. Chen, A. L. Cotter, D. T. Bradshaw, and W. D. Gauntlet, *DOE/EPRI Electricity Storage Handbook in Collaboration with NRECA.*, Feb 2015. [Online]. Available: <http://www.osti.gov/scitech/servlets/purl/1170618> 2, 3, 5, 19
- [3] M. H. Ali and B. Wu, "Comparison of Stabilization Methods for Fixed-Speed Wind Generator Systems," *IEEE Transactions on Power Delivery*, vol. 25, no. 1, pp. 323–331, Jan 2010. 97
- [4] M. H. Ali, T. Murata, and J. Tamura, "Transient Stability Enhancement by Fuzzy Logic-Controlled SMES Considering Coordination With Optimal Reclosing of Circuit Breakers," *IEEE Transactions on Power Systems*, vol. 23, no. 2, pp. 631–640, May 2008. 97
- [5] M. H. Ali, B. Wu, and R. A. Dougal, "An Overview of SMES Applications in Power and Energy Systems," *IEEE Transactions on Sustainable Energy*, vol. 1, no. 1, pp. 38–47, Apr. 2010. 2, 25
- [6] O. Anaya-Lara, F. Hughes, N. Jenkins, and G. Strbac, "Contribution of DFIG-based Wind Farms to Power System Short-term Frequency Regulation," *IEE Proceedings on Generation, Transmission and Distribution*, vol. 153, no. 2, pp. 164–170, March 2006. 26
- [7] P. M. Anderson, *Analysis of Faulted Power Systems*. New York, NY: Wiley-IEEE Press, 1995. 30, 37
- [8] P. M. Anderson and A. A. Fouad, *Power System Control and Stability*, 2nd ed. Wiley-IEEE Press, 2003. 37, 61, 102
- [9] M. Aneke and M. Wang, "Energy Storage Technologies and Real Life Applications - A State of the Art Review," *ELSEVIER Applied Energy*, vol. 179, pp. 350–377, 2016. 4, 17
- [10] Y. M. Atwa and E. F. El-Saadany, "Optimal Allocation of ESS in Distribution Systems With a High Penetration of Wind Energy," *IEEE Transactions on Power Systems*, vol. 25, no. 4, pp. 1815–1822, Nov 2010. 5
- [11] A. S. A. Awad, J. D. Fuller, T. H. M. EL-Fouly, and M. M. A. Salama, "Impact of Energy Storage Systems on Electricity Market Equilibrium," *IEEE Transactions on Sustainable Energy*, vol. 5, no. 3, pp. 875–885, Jul. 2014. 54

- [12] V. Barbu and S. S. Sritharan, “ H_∞ Control Theory of Fluid Dynamics,” in *Proceedings of the Royal Society A: Mathematical, Physical and Engineering Science*, vol. 454, no. 1979. The Royal Society, 1998, pp. 3009–3033. 76
- [13] Beacon Power, “Beacon Power Operating Plants - Hazle Township, Pennsylvania.” [Online]. Available: <http://beaconpower.com/hazle-township-pennsylvania/> 22
- [14] Beacon Power, “20 MW Flywheel Energy Storage Plant.” [Online]. Available: http://www.sandia.gov/ess/docs/pr_conferences/2014/Thursday/Session7/02_Areseneaux_Jim_20MW_Flywheel_Energy_Storage_Plant_140918.pdf 22
- [15] M. Beaudin, H. Zareipour, A. Schellenberglabe, and W. Rosehart, “Energy storage for mitigating the variability of renewable electricity sources: An updated review,” *Energy for Sustainable Development*, vol. 14, pp. 302–313, 2010. 1, 17, 54
- [16] J. Beerten, S. Cole, and R. Belmans, “Modeling of Multi-Terminal VSC HVDC Systems With Distributed DC Voltage Control,” *IEEE Transactions on Power Systems*, vol. 29, no. 1, pp. 34–42, Jan. 2014. 14
- [17] P. Benner, V. Mehrmann, V. Sima, S. Van Huffel, and A. Varga, “SLICOT – A Subroutine Library in Systems and Control Theory,” *Applied and Computational Control, Signal and Circuits*, vol. 1, no. 10, pp. 499–539, Nov. 1999. 77
- [18] G. L. Berg, “Power System Load Representation,” *Proceedings of the IEEE*, vol. 120, no. 3, pp. 344–348, 1973. 37
- [19] H. Bevrani, A. Ghosh, and G. Ledwich, “Renewable Energy Sources and Frequency Regulation: Survey and New Perspectives,” *IET Renewable Power Generation, IET*, vol. 4, no. 5, pp. 438–457, Sept 2010. 26
- [20] S. P. Bhattacharyya, H. Chapellat, and L. H. Keel, *Robust Control: The Parametric Approach*. Prentice Hall, Jun. 1995, ch. 13. 76
- [21] R. Billinton and P. R. S. Kuruganty, “Probabilistic assessment of transient stability in a practical multimachine system,” *IEEE Transactions on Power Apparatus and Systems*, vol. PAS-100, no. 7, pp. 3634–3641, July 1981. 102
- [22] R. Billinton and P. R. S. Kuruganty, “A Probabilistic Index for Transient Stability,” *IEEE Transactions on Power Apparatus and Systems*, vol. PAS-99, no. 1, pp. 195–206, Jan 1980. 102
- [23] T. K. A. Brekken, A. Yokochi, A. von Jouanne, Z. Z. Yen, H. M. Hapke, and D. A. Halamay, “Optimal Energy Storage Sizing and Control for Wind Power Applications,” *IEEE Transactions on Sustainable Energy*, vol. 2, no. 1, pp. 69–77, Jan 2011. 5
- [24] Brown, Boveri & CIE (BBC), “Huntorf Air Storage Gas Turbine Power Plant.” [Online]. Available: https://www.eon.com/content/dam/eon-content-pool/eon/company-asset-finder/asset-profiles/shared-ekk/BBC_Huntorf_engl.pdf 2

- [25] L. Castro and E. Acha, "On the Provision of Frequency Regulation in Low Inertia AC Grids Using HVDC Systems," *IEEE Transactions on Smart Grid*, vol. PP, no. 99, pp. 1–11, 2015. 26
- [26] N. R. Chaudhuri, R. Majumder, B. Chauduri, and J. Pan, "Stability Analysis of VSC MTDC Grids Connected to Multimachine AC Systems," *IEEE Transactions on Power Delivery*, vol. 26, no. 4, pp. 2774–2784, Oct. 2011. 14
- [27] N. R. Chaudhuri, B. Chauduri, R. Majumder, and A. Yazdani, *Multi-terminal Direct-current Grids: Modeling, Analysis, and Control*. John Wiley & Sons, 2014. 14, 15, 16
- [28] A. Chauhan and R. Saini, "Statistical Analysis of Wind Speed Data Using Weibull Distribution Parameters," in *1st International Conference on Non Conventional Energy (ICONCE 2014)*, Kalyani, India, Jan. 2014, pp. 160–163. 81
- [29] C. Chen, S. Duan, T. Cai, B. Liu, and G. Hu, "Optimal Allocation and Economic Analysis of Energy Storage System in Microgrids," *IEEE Transactions on Power Electronics*, vol. 26, no. 10, pp. 2762–2773, Oct 2011. 5
- [30] C. Q. Choi, "Nitrogen Supercharges Supercapacitors," *IEEE Spectrum*, vol. 53, no. 2, p. 14, Feb. 2016. 23
- [31] Clean Technica, "Europe's Largest Battery Energy Storage Project Opens In Feldheim, Germany." [Online]. Available: <https://cleantechnica.com/2015/09/21/new-10-mw-storage-plant-opened-feldheim-germany-europes-largest/> 17
- [32] S. Cole, "Steady-State and Dynamic Modelling of VSC HVDC Systems for Power System Simulation," Ph.D. dissertation, Katholieke Universiteit Leuven, Sep. 2010. 15
- [33] Department of Communications, Marine and Natural Resources of Ireland, "Delivering a Sustainable Energy Future for Ireland," Government White Paper, 2007. [Online]. Available: http://www.seai.ie/About_Energy/Energy_Policy/European_Union_Drivers/EnergyWhitePaper12March2007.pdf 1
- [34] Department of Jobs, Enterprise and Innovation, Ireland, "First Hybrid-Flywheel Energy Storage Plant in Europe Announced in Ireland." [Online]. Available: <https://www.djei.ie/en/News-And-Events/Department-News/2015/March/First-Hybrid-Flywheel-Energy-Storage-Plant-in-Europe-announced-in-Midlands-.html> 87
- [35] DIgSILENT, *PowerFactory Technical Reference Ver. 15*, Gomaringen, Germany, 2015. 27, 29, 48
- [36] DOE Global Energy Storage Database, "Notrees Battery Storage Project - Duke Energy." [Online]. Available: <http://www.energystorageexchange.org/projects/11> 17
- [37] DOE Global Energy Storage Database, "Next Gen CAES using Steel Piping - NYPA." [Online]. Available: <http://www.energystorageexchange.org/projects/140> 19
- [38] DOE Global Energy Storage Database, "Beacon Power 20 MW Flywheel Frequency Regulation Plant." [Online]. Available: <http://www.energystorageexchange.org/projects/181> 22

- [39] Dominion Virginia Power, “Bath County Pumped Storage Station.” [Online]. Available: <https://www.dom.com/corporate/what-we-do/electricity/generation/hydro-power-stations/bath-county-pumped-storage-station> 2
- [40] Z. Y. Dong, J. H. Zhao, and D. J. Hill, “Numerical Simulation for Stochastic Transient Stability Assessment,” *IEEE Transactions on Power Systems*, vol. 27, no. 4, pp. 1741–1749, Nov 2012. 103
- [41] Duke Energy, “Notrees Windpower.” [Online]. Available: <https://www.duke-energy.com/commercial-renewables/notrees-windpower.asp> 17
- [42] EirGrid Group, “All Island Irish Transmission System Map.” [Online]. Available: <http://smartgriddashboard.eirgrid.com/#all/transmission-map> 48, 121
- [43] Electricity Supply Board (ESB), “Turlough Hill Pumped Storage Scheme – Co. Wicklow, Ireland.” [Online]. Available: <https://ruralelectric.files.wordpress.com/2015/10/tourlough-hill-pr-pamphlet.pdf> 2
- [44] Energiequelle, “Europe’s biggest battery storage system enters service.” [Online]. Available: <http://www.energiequelle.de/index.php/en/home/51-neuigkeiten-en/339-europe-s-biggest-battery-storage-system-enters-service> 17
- [45] A. Esmaili, B. Novakovic, A. Nasiri, and O. Abdel-Baqi, “A Hybrid System of Li-Ion Capacitors and Flow Battery for Dynamic Wind Energy Support,” *IEEE Transactions on Industry Applications*, vol. 49, no. 4, pp. 1649–1657, Aug. 2013. 2, 18
- [46] A. Etxeberria, I. Vechiu, H. Camblong, and J.-M. Vinassa, “Comparison of Sliding Mode and PI Control of a Hybrid Energy Storage System in a Microgrid Application,” in *International Conference on Smart Grid and Clean Energy Technologies*, Chengdu, China, Sep. 2011, pp. 966–974. 73, 75
- [47] J. Eyer and G. Corey, “Energy Storage for the Electricity Grid: Benefits and Market Potential Assessment Guide,” Sandia National Laboratories, Albuquerque, New Mexico, Tech. Rep. SAND2010-0815, Feb. 2010. 5
- [48] J. Fang, W. Yao, Z. Chen, J. Wen, and S. Cheng, “Design of Anti-Windup Compensator for Energy Storage-Based Damping Controller to Enhance Power System Stability,” *IEEE Transactions on Power Systems*, vol. 29, no. 3, pp. 1175–1185, May 2014. 54, 55
- [49] D. T. Gillespie, “Exact Numerical Simulation of the Ornstein-Uhlenbeck Process and its Integral,” *Physical Review E*, vol. 54, no. 2, pp. 2084–2091, 1996. 119
- [50] A. Gómez-Expósito, A. J. Conejo, and C. A. Cañizares, *Electric Energy Systems: Analysis and Operation*. Boca Raton, FL: CRC Press, 2009. 98
- [51] P. Hirsch, *Extended Transient-Midterm Stability Program (ETMSP), Ver.3.1 User’s Manual*, EPRI, 1994. 37, 39

- [52] I. A. Hiskens, "Power System Modeling for Inverse Problems," *IEEE Transactions on Circuits and Systems - I: Regular Papers*, vol. 51, no. 3, pp. 539–551, Mar. 2004. 119
- [53] C.-S. Hsu, M.-S. Chen, and W. Lee, "Approach for Bus Frequency Estimating in Power System Simulations," *IEE Proceedings-Generation, Transmission and Distribution*, vol. 145, no. 4, pp. 431–435, Jul 1998. 27, 28, 36
- [54] H. Ibrahim, A. Ilinca, and J. Perron, "Energy Storage Systems - Characteristics and Comparisons," *Renewable and Sustainable Energy Reviews*, vol. 12, pp. 1221–1250, 2008. 17
- [55] "Electrical Energy Storage," white paper, IEC, Dec. 2011. 1
- [56] IEEE Task Force on Benchmark Models for Digital Simulation of FACTS and Custom-Power Controllers, T&D Committee, "Detailed Modeling of Superconducting Magnetic Energy Storage (SMES) System," *IEEE Transactions on Power Delivery*, vol. 21, no. 2, pp. 699–710, Apr. 2006. 25
- [57] IEEE Task Force on Load Representation for Dynamic Performance, "Load Representation for Dynamic Performance Analysis [of Power Systems]," *IEEE Transactions on Power Systems*, vol. 8, no. 2, pp. 472–482, May 1993. 27, 28
- [58] IEEE/CIGRE Joint Task Force on Stability Terms and Definitions, "Definition and Classification of Power System Stability," *IEEE Transactions on Power Systems*, vol. 19, no. 2, pp. 1387–1401, May 2004. 96, 97
- [59] Illinois Center for a Smarter Electric Grid (ICSEG), "IEEE 39-Bus System," URL: <http://publish.illinois.edu/smartergrid/ieee-39-bus-system/>. 44
- [60] Illinois Center for a Smarter Electric Grid (ICSEG), "WSCC 9-Bus System," URL: <http://publish.illinois.edu/smartergrid/wsc-9-bus-system/>. 61
- [61] F. A. Inthamoussou, J. Pegueroles-Queralt, and F. D. Bianchi, "Control of a Supercapacitor Energy Storage System for Microgrid Applications," *IEEE Transactions on Energy Conversion*, vol. 28, no. 3, pp. 690–697, Sep. 2013. 23, 73, 78
- [62] D. Kairous and R. Wamkeue, "DFIG-based fuzzy sliding-mode control of WECS with a flywheel energy storage," *Electric Power System Research*, vol. 93, pp. 16–23, Dec. 2012. 73, 78
- [63] A. Kanchanaharuthai, V. Chankong, and K. A. Loparo, "Transient Stability and Voltage Regulation in Multimachine Power Systems Vis-à-Vis STATCOM and Battery Energy Storage," *IEEE Transactions on Power Systems*, vol. 30, no. 4, pp. 2404–2016, Sep. 2015. 97
- [64] Y.-W. Kim, G. Rizzoni, and V. Utkin, "Automotive Engine Diagnosis and Control Via Nonlinear Estimation," *IEEE Control Systems*, vol. 18, no. 5, pp. 84–99, Oct 1998. 78
- [65] S. K. M. Kodsı and C. A. Cañizares, "Modeling and Simulation of IEEE 14-bus System with FACTS Controllers," University of Waterloo, Waterloo, Tech. Rep. 2003-3, Mar. 2003. 40

- [66] P. C. Krause, O. Wasynczuk, and S. D. Sudhoff, *Analysis of Electric Machinery and Drive Systems*, 2nd ed. Wiley-IEEE Press, 2002. 20, 22, 37
- [67] S. Kundu, N. Sinitzyn, I. Hiskens, and S. Backhaus, “Modeling and Control of Thermostatically Controlled Loads,” in *17th Power Systems Computation Conference 2011, (PSCC 2011 STOCKHOLM)*, 2011, pp. 969–975. 39
- [68] P. Kundur, *Power System Stability and Control*. New York: McGraw-Hill, 1994. 102
- [69] G. Li, S. Cheng, J. Wen, Y. Pan, and J. Ma, “Power System Stability Enhancement by a Doubled Induction Machine with a Flywheel Energy Storage System,” in *Power Engineering Society General Meeting, IEEE*, Montreal, Que, 2006. 2, 23, 73
- [70] Lu Miao, Jinyu Wen, Hailian Xie, Chengyan Yue, and Wei-Jen Lee, “Coordinated Control Strategy of Wind Turbine Generator and Energy Storage Equipment for Frequency Support,” *IEEE Transactions on Industry Applications*, vol. 51, no. 4, pp. 2732–2742, July 2015. 26
- [71] C. A. Luongo, T. Baldwin, P. Ribeiro, and C. M. Weber, “A 100 MJ SMES Demonstration at FSU-CAPS,” *IEEE Transactions on Applied Superconductivity*, vol. 13, no. 2, pp. 1800–1805, Jun. 2003. 24
- [72] M. Makarov, M. Grossard, P. Rodríguez-Ayerbe, and D. Dumur, “Modeling and Preview H_∞ Control Design for Motion Control of Elastic-Joint Robots With Uncertainties,” *IEEE Transactions on Industrial Electronics*, vol. 63, no. 10, pp. 6429–6438, Oct 2016. 76
- [73] J. L. Mathieu, S. Koch, and D. S. Callaway, “State Estimation and Control of Electric Loads to Manage Real-Time Energy Imbalance,” *IEEE Transactions on Power Systems*, vol. 28, no. 1, pp. 430–440, 2013. 26, 39
- [74] J. M. Mauricio, A. Marano, A. Gómez-Expósito, and J. L. M. Ramos, “Frequency Regulation Contribution Through Variable-Speed Wind Energy Conversion Systems,” *IEEE Transactions on Power Systems*, vol. 24, no. 1, pp. 173–180, Feb 2009. 26
- [75] P. Mercier, R. Cherkaoui, and A. Oudalov, “Optimizing a Battery Energy Storage System for Frequency Control Application in an Isolated Power System,” *IEEE Transactions on Power Systems*, vol. 24, no. 3, pp. 1469–1477, Aug. 2009. 5, 70
- [76] R. D. Middlebrook and S. Cuk, “A General Unified Approach to Modelling Switching-Converter Power Stages,” in *Power Electronics Specialists Conference, 1976 IEEE*, June 1976, pp. 18–34. 15
- [77] F. Milano, “A Python-based Software Tool for Power System Analysis,” in *Procs. of the IEEE PES General Meeting*, Vancouver, BC, Jul. 2013. 40
- [78] F. Milano, *Power System Modelling and Scripting*. London: Springer, 2010. 35, 37, 45, 52, 120
- [79] F. Milano, “Semi-Implicit Formulation of Differential-Algebraic Equations for Transient Stability Analysis,” *IEEE Transactions on Power Systems*, vol. PP, no. 99, pp. 1–10, 2016. 56

- [80] F. Milano and Á. Ortega, “Frequency Divider,” *IEEE Transactions on Power Systems*, 2016, (in press). 30, 31
- [81] F. Milano and R. Zárate-Miñano, “Study of the Interaction between Wind Power Plants and SMES Systems,” in *12th Wind Integration Workshop*, London, UK, Oct. 2013. 12, 25
- [82] F. Milano and R. Zárate-Miñano, “A Systematic Method to Model Power Systems as Stochastic Differential Algebraic Equations,” *IEEE Transactions on Power Systems*, vol. 28, no. 4, pp. 4537–4544, Nov. 2013. 74, 119
- [83] Minyuan Guan, Wulue Pan, Jing Zhang, Quanrui Hao, Jingzhou Cheng, and Xiang Zheng, “Synchronous Generator Emulation Control Strategy for Voltage Source Converter (VSC) Stations,” *IEEE Transactions on Power Systems*, vol. 30, no. 6, pp. 3093–3101, Nov 2015. 26
- [84] M. G. Molina, P. E. Mercado, and E. H. Watanabe, “Improved Superconducting Magnetic Energy Storage (SMES) Controller for High-Power Utility Applications,” *IEEE Transactions on Energy Conversion*, vol. 26, no. 2, pp. 444 – 456, Jun. 2011. 73
- [85] P. Moutis, A. Vassilakis, A. Sampani, and N. Hatzargyriou, “DC Switch Driven Active Power Output Control of Photovoltaic Inverters for the Provision of Frequency Regulation,” *IEEE Transactions on Sustainable Energy*, vol. 6, no. 4, pp. 1485–1493, Oct 2015. 26
- [86] New York Power Authority, “Energy Storage Activities at New York Power Authority .” [Online]. Available: <http://www.publicpower.org/files/NationalConference/Kou.pdf> 19, 68
- [87] T. D. Nguyen, K. J. Tseng, S. Zhang, S. Zhang, and H. T. Nguyen, “Model predictive control of a novel axial flux permanent magnet machine for flywheel energy storage system,” in *IPEC, 2010 Conference Proceedings*, Oct 2010, pp. 519–524. 73
- [88] J. Nutaro and V. Protopopescu, “Calculating Frequency at Loads in Simulations of Electro-Mechanical Transients,” *IEEE Transactions on Smart Grid*, vol. 3, no. 1, pp. 233–240, March 2012. 27, 28, 36
- [89] Á. Ortega and F. Milano, “Generalized Model of VSC-Based Energy Storage Systems for Transient Stability Analysis,” *IEEE Transactions on Power Systems*, vol. 31, no. 5, pp. 3369–3380, Sept 2016. 55
- [90] Á. Ortega and F. Milano, “Comparison of Bus Frequency Estimators for Power System Transient Stability Analysis,” in *International Conference on Power System Technology (POWERCON)*, Wollongong, Australia, Sep. 2016. 28
- [91] Á. Ortega and F. Milano, “Design of a Control Limiter to Improve the Dynamic Response of Energy Storage Systems,” in *Power Engineering Society General Meeting, IEEE*, Denver, Colorado, USA, July 2015. 13, 55, 114
- [92] Á. Ortega and F. Milano, “Modeling, Simulation and Comparison of Control Techniques for Energy Storage Systems,” *IEEE Transactions on Power Systems*, 2016, (in press). 73

- [93] B. C. Pal, A. H. Coonick, I. M. Jaimoukha, and H. El-Zobaidi, “A Linear Matrix Inequality Approach to Robust Damping Control Design in Power Systems with Superconducting Magnetic Energy Storage Device,” *IEEE Transactions on Power Systems*, vol. 15, no. 1, pp. 356–362, Feb. 2000. 54
- [94] O. Palizban and K. Kauhaniemi, “Energy Storage Systems in Modern Grids - Matrix of Technologies and Applications,” *ELSEVIER Journal of Energy Storage*, vol. 6, pp. 248–259, 2016. 2, 3, 5, 17
- [95] C. Patsios, B. Wu, E. Chatzinikolaou, D. J. Rogers, N. Wade, N. P. Brandon, and P. Taylor, “An Integrated Approach for the Analysis and Control of Grid Connected Energy Storage Systems,” *ELSEVIER Journal of Energy Storage*, vol. 5, pp. 48–61, 2016. 5
- [96] M. Pavella, D. Ernst, and D. Ruiz-Vega, *Transient Stability of Power Systems – A Unified approach to Assessment and Control*. Boston: Kluwer Academic Publishers, 2000. 27
- [97] M. Perninge, V. Knazkins, M. Amelin, and L. Söder, “Risk Estimation of Critical Time to Voltage Instability Induced by Saddle-Node Bifurcation,” *IEEE Transactions on Power Systems*, vol. 25, no. 3, pp. 1600–1610, Aug. 2010. 119
- [98] PowerSouth Energy Cooperative, “Compressed Air Energy Storage: McIntosh Power Plant (Alabama).” [Online]. Available: http://www.powersouth.com/teenpower/mcintosh_power_plant/compressed_air_energy 2
- [99] G. Ramtharan, J. Ekanayake, and N. Jenkins, “Frequency Support from Doubly Fed Induction Generator Wind Turbines,” *IET Renewable Power Generation*, vol. 1, no. 1, pp. 3–9, March 2007. 26
- [100] P. F. Ribeiro, B. K. Johnson, M. L. Crow, A. Arsoy, and Y. Liu, “Energy Storage Systems for Advanced Power Applications,” *Proceedings of the IEEE*, vol. 89, no. 12, pp. 1774–1756, Dec. 2001. 1, 2, 17
- [101] K. Samarakoon, J. Ekanayake, and N. Jenkins, “Investigation of Domestic Load Control to Provide Primary Frequency Response Using Smart Meters,” *IEEE Transactions on Smart Grid*, vol. 3, no. 1, pp. 282–292, March 2012. 26
- [102] S. Samineni, B. K. Johnson, H. L. Hess, and J. D. Law, “Modeling and Analysis of a Flywheel Energy Storage System for Voltage Sag Correction,” *IEEE Transactions on Industry Applications*, vol. 42, no. 1, pp. 42–52, Jan. 2006. 22
- [103] Schwungrad Energie Limited, “First Hybrid-Flywheel Energy Storage Plant in Europe Announced in Ireland.” [Online]. Available: <http://schwungrad-energie.com/hybrid-flywheel-energy-storage-plant-europe-announced-ireland/> 87
- [104] Schwungrad Energie Limited, “Rhode Hybrid Energy Storage Test Facility.” [Online]. Available: <http://schwungrad-energie.com/projects/rhode-hybrid-test-facility/> 87

- [105] C. M. Shepherd, “Design of Primary and Secondary Cells II. An Equation Describing Battery Discharge,” *Journal of the Electrochemical Society*, vol. 112, no. 7, pp. 657–664, 1965. 18, 70
- [106] J. Shi and Y.-S. Lu, “Chatter Free Variable Structure Perturbation Estimator on the Torque Control of Flexible Robot Joints with Disturbance and Parametric Uncertainties,” in *Industrial Electronics, Control, and Instrumentation, 1996., Proceedings of the 1996 IEEE IECON 22nd International Conference on*, vol. 1, Aug 1996, pp. 238–243 vol.1. 78
- [107] V. P. Singh, S. R. Mohanty, N. Kishor, and P. K. Ray, “Robust H-infinity load frequency control in hybrid distributed generation system,” *Electrical Power & Energy Systems*, vol. 46, pp. 294–305, 2013. 54, 73, 76
- [108] H. Sira-Ramírez and R. Silva-Ortigoza, *Control Design Techniques in Power Electronics Devices*. London: Springer, 2006. 15
- [109] S. E. Z. Soudjani and A. Abate, “Aggregation of Thermostatically Controlled Loads by Formal Abstractions,” in *Control Conference (ECC), 2013 European*, 2013, pp. 4232–4237. 39
- [110] X. Sui, Y. Tang, H. He, and J. Wen, “Energy-Storage-Based Low-Frequency Oscillation Damping Control Using Particle Swarm Optimization and Heuristic Dynamic Programming,” *IEEE Transactions on Power Systems*, Mar. 2014. 54
- [111] M. Swierczynski, D. Stroe, A.-I. Stan, R. Teodorescu, and D. Sauer, “Selection and Performance-Degradation Modeling of $\text{LiMO}_2/\text{Li}_4\text{Ti}_5\text{O}_{12}$ and LiFePO_4/C Battery Cells as Suitable Energy Storage Systems for Grid Integration With Wind Power Plants: An Example for the Primary Frequency Regulation Service,” *IEEE Transactions on Sustainable Energy*, vol. 5, no. 1, pp. 90–101, Jan 2014. 5, 26
- [112] C. Taylor and S. Lefebvre, “HVDC Controls for System Dynamic Performance,” *IEEE Transactions on Power Systems*, vol. 6, no. 2, pp. 743–752, May 1991. 26
- [113] M. M. Tiller, *Introduction to Physical Modeling with Modelica*. Boston: Kluwer Academic Publishers, 2001. 33
- [114] C. Trabert, A. Ulbig, and G. Andersson, “Model predictive frequency control employing stability constraints,” in *American Control Conference (ACC), 2015*, July 2015, pp. 5678–5685. 73
- [115] O. Tremblay, L.-A. Dessaint, and A.-I. Dekkiche, “A Generic Battery Model for the Dynamic Simulation of Hybrid Electric Vehicles,” in *Vehicle Power and Propulsion Conference*. Arlington, TX: IEEE, Sep. 2007, pp. 284–289. 18, 70
- [116] UK Department of Trade and Industry, “Meeting the Energy Challenge,” White Paper, 2007. [Online]. Available: https://www.gov.uk/government/uploads/system/uploads/attachment_data/file/243268/7124.pdf 1
- [117] U.S. Department of Energy, “2014 Wind Technologies,” Market Report, 2015. [Online]. Available: <http://energy.gov/sites/prod/files/2015/08/f25/2014-Wind-Technologies-Market-Report-8.7.pdf> 1

- [118] V. I. Utkin, "Sliding Mode Control Design Principles and Applications to Electric Drives," *IEEE Transactions on Industrial Electronics*, vol. 40, no. 1, pp. 23–36, Feb 1993. 78
- [119] V. Utkin, J. Guldner, and J. Shi, *Sliding Mode Control in Electro-Mechanical Systems*, 2nd ed. CRC Press, 2009. 78
- [120] V. Vongmanee, "The Renewable Energy Applications for Uninterruptible Power Supply Based on Compressed Air Energy Storage System," in *IEEE Symposium on Industrial Electronics and Applications (ISIEA 2009)*, Kuala Lumpur, Malaysia, Oct. 2009, pp. 827–830. 19, 20
- [121] J. Winkelman, J. Chow, B. Bowler, B. Avramovic, and P. Kokotovic, "An Analysis of Interarea Dynamics of Multi-Machine Systems," *IEEE Transactions on Power Apparatus and Systems*, vol. PAS-100, no. 2, pp. 754–763, Feb 1981. 27
- [122] J. Wu, J. Wen, H. Sun, and S. Cheng, "Feasibility Study of Segmenting Large Power System Interconnections With AC Link Using Energy Storage Technology," *IEEE Transactions on Power Systems*, vol. 27, no. 3, pp. 1245–1252, Aug. 2012. 54
- [123] H. Xin, L. Huang, L. Zhang, Z. Wang, and J. Hu, "Synchronous Instability Mechanism of P-f Droop-Controlled Voltage Source Converter Caused by Current Saturation," *IEEE Transactions on Power Systems*, vol. 31, no. 6, pp. 5206–5207, Nov 2016. 108
- [124] K. Yang and A. Walid, "Outage-Storage Tradeoff in Frequency Regulation for Smart Grid With Renewables," *IEEE Transactions on Smart Grid*, vol. 4, no. 1, pp. 245–252, March 2013. 26
- [125] A. Yazdani and R. Iravani, *Voltage-Sourced Converters in Power Systems. Modeling, Control and Applications*, 1st ed. Wiley-IEEE Press, 2010. 14, 100, 104
- [126] H. Yuan-Yih and C. Chung-Liang, "Probabilistic Transient Stability Studies Using the Conditional Probability Approach," *IEEE Transactions on Power Systems*, vol. 3, no. 4, pp. 1565–1572, Nov 1988. 102
- [127] R. Zárate-Miñano and F. Milano, "Construction of SDE-based Wind Speed Models with Exponentially Decaying Autocorrelation," *Renewable Energy*, vol. 94, pp. 186 – 196, 2016. 120
- [128] K. Zhang, C. Mao, J. Lu, D. Wang, X. Chen, and J. Zhang, "Optimal control of state-of-charge of superconducting magnetic energy storage for wind power system," vol. 8, no. 1, pp. 58–66, Jan. 2014. 73
- [129] Z. Zhong, C. Xu, B. J. Billian, L. Zhang, S. J. S. Tsai, R. W. Conners, V. A. Centeno, A. G. Phadke, and Y. Liu, "Power System Frequency Monitoring Network (FNET) Implementation," *IEEE Transactions on Power Systems*, vol. 20, no. 4, pp. 1914–1921, Nov 2005. 28
- [130] D. Zhu and G. Hug-Glanzmann, "Robust Control Design for Integration of Energy Storage into Frequency Regulation," in *Innovative Smart Grid Technologies (ISGT Europe), 3rd IEEE PES International Conference and Exhibition*, Berlin, Oct. 2012, pp. 1–8. 73, 76

Index

- A**
Asynchronous Motor, 14, 19, 37
- D**
DOME, 40
dq-frame Representation, 14, 15, 20, 22, 29, 36
- E**
ESS Control, 12–13, 26, 57, 73–95
 H-infinity Control, 73, 75–77
 PI Control, 12, 73, 75
 Sliding Mode Control, 73, 78–80
 Storage Input Limiter, 13, 114–118
ESS Modeling
 Generalized Model, 7, 54–72, 76, 78
 Simplified Model, 54, 61–70
 Transient Stability Model, 17–25, 61–70
ESS Technologies, 1, 2, 17–57
 BES, 1, 17–18, 59, 70, 87, 104, 114
 CAES, 1, 19–21, 60, 68–70
 FES, 1, 22–23, 60, 87, 104
 SCES, 1, 23–24, 59
 SMES, 1, 24–25, 60, 62–66
ESS Transient Stability, 96–108
 Probabilistic Stochastic Analysis, 102
- F**
Frequency Estimation, 26–53
 Center of Inertia, 7, 27, 28, 35–53, 62, 70, 81, 84, 104, 115
 Frequency Divider, 30–53, 93, 104
 Washout Filter, 28, 35–53
- I**
Inertia, 1, 7, 27, 28
- M**
Monte Carlo Method, 74, 88
- P**
Phase-Locked Loop, 15
- R**
Renewable Energy Source, 1, 26, 102
 Solar, 1, 26
 Wind, 1, 26, 47, 50, 80, 87, 104
- S**
Simulation Test System
 All-Island, 1,479-Bus Irish System, 47–50, 87–94, 104–108
 ENTSO-E, 21,177-Bus System, 47, 51–52
 IEEE 14-Bus System, 38, 40–43, 80–84
 New England, 39-Bus, 10-Machine System, 38, 44–46
 WSCC 9-Bus System, 61–70, 114–116
STATCOM, 100, 104
Stochastic Process, 119–120
 Ornstein-Uhlenbeck’s Process, 66, 69, 87, 116, 119
 Weibull Distribution, 48, 81, 87, 104, 120

Synchronous Machine, 7, 26–28, 30, 33, 35,
45, 47, 48, 61, 80, 98, 104

System Regulation

Frequency, 1, 11, 26, 62, 70, 81–84, 93–
94, 104, 115

Line Active Power Flow, 1, 11, 68, 88–
93

RoCoF, 1

Voltage, 1, 16, 105

T

Thermostatically Controlled Load, 39

Transient Stability, 97, 102

Critical Clearing Time, 97, 99

Equal Area Criterion, 98

V

Voltage Sourced Converter, 2, 14–16, 55,
57, 100, 104

W

Washout Filter, 27